Charles University in Prague
Faculty of Mathematics and Physics
Department of Electronic Structures

Investigation of Magnetic Processes of Structure-Degraded Ferromagnetic Materials

Oleksandr Stupakov

Doctoral Thesis

Supervisors:
RNDr. Ivan Tomáš, CSc. (10.2001-6.2004)
Prof. RNDr. Vladimír Sechovský, DrSc. (7.2004-6.2006)

Prague 2006

Preface

During my post-graduate study at the Department of Condensed Matter Physics and Material Research of Charles University in Prague and collaboration with the Department of Magnetism at the Institute of Physics AS CR in Prague my research topic was investigation of magnetization processes of structurally modified ferromagnetic materials under supervision by Dr. I. Tomáš. The main task of the study was analysis of applicability of magnetic non-destructive testing methods for evaluation of structure degradations of construction ferromagnetic steels.

Magnetic investigation was carried out on similarly degraded series of magnetically *closed* and *open* samples. The *closed* samples are composed of a magnetically homogeneous circuit of the tested material and usually realized in the form of a ring. These specimens with a driving coil for the sample magnetization and an induction coil for the flux measurement, wound along the ring perimeter, are the most preferable for precise and repeatable magnetic measurements. But this method demands large labor and time expenses, which substantially limits its attraction as a commercial technique.

Industry needs a simple, fast and stable measuring technique for characterization of the magnetically *open* samples (e.g. rolled steel sheets). However, this problem has not been solved to the full extent yet. All developed devices are either too robust or unstable to small deviations of the measurement conditions. In this work the inductive measurements of the open samples were done with an attached U-shaped yoke carrying the magnetizing and the induction coils. In that way the magnetically *closed* circuit "yoke-sample" is formed for the measurements. Analysis

of the results of the parallel measurements on the *closed* and the *open* samples was supposed to determine conditions of applicability of the single-yoke technique.

The methods of magnetic testing of structure properties of materials have been investigated and utilized in practice for decades. In introductory Chapter 1 a short historical survey and state-of-art methods of the measurement and of the data evaluation, concerned with this work, are presented.

Chapter 2 of this thesis is devoted to detailed investigation of the magnetic response to a special case of structure degradation, namely to plastic uniaxial deformation of a low-carbon steel. Hysteresis magnetic measurements were performed in different experimental configurations: with different magnetization directions and with different series of the closed and the open samples. These results were supplemented and compared with Barkhausen noise measurements, carried out by Ing. J. Pal'a at the University of Technology in Bratislava on the same sample series. Besides the observed physical features of magnetic behavior, our main task was investigation of applicability of the magnetic testing methods for examination of the material deformation. Basic results of this research are the following:

- indication of the degradation level, caused by the plastic deformation, with the help of proposed alternative magnetic parameters.
- detection and explanation of magneto-structural anisotropy with respect to the direction of the applied uniaxial deformation.
- analysis of principal differences of the inductive measurements on the magnetically closed and open samples.

The results of the single yoke measurements, presented in Chapter 2, have shown remarkable *instability* of the technique with regard to the *yoke-sample contact* quality. This stimulated us to investigate technical part of the problem, namely, the question of single-yoke measurement optimization in order to increase accuracy of this attractive and simple

technique. The results of this work are presented in Chapter 3 of the thesis. It was suggested that the yoke measurements have to be stabilized by precise determination of *inside-sample field*. However, because of significant field gradients at the samples' surface it is a non-trivial task. It was proposed to utilize *multi-point surface field* measurements with *extrapolation* of the field profile to the sample surface. Simultaneous measurements of the magnetic material properties and of the surface sample fields have confirmed our suggestion about substantially improved stability of the field extrapolation method to the yoke-sample contact imperfections compared with the widely used methods of the sample field determination from the magnetizing current or the one-point surface field measurements. The method was proposed to be used in practice for local magnetic non-destructive control. The advantages as well as important drawbacks of the measurement procedure and of the extrapolation method were discussed in detail.

Accomplishment of the present work would have been impossible without valuable support by my supervisors Dr. I. Tomáš and Prof. V. Sechovský, as well as by my colleagues Dr. O. Perevertov, Ing. J. Pal'a, Dr. J. Kadlecová, Dr. G. Vértesy, Dr. J. Bydžovský, Dr. V. Novák, Prof. S. Takahashi, and by all my teachers, professors of Donetsk National University and of Charles University in Prague, to whom I owe my advances in the ways of science. The author is also very thankful to Dr. B. Skrbek for preparation of the measured samples and to M. Crhán for technical assistance. The financial support by the Grant Agency of the Czech Republic (projects No. 101/02/0236, No. 1QS100100508 and No. AVOZ10100520), by Charles University in Prague, by Iwate University in Morioka and last but definitely not least by Institute of Physics AS CR in Prague are greatly acknowledged.

Contents

Glossary of symbols

Symbol	SI Units	Meaning
$\mathbf{A}$	Vs/m	Magnetic vector potential
$\mathbf{B}$	T	Magnetic induction (flux density)
B_h	T	Head magnetic induction
B_m	T	Maximum magnetic induction (amplitude)
B_R	T	Remanent induction
B_R^*	T	Effective remanent induction
B_s	T	Sample magnetic induction
D_h	mm	Head height
d	mm	Sample thickness
g	mm	Driving Coil gap (DCL configuration)
$\mathbf{H}$	A/m	Magnetic field strength
H_c	A/m	Coercive field
H_c^*	A/m	Effective coercive field
H_{ext}	A/m	Extrapolated field
H_{hall}	A/m	Measured surface sample field
H_m	A/m	Maximum magnetic field (field amplitude)
H_m^*	A/m	Effective field amplitude
H_{on}	A/m	On-/above-sample magnetic field
H_s	A/m	Sample magnetic field
H_s^*	A/m	Effective sample magnetic field
H_{sat}	A/m	Saturation magnetic field
H_{un}	A/m	Under-sample magnetic field
H_x	A/m	Tangential x-component of magnetic field

$\mathbf{I}$	A	Current
L_{DC}	mm	Driving Coil width (DCL configuration)
L_h	mm	Head width
L_l	mm	Head legs width
l	mm	Magnetic path
l_a	mm	Air-gap magnetic path
l_h	mm	Head magnetic path
l_s	mm	Sample magnetic path
N	–	Turn number of magnetizing winding
n	–	Turn number of induction winding
r	mm	Radius
S	mm^2	Cross-section
S_a	mm^2	Air-gap cross-section
S_h	mm^2	Head leg cross-section
S_s	mm^2	Sample cross-section
T	^oC	Tempering temperature
t	s	Time
U_{ind}	V	Induced voltage
U_{env}	V	Barkhausen noise envelope
U_{env}^{max}	V	Maximum of Barkhausen noise envelope
U_{RMS}	V	Barkhausen noise RMS
W_h	$\mathrm{J/m}^3$	Hysteresis losses
x, y, z	mm	Space axes
ΔH	A/m	Magnetic field step
Δ_h	mm	Head depth
ε	–	Mechanical strain
μ_0	$4\pi 10^{-7}\mathrm{H/m}$	Permeability of vacuum
μ_a	1	Permeability of air
μ_h	–	Permeability of head
μ_R	–	Remanent differential permeability
μ_s	–	Permeability of sample
μ_{dif}	–	Differential magnetic permeability

μ_{max}	–	Maximum differential permeability
μ^*_{max}	–	Effective maximum differential permeability
Φ	Wb	Magnetic flux
Φ_h	Wb	Head magnetic flux
Φ_s	Wb	Sample magnetic flux

List of abbreviation

Abbreviation	Meaning
2-D	2 Dimensional
3-D	3 Dimensional
AC	Alternating Current
BN	Barkhausen Noise
DC	Direct Current
DCB	Driving Coil on the head Bow
DCL	Driving Coils on the head Legs
FEM	Finite Element Method
MAT	Magnetic Adaptive Testing
NDT	Non-Destructive Testing
RMS	Root Mean Square
SST	Single Sheet Tester
TEM	Transmission Electron Microscopy

Chapter 1

Introduction

The issue of Non-Destructive Testing (NDT) of compositional and structural variation or degradation of construction ferromagnetic steels is still one of very topical problems in metal industry. There is strong need of NDT evaluation of structural changes of steels during production processes: rolling, extrusion, cutting or punching. Gas pipeline industry and other steel producers are also interested in reliable estimation of the remaining life of steel constructions and industrial plants. General simplicity and economical feasibility of magnetic testing techniques attract broad attention to the inspection methods, based on coupling of magnetization processes of such materials to details of their structural changes (see reviews [1, 2]). The spectrum of investigated structural modifications of ferromagnetic construction materials belonging to the field of the classical industrial interests includes consequences of quenching and tempering [3, 4, 5], mechanical tension and compression [6, 7, 8], fatigue [9, 10], irradiation [11], etc. This introductory chapter presents a short survey, needed for understanding of motivations of this work. Section 1.1 contains review of the techniques, used for inductive magnetic measurements in industry and in laboratory conditions. Section 1.2 is devoted to the problem of the best choice of magnetic descriptors for indication of material structure changes of interest.

1.1 Measurement techniques

The most precise method of inductive magnetic measurement of *homogenous* materials is the use of magnetically *closed* rings with the magnetizing (driving) and the measuring (induction) coils, directly wound on their bodies. The rings should be thin in comparison with their mean radius r with homogenously distributed driving coil around their perimeter [12, 13]. The principle of the measurement is very simple: Alternating Current (AC) $I(t)$ in the driving coil generates homogenous magnetic field $H_s(t)$ along the ring perimeter; the measuring coil voltage U_{ind} is proportional to the derivative of the sample magnetic flux Φ_s according to the induction law [14].

$$H_s(t) = \frac{N}{l_s} I(t) = \frac{N}{2\pi r} I(t) \tag{1.1}$$

$$U_{ind} = -n \frac{\mathrm{d}\Phi_s}{\mathrm{d}t} = -n S_s \frac{\mathrm{d}B_s}{\mathrm{d}t} \tag{1.2}$$

where l_s is the sample magnetic path (mean ring perimeter); S_s is the sample cross-section; B_s is the sample magnetic induction (subscript s means sample); N and n are turn numbers of the driving and of the induction coils, respectively. Obviously, this method is not suitable for any serious industrial application due to its complexity (sample cutting and coils winding) and limitation to homogenous material testing. In the thesis this classical method is utilized for laboratory measurement to obtain precise magnetic characteristics of investigated materials for comparison with parallel measurement on magnetically *open* samples.

Industrial NDT evaluation needs a simple and fast measuring technique for material characterization of magnetically *open* samples (sheets or strips of different shapes). Inductive magnetic measurements have been used for this task for decades. Because of its high accuracy and reproducibility, the classical Epstein's apparatus [15] remains for more than a century to be one of the major instruments for evaluation of electrical steel quality in industry. The samples for the Epstein testing are arranged from steel strips of 30 × 500 mm size, collected in four piles

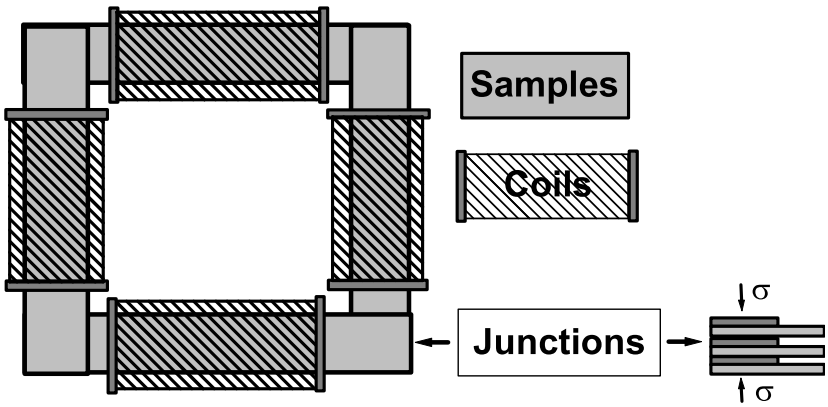

Figure 1.1: Principal scheme of the Epstein apparatus.

of 2.5 kg each. Total weight of the sample is 10 kg, and total length is 2 m. There is also smaller variant of the device with 30 × 250 mm size samples of the weight of 0.5-1.5 kg each. The procedure of the sample fabrication includes accurate cutting of the strips and their additional annealing for residual stress relief. Then the piles are composed together to *closed* square frame with four double driving-induction windings in solenoid-like surrounding as is shown in Fig. 1.1. At junctions the piles are pressed by a special fix equipment. The device is usually used for hysteresis loss W_h measurement at constant maximal induction B_m and at 50 Hz sinusoidal excitation current (conditions of transformer sheet application). Magnetic parameters are calculated similar to the case of the ring measurements (see Eqs. 1.1-1.2). Declared precision of the measurement method according to the standard is 3%, but in reality it can be 5-10%. The main reason is bad contact condition and field distribution inhomogeneity on the pile junctions [12]. Obviously, use of the Epstein apparatus has another certain detractions, notably in being expensive and time consuming. These facts stimulated development of a whole series of other devices for measurements of magnetic characteristics of steel sheets, mostly of their magnetic losses W_h and coercive fields H_c (see reviews [16, 17]).

Another standard method for measuring of open magnetic sheets is the Single Sheet Tester (SST) [18]. Closed magnetic circuits are formed

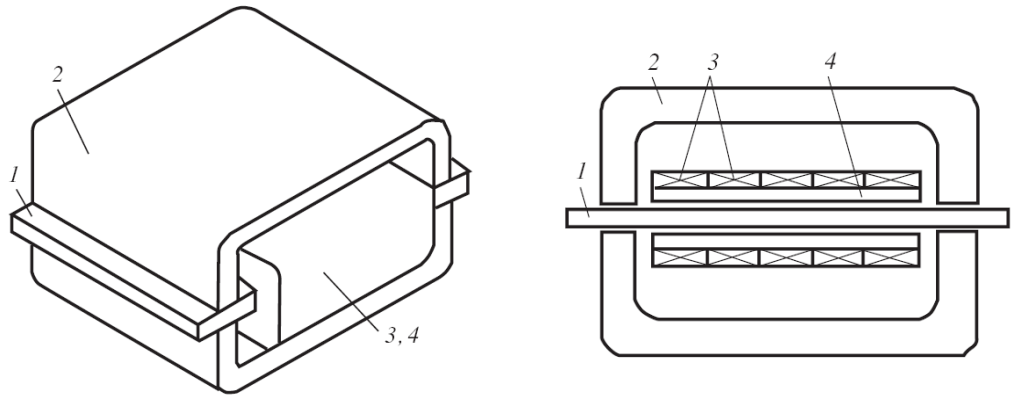

Figure 1.2: Scheme of the SST device: (1) tested sheet sample, (2) magnetic yokes, (3) magnetizing winding, (4) measuring winding.

by magnetically soft conductors (two U-shaped yokes) with large cross-section of the legs, pressed to plane edges of the sheet. The magnetizing and the measuring windings are incorporated in the solenoid surrounding the tested sample. In Fig. 1.2 the scheme of this simplest variant of the SST device is presented. Magnetic field of the tested sheet is calculated again according Eq. 1.1 with the magnetic sample path equal to the inner distance between the yoke legs. However, this approach leads to mistakes due to non-homogenous field distribution through the sample-yokes system in contrast to the ideal ring case.

Another standard variation of the SST device, which is more physically accurate, is based on the surface sample field determination by an H-coil. The H-coil is an additional induction air-coil, positioned between the sample and the solenoid-like surrounding. It measures the signal $U_{ind} \sim \mathrm{d}B/\mathrm{d}t$, which is proportional to $\mathrm{d}H/\mathrm{d}t$ in vacuum. However, the standard prefers the first method of the field determination (the current method) because of instabilities and small signal amplitudes of the H-coil [19]. The SST has very similar disadvantages to the Epstein: firstly, extreme attention must be paid to good contact quality between the constituents of the composed magnetic circuit, and, secondly, the driving and the induction coils are required to be positioned directly on the investigated specimen in order to increase the device precision. Un-

certainty of the W_h measurement can also reach $\pm 10\%$ [19]. The main problem on the way of complete substitution of the cumbrous Epstein apparatus by the easier SST device in practice is the lack of coincidence between the measurement results, obtained by these two different techniques [20, 21, 22]. Therefore, there were and still are a lot of attempts to improve the SST device [16, 23, 24, 25]. However, there is no general understanding how it should be done, and work in different research groups goes in relatively different ways. Attempts of the measurements of the same sample series on these different laboratory equipments have shown substantial scatter of the results [26, 27].

At the end of 1930s in former USSR a coercimeter with a single inspection U-yoke was developed and introduced for local magnetic control of ferromagnetic steel sheets (see reviews [28, 29]). It had considerable design differences from the SST device: firstly, the coercimeter dimensions are by an order of magnitude smaller than those of the SST, and, secondly, the magnetizing coils are wound on the yoke legs. Additionally, a moving current loop, positioned into the yoke bow, was applied for determination of the magnetic flux through the yoke-sample circuit. In 1950s replacement of the current loop by a flux-gate meter led to a considerable increase of operational speed and measurement precision (see Fig. 1.3). Positioning of the magnetizing coil and of the flux meter on the yoke body changes the measurement conditions significantly. In the SST design the yokes are used only for closing the sample magnetic flux, whereas in the coercimeter case the samples are magnetized by the yoke-generated flux, what complicates the system a lot. Moreover, the measured yoke flux by the flux-gate is not equal to the sample flux due to the non-zero flux leakage through the yoke legs. However, this mobile coercimeter, simple and fast in use, with a set of different *inspection heads* has found wide application in industry. The investigated single yokes with the coils and other magnetic sensors, placed on the yoke bodies, will be referred to hereafter in this work as *inspection heads*.

The principle of coercimeter work is very simple: the sample is magnetized to saturation first, and then, with the magnetizing current decrease,

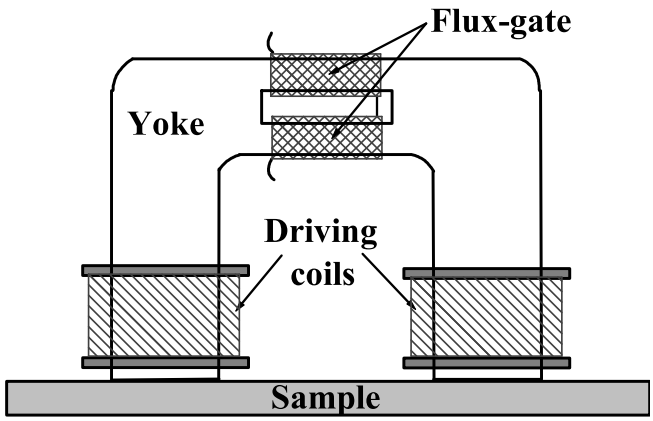

Figure 1.3: Principal scheme of the coercimeter device.

the current value, when the yoke flux equals zero, is fixed and referred to the coercive field H_c. Series of papers were devoted to investigations of the result stability and of the error sources of the measurement technique as well as the methods of its optimization [30, 31]. In 1970-80s after minimal changes in the measurement technique, the coercimeter started to be used for measurement of a whole set of other magnetic parameters: remanent induction B_R, relaxation coercive force, maximum permeability μ_{max}, etc [28, 29]. Magnetic characteristics are evaluated similarly to Eq. 1.1-1.2 assuming that $H_s(t) \sim I(t)$ and that the measured $\Phi_h \simeq \Phi_s$ (subscript h means head/yoke).

In the last decades a similar single-yoke setup, also considered by author in this work, is frequently used for laboratory investigation because of its simplicity. An induction winding, wound directly on the yoke body for determination of the system flux, has replaced the flux-gate meter [32, 33]. The induction signal U_{ind} in the simplest and the roughest case is classically referred to the *magnetizing current* $I(t)$, as for the coercimeter method [34, 35], or to the *magnetic field*, measured by a magnetic sensor on the *sample surface*. The first attempts of the surface field measurements were done with the H-coil in analogy with the SST [36]; nowadays mainly a Hall sensor is used [32, 33, 37]. The main drawback of such a technique is the well-known problem of substantial

dependence of the measurement results on the contact quality between the sample and the attached yoke [28, 31, 37, 38]. In order to extend applicability of this technique to standardized industrially used method, this problem must be fixed to an acceptable level of the parameters determination error. The results of the single-yoke measurements with the simple reference to the *magnetizing current* is presented in Chapter 2 of this thesis. Detailed analysis of applicability of the single-yoke setup with the *surface field* measurements and propositions about the device optimization are given in Chapter 3.

1.2 Magnetic parameters

Traditional magnetic parameters, historically used for ferromagnetic material evaluation, are several characteristics, derived from the saturation hysteresis loop: remanent magnetic induction B_R, coercive force H_c, maximum permeability μ_{max}, maximum induction B_m, magnetic losses W_h (see Fig. 1.4) [7, 39]. Saturation is theoretically determined at maximum applied field $H_{sat} = H_m \simeq 10 - 20H_c$ [12], usually it is defined by fixing of the field amplitude H_m or of the magnetic induction B_m. B_R and H_c are intersection points of the hysteresis loop with the induction and the field axes, respectively. Physical meaning of the remanence B_R is the value of the magnetic induction of the ferromagnetic material in absence of the external magnetic field, left after previous magnetization to the saturation. The coercive field H_c is the field, needed to suppress this remanent magnetic induction. Magnetic parameter, mostly used in practice, is probably the magnetic hysteresis losses W_h (the Epstein and the SST devices – see previous Section 1.1). W_h is the work, required for remagnetization along the closed hysteresis loop, or simply the hysteresis area $W_h = \oint_{hyst} HdB$. Such a popularity of W_h is because of the practical necessity of testing this magnetic property of transformer sheets and electrical machines. The next frequently used parameter for magnetic NDT is the coercive field H_c (e.g. wide industrial application of coercimeters). The behavior of these two descriptors W_h and H_c is

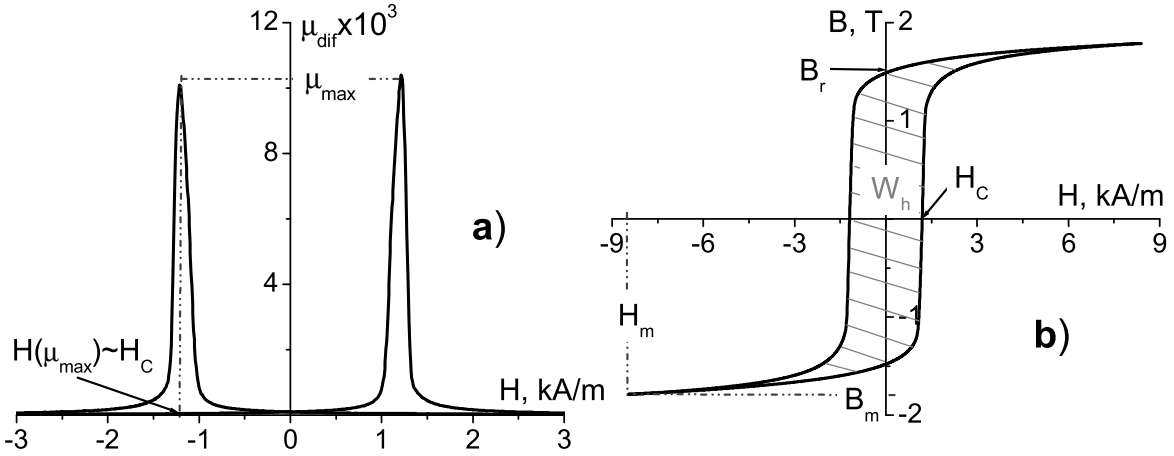

Figure 1.4: Traditional magnetic parameters of: (a) the differential permeability curve $\mu_{dif}(H) \sim \mathrm{d}B/\mathrm{d}H$; (b) the magnetic hysteresis loop $B(H)$.

usually very similar to each other in different cases of structure changes. Advantages of H_c over W_h is that, firstly, it is easier to be measured, and, secondly, it seems to be the most stable parameter for the measurement of magnetically open samples [28, 37]. In recent years with improvement of measurement techniques the attempts of utilization of other magnetic parameters, as B_R, B_m or less stable differential characteristic as μ_{max} ($\mu_0\mu_{dif} = \mathrm{d}B/\mathrm{d}H$), have been also done but with rather moderate success [28, 32, 37].

The traditional magnetic parameters are often not optimal indicators of structural alterations of ferromagnetic materials, which are industrially highly interesting. Nowadays the line of development of the topic is mostly shifted to a search for alternative magnetic parameters, which could be used more efficiently than their so far applied analogues, either by itself or together with the traditional descriptors. The research is carried out in all range of the applied field amplitudes H_m from low magnetization values up to saturation of the material [28, 35, 40]. It was shown [35, 40, 41] that magnetic descriptors, obtained at small applied magnetic fields H_m, could be more sensitive to structural alterations of the materials than the parameters, derived from the saturation loop.

One of the active research directions is investigation of so-called re-

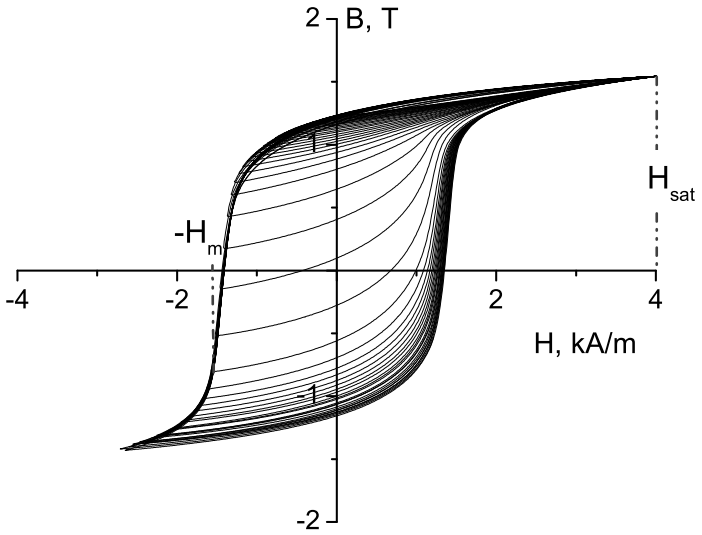

Figure 1.5: Example of the return branches measurement.

turn branches: the magnetization process is applied from saturation H_{sat} to current field amplitudes $H_m = H_{sat} - \Delta H; H_{sat} - 2\Delta H; \ldots; -H_{sat}$, where ΔH is some constant/floating step (see Fig. 1.5) [42]. In the coercimeter technique it is frequently used for measurement of new introduced parameters, like the relaxation coercive field (the return branch field $-H_m$, after which with further field increase the magnetic induction goes through zero) or the return branch remanence at the fixed $-H_m$ value (intersection of the return branches with the induction axis) [3]. This method of measurement is also utilized for Preisach modeling of the magnetic hysteresis [43].

Recently our group introduced a new algorithm of magnetic hysteresis data evaluation, referred to as the Magnetic Adaptive Testing (MAT) [41, 44]. It represents an attempt to generalize the search for the most sensitive and reliable magnetic parameters, connected with investigated structural variations of ferromagnetic materials. MAT works with symmetrical families of minor hysteresis loops $H_m = \pm\Delta H; \pm 2\Delta H; \ldots$ from a minimum possible amplitude ΔH up to the major, saturated one H_{sat}. The physical basis is that, according to the Preisach theory [42, 43], this minor loop data-set (as well as the return branch data-set) contains

all possible information about hysteresis magnetization process. MAT simply picks up that *minor loop* H_m from the whole family and those *descriptor/s* within the selected minor loop, which are the most sensitive and reliable for the used sample material and for the investigated structural change. An example of such a minor loop hysteresis measurement is shown in Fig. 1.6(a) and of a minor loop $B(H, H_m)$ plane – in Fig. 1.6(b). Such a Preisach-like plane is used for graphic data presentation [41]. The shown $B(H, H_m)$ plane in reality is a plot of a matrix of the magnetic induction values B as a two-parametric function of the applied magnetic field H (matrix columns) and of the minor loop field amplitudes H_m (matrix rows) with a chosen constant step $\Delta H = \Delta H_m$. The potential of the proposed MAT-method was already proven on several series of magnetically *closed* ferromagnetic samples with structures, gradually degraded by application of mechanical stress and of thermal processing [45, 46]. Our recent results of MAT application to two parallel series of magnetically *closed* and *open* samples are presented in Chapter 2.

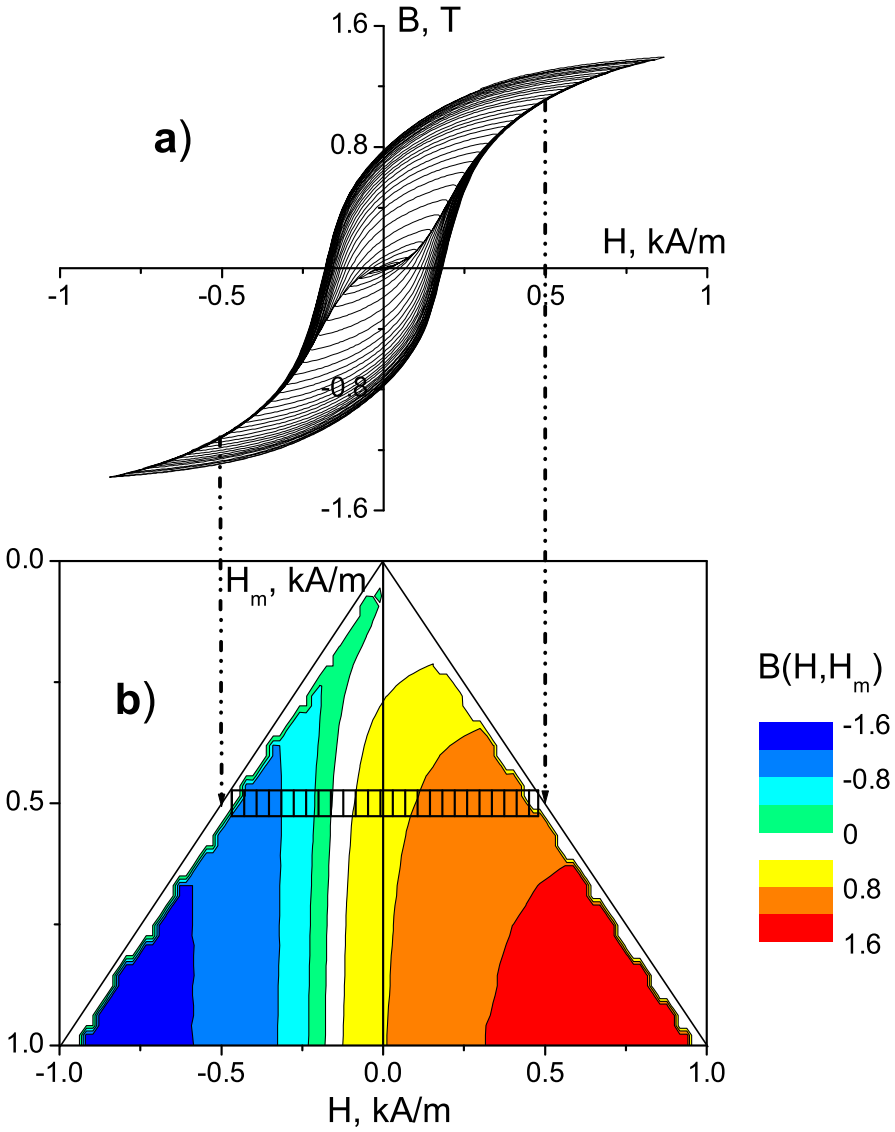

Figure 1.6: Example of the minor loop measurement (a) and of the data transformation of the upper hysteresis branches to the $B(H, H_m)$ plane (b). Correspondence of the chosen experimental minor loop $H_m = 0.5$ kA/m with the plane column $B(H, 0.5$ kA/m$)$ is shown for clarity.

Chapter 2

Investigation of plastic deformation

The issue of dependence of magnetic properties of ferromagnetic construction materials on applied mechanical stresses was one of the first phenomena attracting the scientists' attention with opening of the magnetic era 150 years ago [6, 7]. Despite of this, with recent improvement of measurement techniques the seemingly well-investigated topic stimulates lively debates about some interesting magnetic features of the stressed ferromagnetic materials: e.g. two-peak form of Barkhausen Noise (BN) envelopes [47, 48] and of differential permeability curves [8, 49] as well as the corresponding bulging of the hysteresis loops [8, 50, 51] with nearly fixed intersection points [7, 47, 51]. However, investigation of these problems is complicated by a wide variety of chemical and structural compositions of the investigated commercial steels. The magnetic response depends fundamentally on such structure details (e.g. presence of either two peaks of permeability curve [49] or initial increase of BN energy with strain [47, 52, 53]). This interesting magnetic behavior is usually explained by generation of a dislocation structure and by presence of internal stresses, which change the domain wall pinning and the magneto-elastic energy, respectively. The existence of inclusions or different structure phases (perlite, cementite, etc.) makes the situation even more confused [8, 47]. Aside from the physical interest, the problem is still very topical for industrial application [8, 37, 52]. Therefore, the main aim of our investigation was to reveal new magnetic parameters,

which can be utilized and compete with the classically used parameters in magnetic NDT.

In this chapter the results of complex investigation of mechanical degradation of low-carbon steel are presented. The magnetic tests (hysteresis and Barkhausen noise emission) were done on different sample series after unloading from plastic tensile deformation. The measurements were prepared with magnetization in the parallel as well as in the perpendicular directions to the previous elongation. The aim was to investigate the so far poorly known topic of magnetic anisotropy, caused by uniaxial deformation. The obtained characteristic features of the magnetic behavior (e.g. two-peaks profiles of the BN envelope and of the permeability leading to bulging of the hysteresis loops) were explained by the deformation-driven accumulation of residual intrinsic stresses and dislocation tangles. The dislocation structure formation was checked by Transmission Electron Microscopy (TEM). The observed interesting effect of the hysteresis "coincident" intersection points was also mentioned. Evolution of the magnetic parameters with the deformation was examined in detail and the most sensitive and stable magnetic parameters for the considered degradation were introduced and proposed for utilization. Applicability of the magnetic hysteresis method for NDT of previous plastic tension of steel components was discussed. Results of this work were published in a series of articles [45, 54, 55, 56]. Our next works, devoted to investigation of the magnetic response to other structure alterations of construction steel and cast iron, were presented in articles [46, 57].

2.1 Magnetic hysteresis measurements

2.1.1 Experiment

Low-carbon steel CSN 12013 (C = 0.03; Mn = 0.18; Si = 0.13; P = 0.027; S = 0.027; N = 0.007 $wt.\%$) was chosen for the investigation in order to consider the problem in a less complicated case of a ferritic steel with-

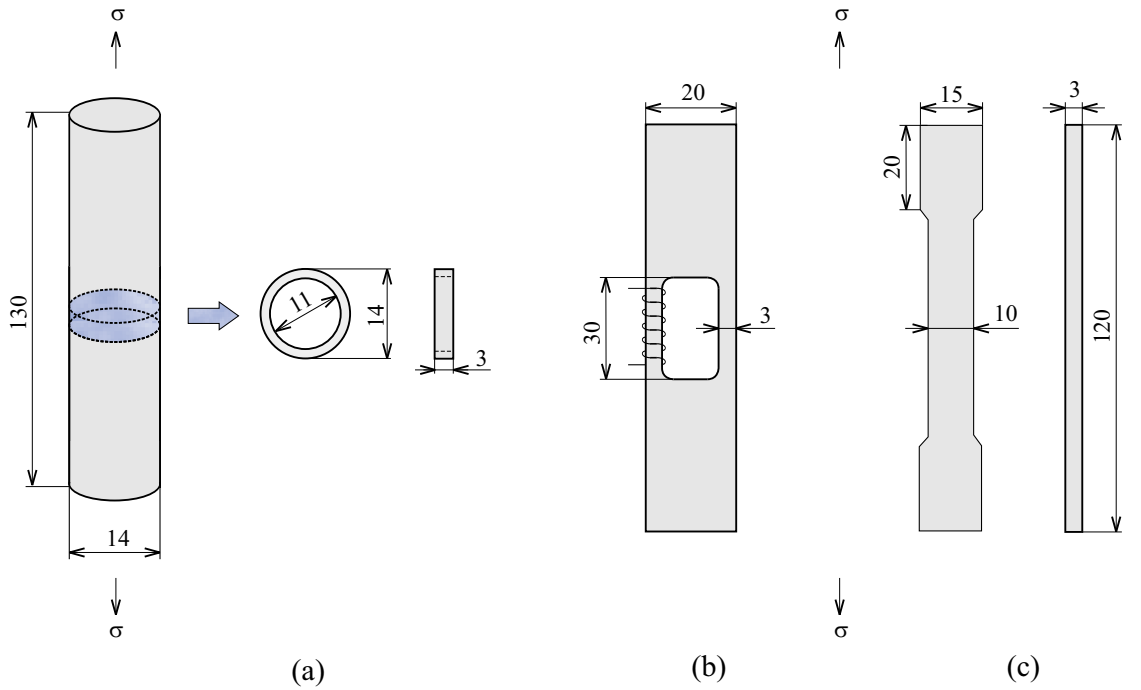

Figure 2.1: Used ring-shaped (a), window-shaped (b) and strip-shaped (c) samples (dimensions of the non-deformed specimens are pointed).

out any significant perlite or cementite inclusions. The samples were deformed to different strain values ε with the strain rate $\mathrm{d}\varepsilon/\mathrm{d}t = 3{\cdot}10^{-3}\,\mathrm{s}^{-1}$ in Instron 8872 machine and measured after unloading out of the Instron. The main ideas were, firstly, to investigate magneto-structural anisotropy after the uniaxial tension and, secondly, to compare measurements on series of magnetically *closed* and *open* samples. Three sample series of different shapes were prepared: *closed* rings, cut from the rods *perpendicularly* to the strain direction, *closed* window-shaped specimens and magnetically *open* strips, magnetized in the *parallel* direction to the strain (see Fig. 2.1). Water-beam cutting was used for the hole drilling in the first two series of the closed samples.

The measurements were performed under full PC control with the simple inductive measuring system (permeameter), described in detail in Refs. [45, 46]. The device scheme for the *closed* sample measurement is presented in Fig. 2.2. Main principles of the measurement and the data

evaluation were published in Ref. [58]. In brief, the presented results were obtained very similarly to the standard methods of measurement, described in introductory Chapter 1. The magnetically *closed* series (rings and windows) were equipped with the driving and the induction windings. Triangular waveform $|\mathrm{d}I/\mathrm{d}t| = const$ was utilized for the magnetizing current $I(t)$. That allows using the chain rule $\mathrm{d}B_s/\mathrm{d}t = (\mathrm{d}B_s/\mathrm{d}H_s)(\mathrm{d}H_s/\mathrm{d}t)$ to rewrite Eqs. 1.1-1.2 as the following:

$$H_s(t) = \frac{N}{l_s} I(t) \tag{2.1}$$

$$U_{ind} = -nS_s \frac{\mathrm{d}B_s}{\mathrm{d}H_s} \frac{\mathrm{d}H_s}{\mathrm{d}t} = -nS_s \mu_0 \mu_{dif} \frac{N}{l_s} \frac{\mathrm{d}I}{\mathrm{d}t} \tag{2.2}$$

The main feature of this kind of the *closed* sample measurement with $|\mathrm{d}I/\mathrm{d}t| = const$ is that the induced signal is proportional to the material differential permeability μ_{dif}. Our principal approach is to take this induced voltage as the basic magnetic output signal, whereas, usually the preferences are given to more stable integral characteristic – the magnetic induction $B = \mu_0 \int \mu_{dif} \mathrm{d}H$. However, despite of the fact that differential permeability is really much more difficult magnetic parameter to be measured, in special cases it can give much deeper understanding of underlying physical nature of the magnetization process. The presented problem of magnetic response to plastic deformation is one of such a case.

In that way the measured induction signal, proportional to the differential permeability, is simply referred to the magnetic field, which is supposed to be proportional to the magnetizing current according Eqs. 2.1-2.2. In the case of the ring it is in agreement with the classical measurement method (see Section 1.1). However, the small ring size and some inhomogeneities of the ring cross-section due to the used water-beam cutting can introduce a measurement error. For the windows-shaped series of samples the magnetic parameters were calculated in a similar way with the magnetic sample path l_s, evaluated as the mean window perimeter. This simplified (and the only possible) method of

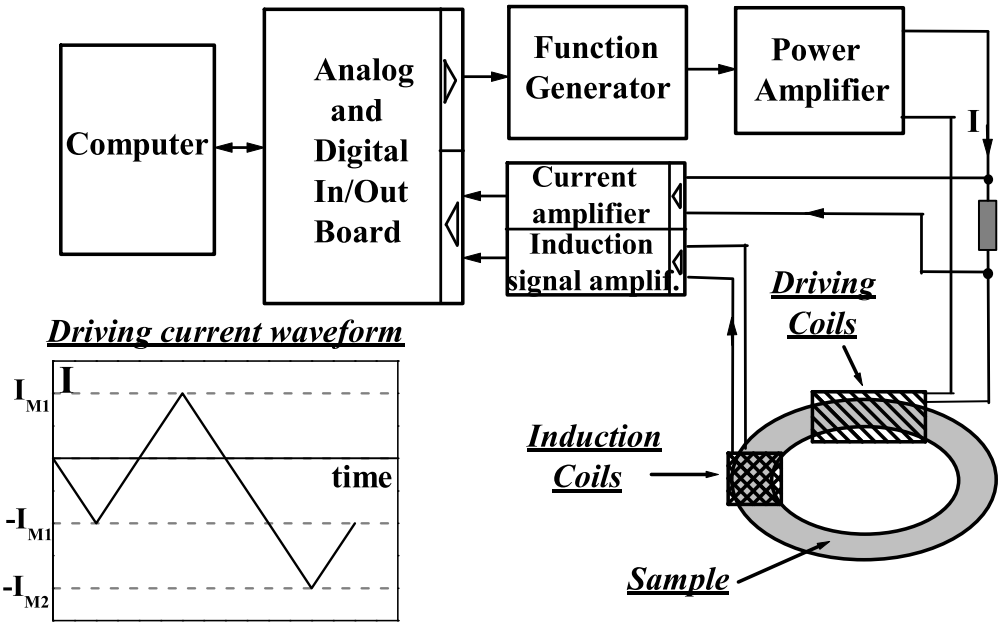

Figure 2.2: Principal scheme of the closed samples measurement.

the magnetic parameter evaluation can also lead to some mistakes due to non-homogenous field distributions on the window edges (for details see Section 2.4.2). The main reason of preparation of the window-shaped series was the necessity to compare the measurements on the *open* strips in the tension direction with some similar series of the *closed* samples. Major loops of the rings and of the windows were measured with nearly quasistatic constant speed $\mathrm{d}H/\mathrm{d}t = 1.2$ and 1.5 kA/m/s, respectively, and with the same field amplitudes $H_m = 4$ kA/m. One of the window samples was measured directly in the Instron for investigation of the magnetic behavior at presence of the applied tension.

The magnetically *open* strips were measured similarly but with an attached magnetizing yoke (see Fig. 2.3). A small Head 1 (see the dimensions in Tab. 2.1) of conventional FeSi transformer C-core was chosen for these measurements. The driving and the induction coils were wound directly on the yoke legs. The field in the samples was assumed again to be simply proportional to the driving current I (according to

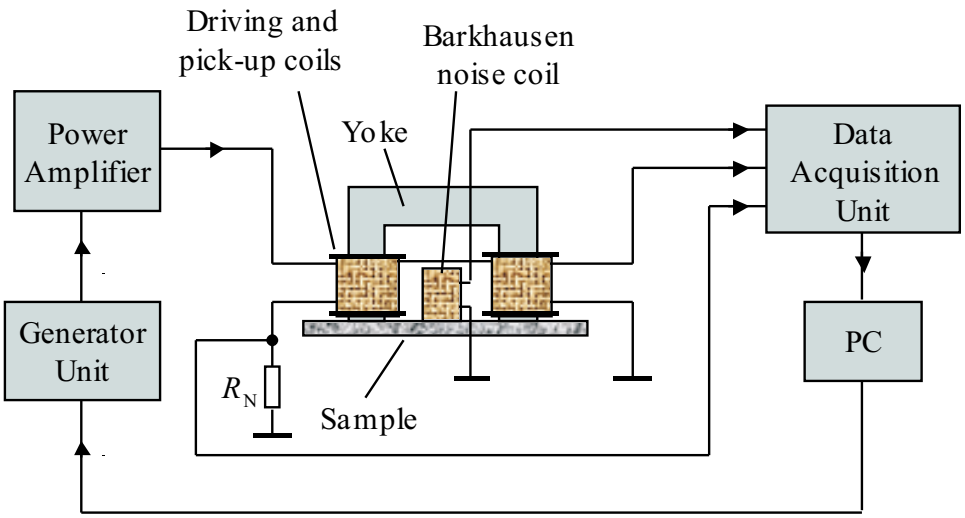

Figure 2.3: Principal scheme of the open samples measurement.

Table 2.1: Head configurations.

Head No	Width L_h mm	Depth Δ_h mm	Height D_h mm	Leg width L_l mm	Cross-section $S_h = L_l\Delta_h$ mm^2	Magn. path l_s mm	Driving and Induction turns N, n
1	28	10	27	8.5	85	14	200
2	39	25	39	10	250	29	200

Eq. 2.1). On basis of the near-saturation field measurements by a conventional Hall sensor above and under the samples the effective magnetic path was defined to be equal $l_s = 14$ mm (the inner and the outer legs distances are 11 and 28 mm). At this stage there was no serious attempt to make the measurements with reference to the sample surface field. However, preliminary measurements of the surface fields were done in order to clarify technical difficulties of realization of this measurement method. The problem of the surface field measurements will be considered in detail in the next Chapter 3. The magnetization speed (the triangular current waveform was used again) was chosen to be high enough $\mathrm{d}H/\mathrm{d}t = 14$ kA/m/s in order to get the stable induction signal. Major loops with the field amplitude $H_m = 5$ kA/m were measured. In order to avoid parasitic jumping of the inspection head during the remagneti-

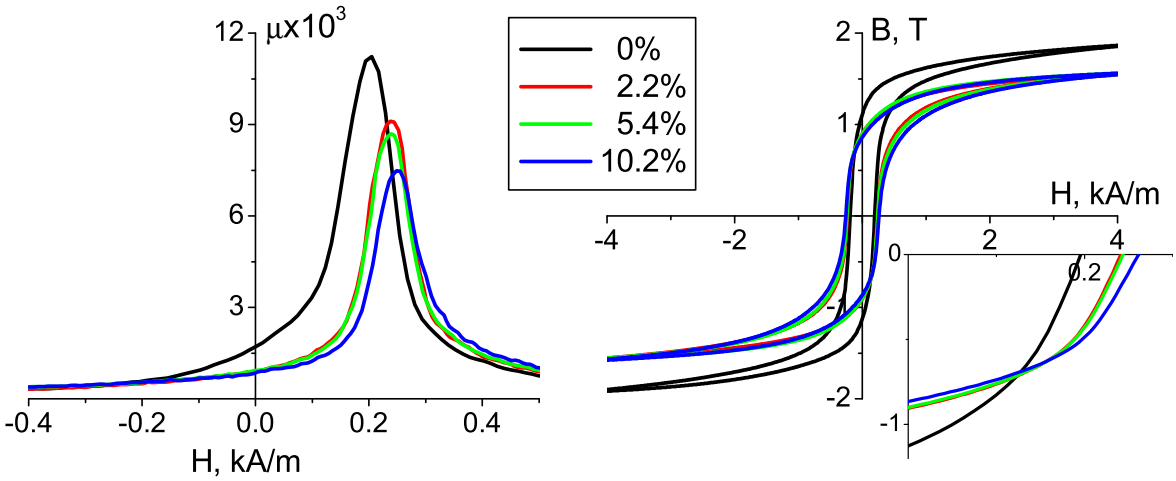

Figure 2.4: Permeability and hysteresis curves for the ring-shaped samples (measured perpendicularly to strain).

zation process, the head was pressed to the polished sample surface by an additional weight.

2.1.2 Major loop measurements

Permeability curves (for one half-loop) and hysteresis loops for the non-deformed and the three deformed samples of the three considered series of the samples are shown in Figs. 2.4-2.6. The sample residual strain ε was calculated through the length changes after unloading. The ring series, magnetized perpendicularly to the stress, showed the standard shape of the permeability curves and the hysteresis loops (Figs. 2.4). The deformed window (Figs. 2.5) and strip samples (Figs. 2.6), magnetized along the stress direction, showed an unusual two-peak form of differential permeability: the first near-horizontal peak at the negative magnetic fields and the second primary peak around the coercive field. The curves are qualitatively very similar to each other but they have their first permeability peak less pronounced for the window-shaped series than for the strips. Moreover, in case of the strip samples, dynamical measurement effects lead to an expected broadening of the permeability curves and of the hysteresis loops on the field, and to a decrease of

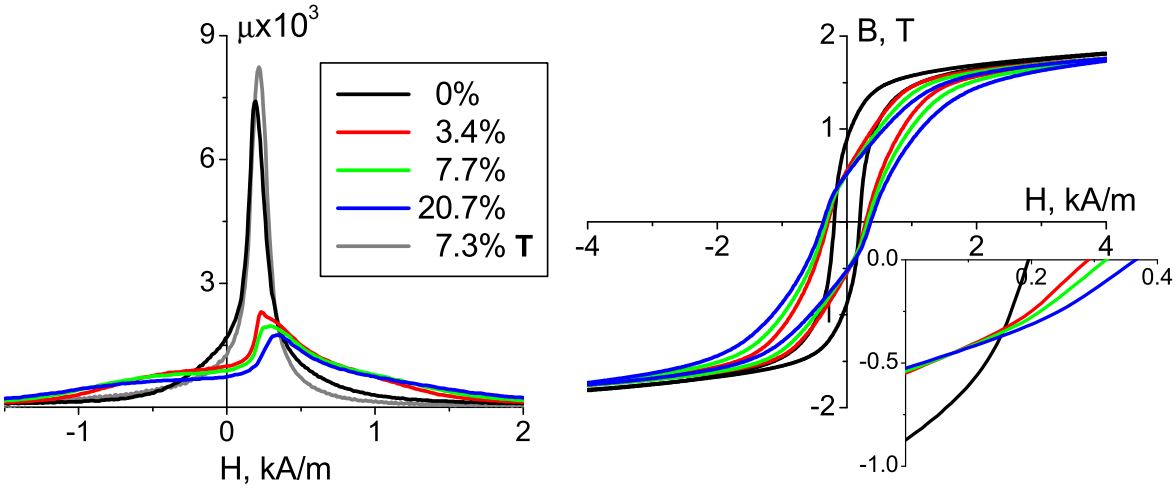

Figure 2.5: Permeability and hysteresis curves for the window-shaped samples (measured parallel to strain). Gray permeability curve presents the measurement at applied tension.

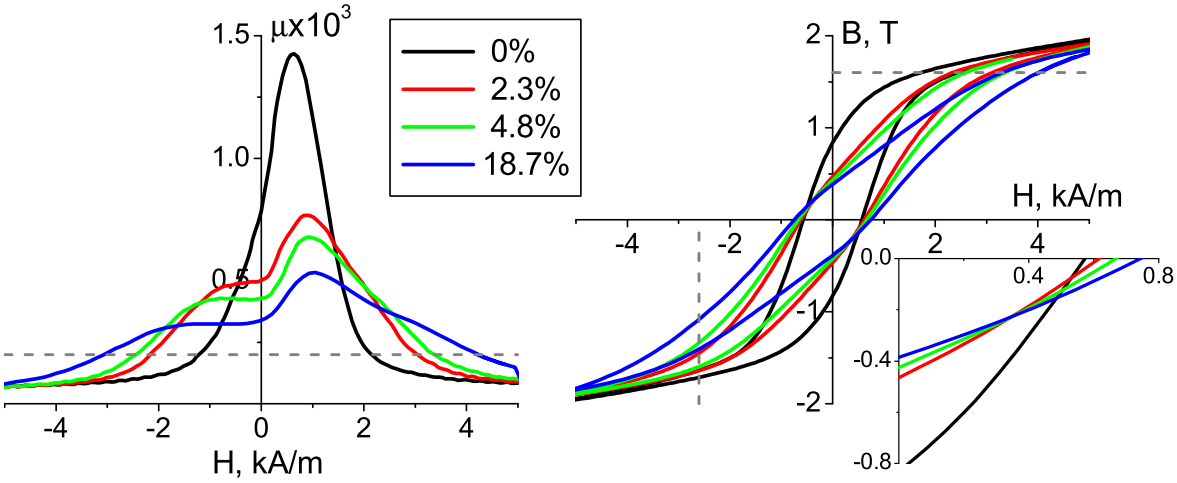

Figure 2.6: Permeability and hysteresis curves for the strip-shaped samples (measured parallel to strain). Horizontal dash lines $\mu = 200$, $B = 1.6$ T and vertical dash line $H = -2.6$ kA/m illustrate the most sensitive magnetic descriptors (see the following Section 2.1.3).

the permeability values. The two-peak profile of the permeability curves leads to a bulged shape of the corresponding hysteresis loops. These loops revolve with the degradation increase around their mutual inter-

section points in the second and the fourth hysteresis quadrants (see the figure insets).

Dependencies of the traditional magnetic parameters (coercive field H_c, remanent induction B_R, and maximum permeability μ_{max}) on strain ε for all the sample series are presented in Figs. 2.7. All the three sample series showed similar parameter behavior. At the initial deformation stage a rapid change of all the parameters was obtained. Then the coercive field H_c (Fig. 2.7(a)) increases monotonically with strain but with a much more moderate slope, whereas the remanence B_R (Fig. 2.7(b)) and the maximum permeability μ_{max} (Fig. 2.7(c-d)) decrease with tendency to saturate. For the strips, the dynamical measurement effects led to increase of the coercive field H_c and to decrease of the maximum permeability μ_{max} (different scales in Figs. 2.7(a) and 2.7(c-d)). Maximum permeability μ_{max} for the window sample in tension was also evaluated (open gray triangulares in Fig. 2.7(c)). At applied tension the maximum permeability μ_{max} increases first and then smoothly drops below the non-stressed value. Due to significant noise of the Instron environment it was a problem to integrate these permeability curves to the hysteresis loops. For the strips the remanent permeability μ_R is shown in Fig. 2.7(d) together with μ_{max}. For the single-yoke measurement with the current method of the sample field determination, μ_R usually shows similar behavior and sensitivity as μ_{max} but a better stability [17].

2.1.3 Minor loop investigation

In this section results of the complex permeability-hysteresis investigation of minor loop magnetic response to the considered structure degradation for the windows and the strips are presented (the case of magnetization parallel to the stress direction). In case of the rings, magnetized perpendicular to the stress, this investigation was done for permeability only (due to small induction signals the integrated minor hysteresis loops were of insufficient quality), and the results were published in Ref. [45]. The main aim of this minor loop investigation was to find new magnetic

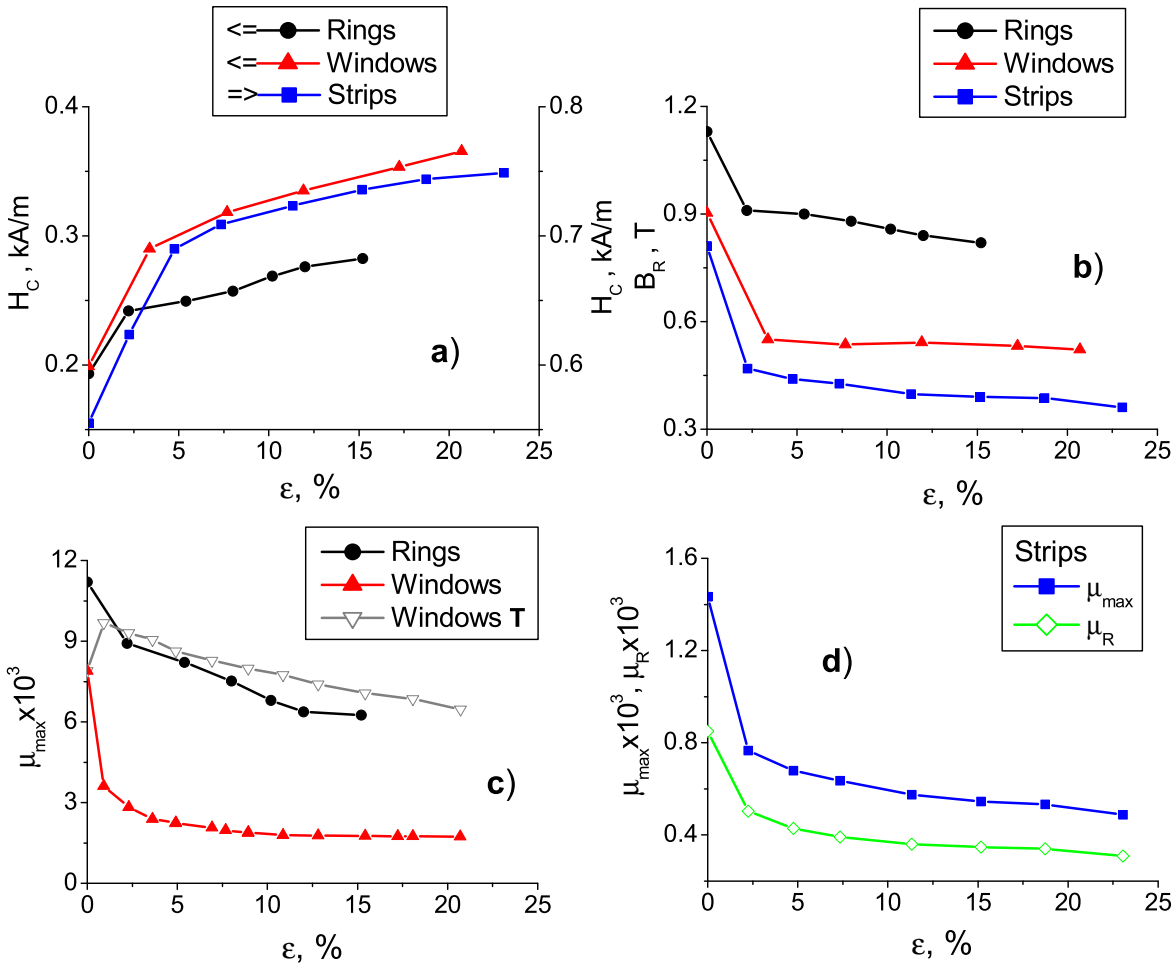

Figure 2.7: Dependencies of the traditional magnetic parameters for all three series of the samples on strain ε: (a) coercive filed H_c (left scale corresponds to the rings and the windows, right scale – to the strips); (b) remanent induction B_R; (c) maximum permeability μ_{max} for the rings and for the windows (also at applied tension – open gray triangulares); (d) maximum μ_{max} and remanence μ_R permeabilities for the strips.

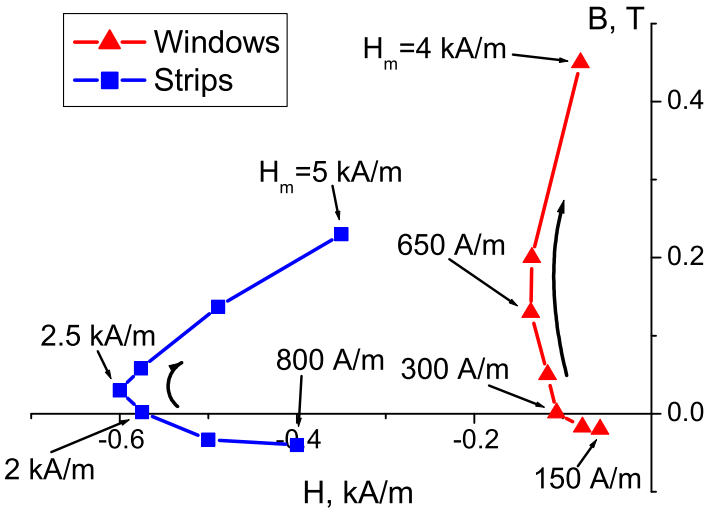

Figure 2.8: Movement of the hysteresis intersection points with the field amplitude.

parameters, which can be utilized and compete with the classically used parameters in magnetic NDT.

Measurements of the minor loop systems were done in the same way and with the same magnetization speeds as the corresponding measurements of the major loops. Families of 50 minor loops with the field amplitudes H_m from ± 20 A/m up to the maximal amplitude ± 1 kA/m and from ± 100 A/m up to ± 5 kA/m for the windows and for the strips, respectively, were measured. The minor loops show similar tendencies to the corresponding major ones: two-peak profiles of permeability, which become more pronounced at higher field amplitudes H_m, and near-the-same hysteresis intersection points. In the initial magnetization stage, when the minor loops have a lentil form (Rayleigh region), the intersection points are in the first and the third hysteresis quadrants. Then with the field amplitude increase they move to the second and the forth quadrants as is shown in Fig. 2.8.

Data of the measured *upper halves* of the minor loops families, i.e. for the field H changing from negative towards positive values, were transformed into permeability and hysteresis matrices with the same field-step in both directions. The two coordinates of the matrices are

the actual field value H (matrix rows) and the field loop amplitude H_m (matrix columns). An example of such a permeability matrix $\mu(H, H_m)$ at different view angles is presented in Fig. 2.9. An example of a hysteresis loop matrix $B(H, H_m)$ is shown in Fig. 1.6. The search of the most suitable magnetic descriptors of the investigated structure alteration was done on the basis of an expanded MAT method [41] (see Section 1.2). In a few words, MAT works with minor loops families (i.e. with the calculated $\mu(H, H_m)$ or $B(H, H_m)$ matrices) and searches for those elements of the matrices, which are the most sensitive with respect to the investigated material structural modifications (i.e. to the tensile strain ε in our case). In this work the originally proposed method [41] was also expanded to the search for the most sensitive field H parameter in the converse planes (μ, H_m) and (B, H_m). Dependencies of the degradation functions $\mu(\varepsilon; H, H_m)$, $B(\varepsilon; H, H_m)$ and $H(\varepsilon; B, H_m)$ of the tested structure degradation, described by the strain value ε, were considered on the two-parametric planes $(H/B, H_m)$. Sensitivity of each of the degradation functions (only monotonous dependencies on ε were taken into account), was evaluated as the sum of the degradation function changes for the neighboring degraded specimen, i.e. $\sum_{\Delta\varepsilon} |B(\varepsilon + \Delta\varepsilon; H, H_m) - B(\varepsilon; H, H_m)|$. Since a much larger difference of the magnetic descriptors between the non-deformed and the deformed samples prevails over the corresponding difference between the deformed samples, i.e. $B(\varepsilon) - B(0) \gg B(\varepsilon + \Delta\varepsilon) - B(\varepsilon)$ (e.g. see Figs. 2.5-2.7), the non-deformed samples were excluded from this sensitivity evaluation.

The results of such an evaluation are presented in the form of sensitivity maps in Figs. 2.10-2.12 for the series of the window-shaped (a) and the strip-shaped (b) samples. The absolute values of sensitivity do not have much physical meaning but their relative values are shown. White areas inside the minor loops triangles correspond to the excluded regions of non-monotonous dependencies of the degradation functions.

The permeability sensitivity map of the window series (see Fig. 2.10(a)) showed results similar to the same material series of the ring samples, cut in the perpendicular direction to the strain [45]: the most sensitive area

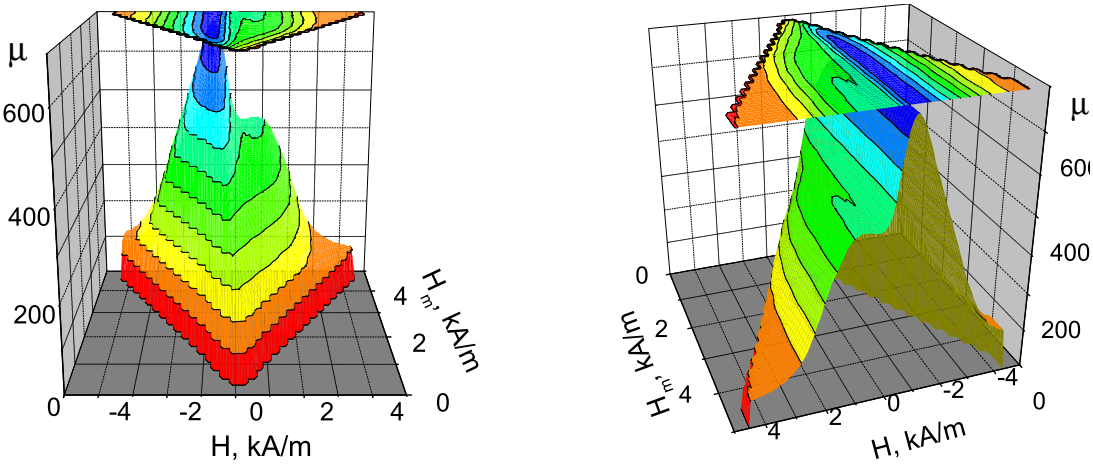

Figure 2.9: 3-D presentation and 2-D projection of the permeability matrix for the strip sample, deformed to 4.8% of strain.

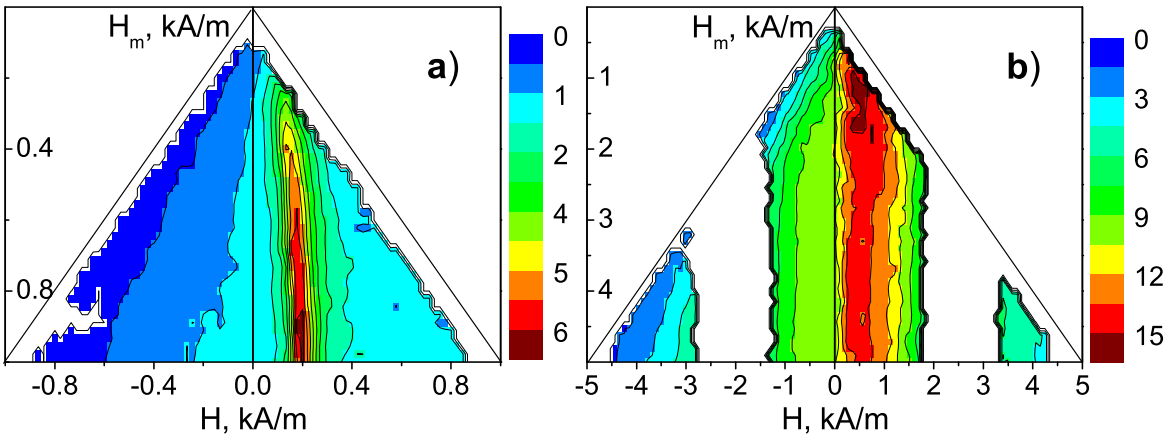

Figure 2.10: Permeability sensitivity maps $\mu(H, H_m)$ for the window-shaped (a) and the strip-shaped (b) series.

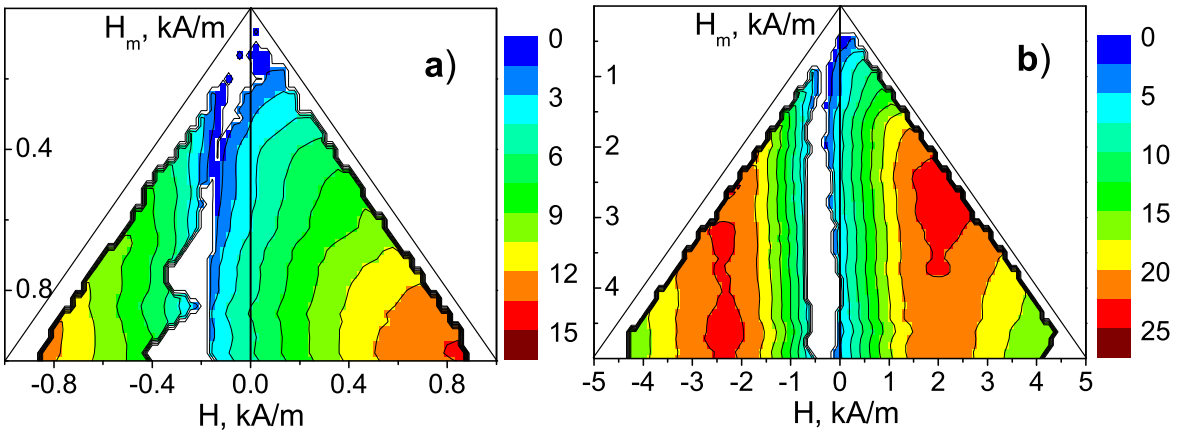

Figure 2.11: Induction sensitivity maps $B(H, H_m)$ for the window-shaped (a) and the strip-shaped (b) series.

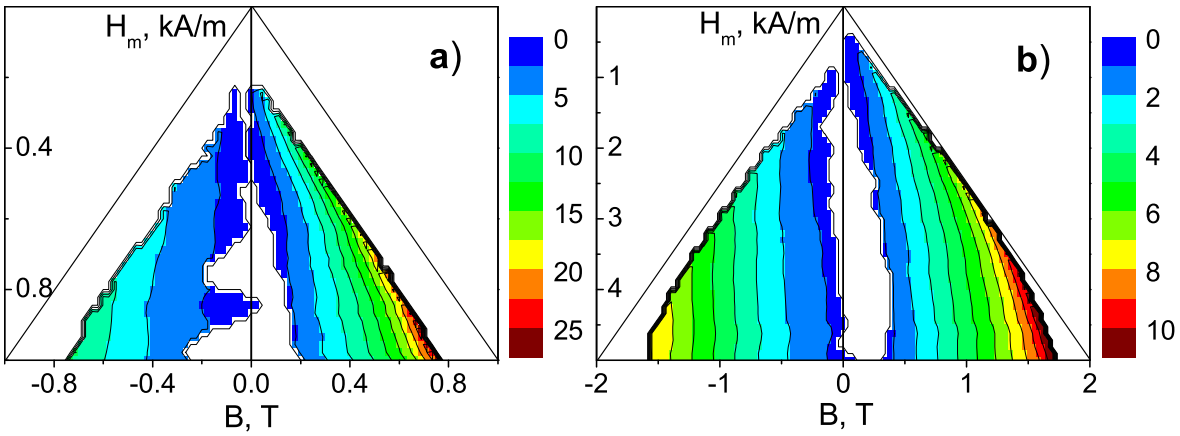

Figure 2.12: Field-to-induction sensitivity maps $H(B, H_m)$ for the window-shaped (a) and the strip-shaped (b) series.

is narrow and corresponds to the region of growing permeability. Sensitivity of this narrow region increases steadily with H_m, so that the maximum sensitivity point corresponds to the major loop. In contrary to this, the $\mu(\varepsilon; H, H_m)$ maximum sensitivity for the strips was found to be at $(H = 0.6, H_m = 1.3)$ kA/m field point, though the sensitivity drops only slightly with the H_m increase. The sensitive area is much wider than that for the window samples. The most sensitive $\mu(\varepsilon; H, H_m)$-MAT curves are very similar to the dependencies of the classical saturation μ_{max} parameter with its poor sensitivity at high strains (see Fig. 2.13(a)). However, the residual plastic tension can be magnetically indicated with good sensitivity by broadening of the permeability curves due to the appearance of the two peaks. As the first peak becomes clearer with larger field amplitudes (e.g. it can be seen from Fig. 2.9), the saturation permeability curve gives the best results. In Fig. 2.13(b) the permeability curves width at two fixed values of permeability (one of these values $\mu = 200$ is shown by a gray dash line in Fig. 2.6) together with the permeability width at the half-height $\mu = \mu_{max}/2$ for the strip series are shown versus strain ε. It can be seen that the permeability curve width is sensitive to the tensile plastic deformation and it shows near-linear growth at high strains. For the window samples the dependencies are very similar but less sensitive and stable on the (H, H_m) plane.

The most sensitive regions of the $B(\varepsilon; H, H_m)$ functions (see Figs. 2.11) are in the right (positive) side of the maps (loops). The sensitivity map for the window series seems to correspond to the non-saturated part of the sensitivity map for the strip series (up to about $H_m = 3$ kA/m). The most sensitive point $(H = 1.9, H_m = 2.6)$ kA/m for the strip samples is again below saturation. However, with H_m increase to near the saturation the left hand-side sensitive region becomes comparable in sensitivity with the right one (at value $H = -2.6$ kA/m, shown by a vertical gray dash line in Fig. 2.6). These most sensitive $B(\varepsilon; H, H_m)$ degradation curves together with the classical saturation remanent induction $B_R(\varepsilon)$ are shown in Fig. 2.14(a).

The search in the $H(\varepsilon; B, H_m)$ plane (see Figs. 2.12) was done in the B

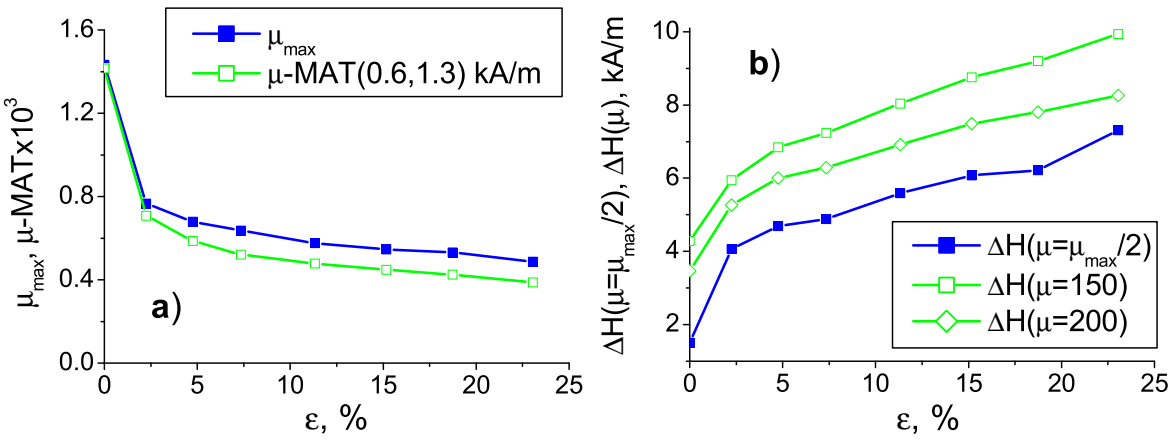

Figure 2.13: μ-MAT parameter compared to μ_{max} (a) and $\Delta H(\mu = const)$ parameters compared to $\Delta H(\mu = \mu_{max}/2)$ (b) versus strain ε for the strip series. Similar trends were found for the window series.

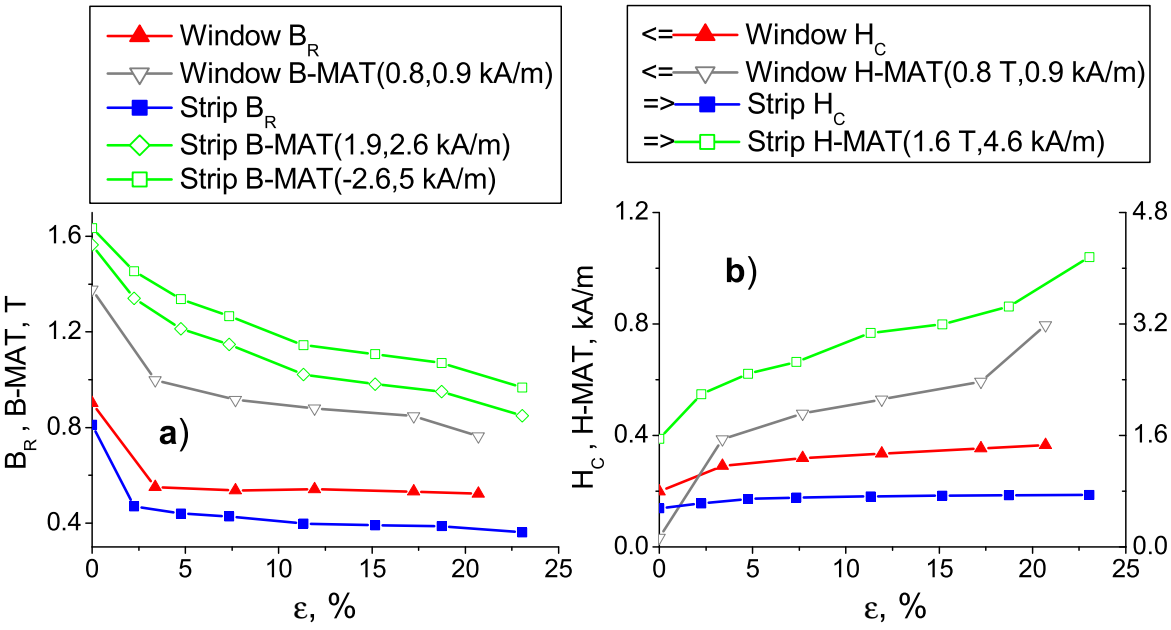

Figure 2.14: $B(H, H_m)$-MAT parameters compared to B_R (a) and $H(B, H_m)$-MAT parameters compared to H_c (b) (the left scale corresponds to the window series, the right scale – to the strips) versus strain ε for the window and the strip series.

range up to the maximum induction for the most deformed sample. The sensitivity maps showed the most sensitive area to be very narrow and to be positioned at the maximum values of B and H_m. The corresponding degradation curves together with the dependencies of the classical saturation coercive fields H_c are shown in Fig. 2.14(b) (the working field point $B = 1.6$ T for the strips is shown by a horizontal gray dash line in Fig. 2.6).

2.2 Barkhausen noise measurements

2.2.1 Experiment

Together with the magnetic hysteresis measurements the BN effect was also utilized in order to obtain the most full picture of the investigated problem. The BN phenomenon arises from discontinuous changes in the flux density B within a ferromagnetic material as the magnetic field H is changed continuously. The physical reason is *discontinuous* domain boundary motion (mostly) and *discontinuous* rotation of the direction of magnetization within a domain [39]. The BN emission is greatly affected by changes in the microstructure of the material, e.g. caused by mechanical stress. Therefore, BN measurements have found an important role in ferromagnetic material evaluation [17, 59, 60].

The rings and the windows were measured classically, similarly to the hysteresis measurements: with the same driving and BN induction coils, wound directly on the samples. The magnetic quasistatic measurements were done again with the triangular waveform current. For the rings and the windows the magnetization speeds were chosen to be $\mathrm{d}H/\mathrm{d}t = 0.5$ kA/m/s and 0.9 kA/m/s, with the field amplitudes equal $H_m = 1.2$ kA/m and 2 kA/m, respectively. The low values of the amplitudes could be used due to the fact that for the BN measurements there is no need of the sample saturation – majority of the BN jumps takes place near H_c. The BN signal was filtered by an analog band-pass filter in the ranges of 1-30 kHz and 0.1-100 kHz for the case of the rings and

the windows, respectively.

However, to measure the BN on the magnetically *open* samples is, similarly to the hysteresis parameters, not an easy task. At the moment there is no standard widely-accepted technique. In laboratory experiments the *open* samples are usually evaluated with a magnetizing single-yoke setup [17, 59, 60]. But quite different approaches are used to obtain the BN induction signal. It can be measured either classically by an induction coil [48, 60], wound directly around the sample body, or by different induction read-coils [52, 59], attached to the sample surface to pick up the normal component of the stray flux. In this work the latter method with the original BN read-head (the sensing coil of 2000 turns, wound around the core of stacked soft amorphous ribbons) was utilized as is shown in Fig. 2.3. The coincidence of measurement results, obtained with the used BN sensor and by the classical method of the induction coil, wound around the sample, was previously checked experimentally [61]. The advantage of this sensor is its much higher output signal due to magnetically softer material of the used amorphous ribbon as compared to the frequently used ferrite or air cores. In contrast to the hysteresis measurements, a magnetically harder U-yoke, made from the same low-carbon steel material, was used. It is an acceptable substitution because there is no need of the sample saturation. The reason was to avoid the parasitic jumping of the yoke influencing the sample magnetization conditions. The magnetization speed was chosen in quasistatic range again $\mathrm{d}H/\mathrm{d}t = 0.6$ kA/m/s with the field amplitudes $H_m = 1.2$ kA/m. The cut-off frequencies of the filter were 0.1-100 kHz.

For next investigation of the magnetic behavior in the perpendicular direction to the previous tension, the BN measurements with external AC magnet were done (see the scheme of the setup in Fig. 2.15). Unfortunately, this type of measurements can not be repeated for the hysteresis in this sample configuration. For the used external magnet the magnetization speed $\mathrm{d}H/\mathrm{d}t \approx 10$ kA/m/s and the field amplitude $H_m \approx 10$ kA/m can be evaluated only approximately. The surface field measurements with a Hall sensor were also used for that. However, the

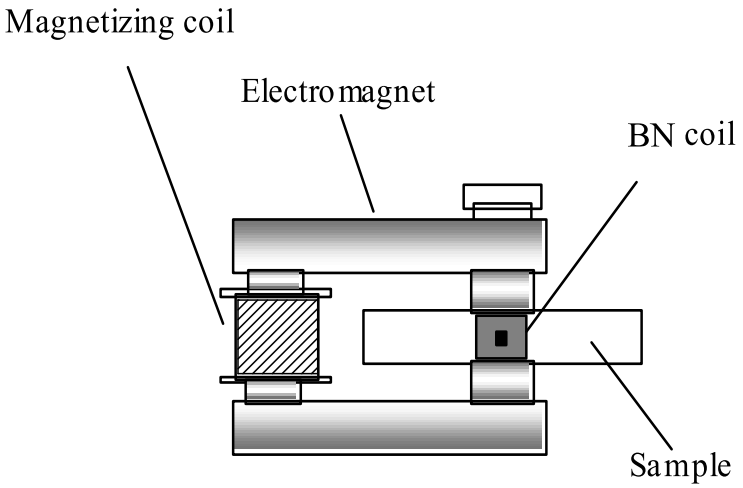

Figure 2.15: Scheme of BN strip measurements in the perpendicular direction to strain.

obtained results are of a high qualitative importance for proving the results of measurements on the ring series.

The main barrier to the way of industrial application of the BN measurements for evaluation of the material degradation is an absence of generally accepted BN parameters, stable and unified, for this task. BN parameters, evaluated in this work, were the Root Mean Square (RMS) value of BN and the BN envelope, widely used as physical descriptors of the BN effect. The RMS values were obtained from one remagnetization period. Every point of the BN envelope was calculated as the RMS value of one hundred noise voltages within a constant time interval. The resultant envelopes were smoothed by a digital low pass filter.

2.2.2 Results

Dependencies of the envelopes and the RMS values of BN on strain ε for all three series of the samples are shown in Figs. 2.16–2.18. The BN envelopes showed qualitatively similar behavior to the differential permeability curves, what proves their theoretically-suggested proportional correlation [62, 63]. In case of the rings the envelopes have usual one-peak profile (see Fig. 2.16), whereas in case of the windows and

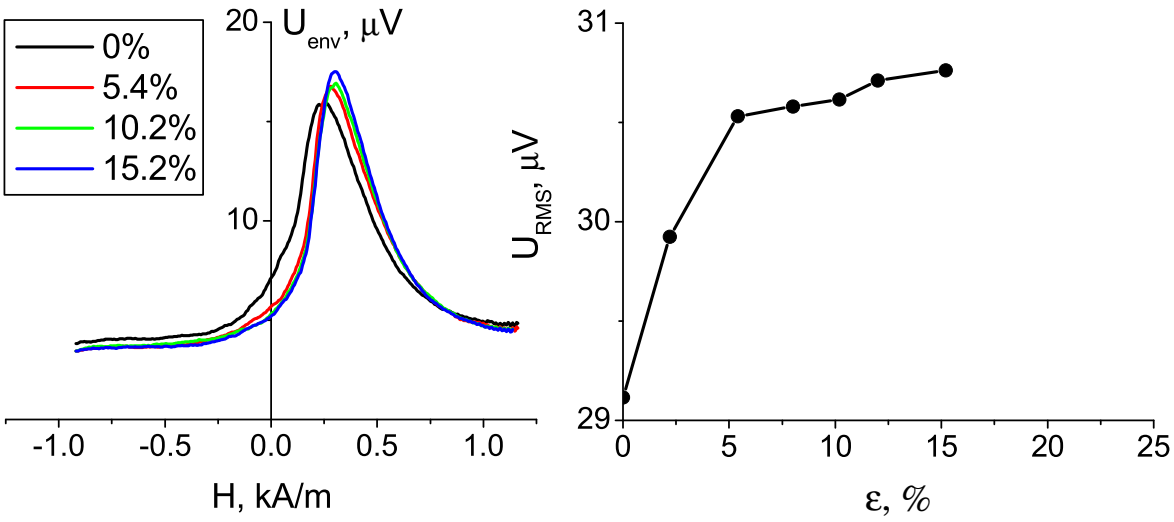

Figure 2.16: Envelope U_{env} and RMS value U_{RMS} of BN for the ring-shaped samples (measured perpendicularly to strain).

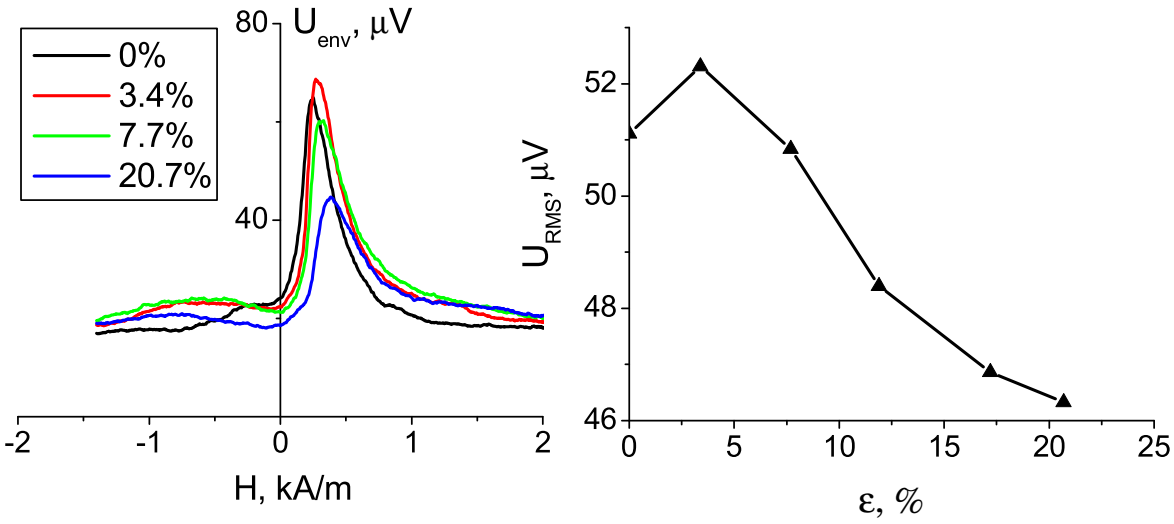

Figure 2.17: Envelope U_{env} and RMS value U_{RMS} of BN for the window-shaped samples (measured parallel to strain).

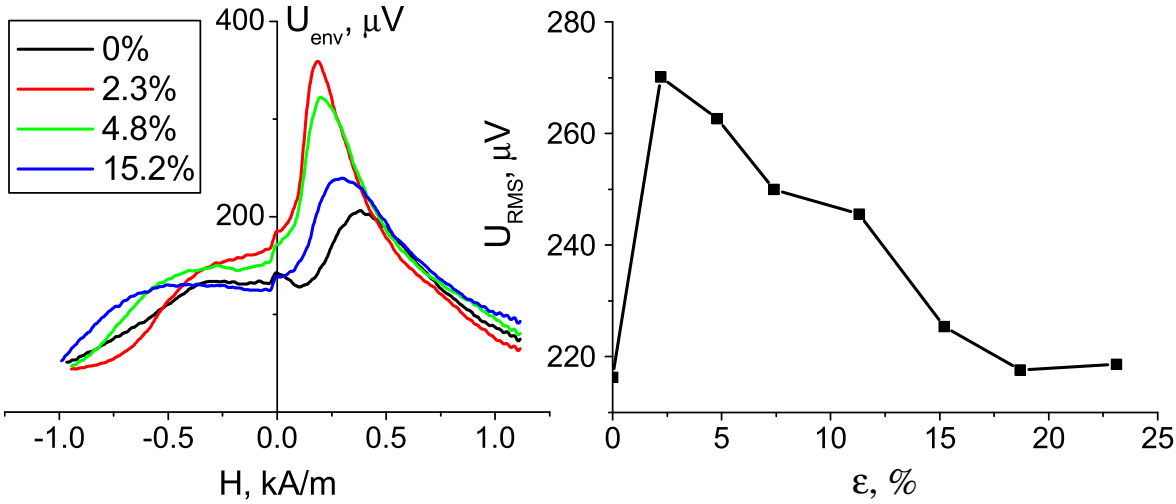

Figure 2.18: Envelope U_{env} and RMS value U_{RMS} of BN for the strip-shaped samples (measured parallel to strain).

the strips they show, similar to permeability, two-peaks behavior (see Figs. 2.17 and 2.18). But there are two visible distinctions. The first one is a slightly pronounced two-peak form of the BN envelopes for the *non-deformed* samples of the windows and the strips. The second distinction is the lack of coincidence between the field values of BN envelope maximum $H(U_{env}^{max})$ and H_c for the strip sample series. All other envelopes (and all the permeability curves) obey the rule $H(\mu_{max}) \simeq H(U_{env}^{max}) \simeq H_c$. The reason is in incorrect determination of the strip sample field. The effective magnetic sample paths l_s are quite different for the undeformed and the deformed specimens. For the undeformed sample it is close to the chosen total magnetic path $l_s + l_h$ due to the same material of the yoke and the sample (l_h is magnetic head path). However, with the material degradation the effective sample path gradually decreases. According to the envelope peaks comparison with H_c the realistic magnetic path for the deformed strip specimens should be 2–3 times smaller. Detailed analysis of this topic is done in the next Chapter 3.

The RMS values of the BN increase after deformation over the yield point ($\varepsilon_{yield} \simeq 2\%$) for all three types of the samples. In cases of the win-

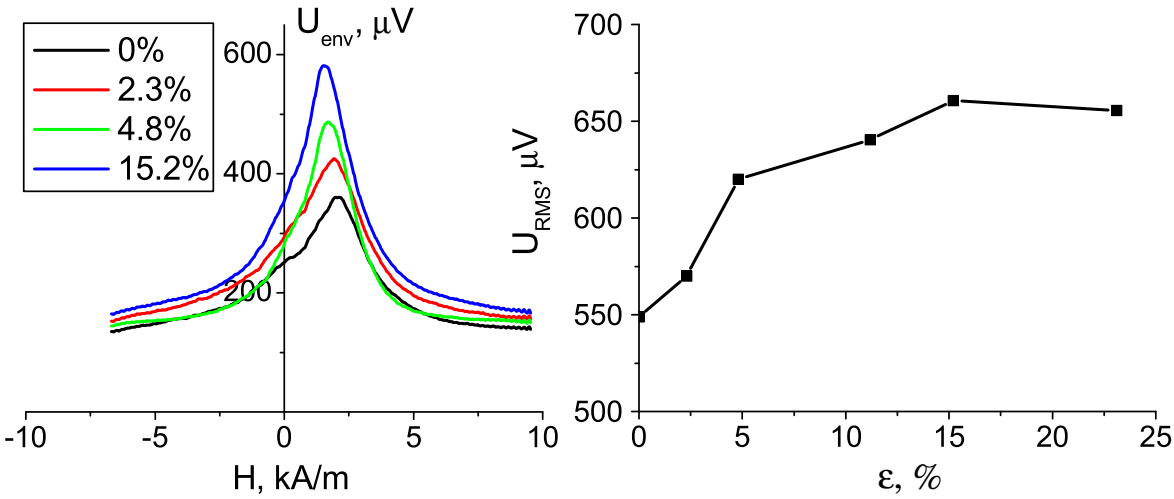

Figure 2.19: Envelope U_{env} and RMS value U_{RMS} of BN for the strip-shaped samples (measured perpendicularly to strain).

dows (Fig. 2.17) and the strips (Fig. 2.18), the RMS dependencies start to decrease just after this initial increase. On the contrary, for the case of the rings (Fig. 2.16), the RMS dependence continues to rise further in all the investigated deformation range but with a slope decrease.

Results of the BN measurements of the strips with magnetization in the perpendicular direction to the tension (AC magnet – see Fig. 2.15) are presented in Fig. 2.19. Despite of the expectable mistakes of the sample field determination for the used measurement configuration, these results are qualitatively very important because they have supported the measurements on the ring series: the usual one-peak profile of the BN envelope and the increase of the RMS value up to 15% of strain were observed in the case of the perpendicular magnetization to the strain.

2.3 TEM

Thin foils were cut in the surface plane of the strip samples for a TEM structure check-up. Figs. 2.20 show the TEM micrographs at four different deformation stages. It can be seen that the non-deformed material (Fig. 2.20(a)) contains only a small number of isolated disloca-

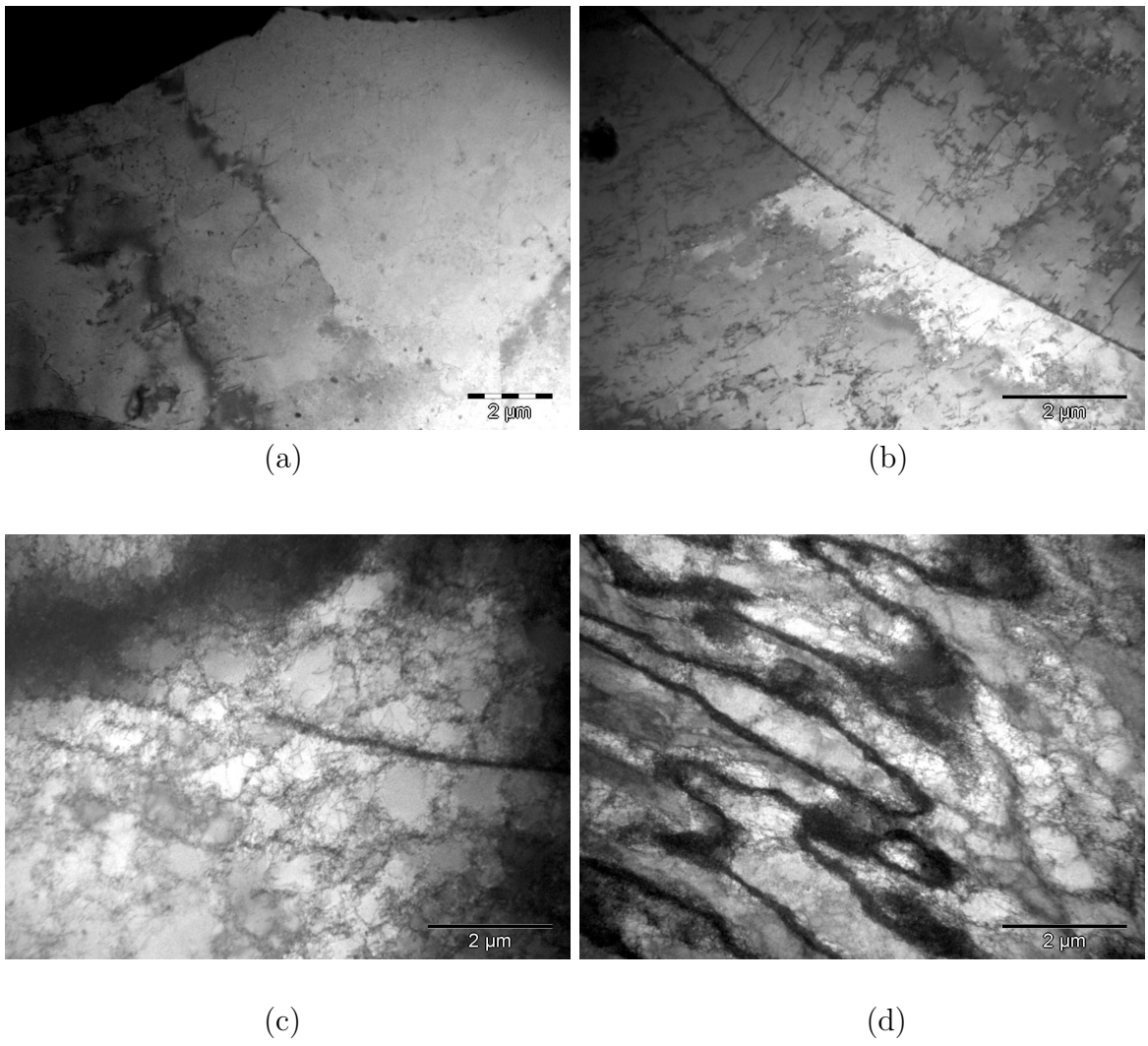

(a) (b)

(c) (d)

Figure 2.20: TEM micrographs of the strip samples, deformed to 0% (a), 2.3% (b), 4.8% (c) and 11.2% (d) of strain.

tions and of any other structural imperfections. The TEM pictures for the deformed samples agree with the known behavior for such low-carbon steels [64, 65]. With deformation the dislocation density increases steadily. For the sample, strained to 2.3% (Fig. 2.20(b)), the dislocation structure is represented by a more-or-less homogenous distribution of isolated dislocations and of small dislocation tangles. At higher strains, the dislocation tangle structure is formed (Fig. 2.20(c)) finally transforming

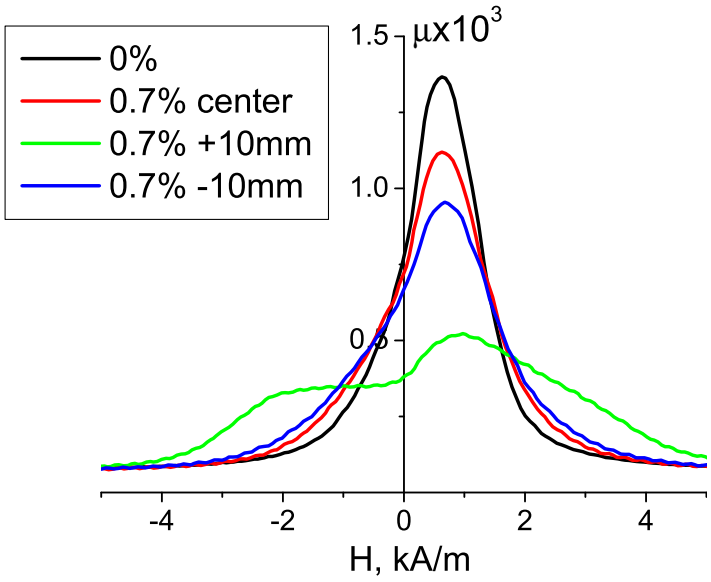

Figure 2.21: Measurement of the strip sample, strained at 0.7% in the Lüders region, with differently positioned yoke (in the center of the specimen and with the displacement to ±10 mm to the both ends).

into the strongly heterogeneous dislocation cell system (Fig. 2.20(d)), which is developed in definite slip directions.

2.4 Discussion

2.4.1 Physical analysis

Tension below the elastic limit is reversible - magnetic measurements after unloading give the same results as for the non-stressed case [66]. Further in the Lüders region (up to $\varepsilon \approx 2\%$) the dislocation multiplication fronts are locally spreading from the sample ends through the specimen's body [67]. The non-homogeneity of plastic deformation within the sample material leads to substantial variation of the measurement results in dependence on the attached yoke position (see Fig. 2.21). After the Lüders region a macroscopically homogeneous dislocation structure is formed throughout the whole specimen(see Fig. 2.20(b)), which stabilizes the measurements.

Dislocation tangles/cells refine the ferrite grain structure: the regions with small dislocation density (ferrite) are separated by the regions with high dislocation density (tangles) as is shown in Figs. 2.20(c-d). As a result, the corresponding refinement of the magnetic domain structure is expected to occur: grain boundaries as well as dislocations are known to be strong pinning sites for the domain walls [39, 68]. For magnetic behavior this refinement has similar consequences as a decrease of the grain size, which leads to the obtained rapid increase of the coercive field H_c, and to the decrease of the maximum permeability μ_{max} and of the remanent induction B_R at the initial deformation stage $\varepsilon \simeq 2 - 5\%$ [69]. The observed behavior of the magnetic parameter can be also explained by a statistical theory of rigid 180° domain walls motion, which states that the inverse initial permeability (usually behaves similar to $1/\mu_{max}$) and the coercive field H_c are proportional to the square root of dislocation density [25, 70, 71].

In the initial stage of the plastic deformation the dislocation structure is mainly presented by isolated dislocations and by small dislocation tangles (Fig. 2.20(b)), which are still surmountable obstacles for the domain wall motion. This leads to increase of the number of irreversible magnetization processes and consequently to the observed increase of the RMS value of BN (see Figs. 2.16-2.18). With higher strain the dislocation density increases steadily but with a decelerating rate. The corresponding change of the magnetic parameters becomes also slower as compared to the initial deformation stage. A large number of domain walls becomes immovable resulting in a decrease of the number of irreversible magnetization processes (i.e. of the RMS value of BN and of permeability) for the case of the window and the strip samples. However, for the ring samples the RMS value continues to rise monotonically, although the slope slows down with higher strain. This different behavior is caused by the second essential factor influencing the magnetization process of plastically deformed steels, namely the magneto-elastic coupling with residual internal stresses.

Magnetic properties of ferromagnetic materials are known to be sub-

stantially dependent on stress [6, 7]. In case of material with positive magnetostriction (e.g. iron-based steel) an uniaxial elastic/plastic tension creates magnetic easy axis along the stress direction due to the magneto-elastic coupling. This increases the permeability (see the gray curves in Figs. 2.5 and 2.7(c)) and BN envelope peak [48] if the magnetization proceeds in the tension direction. The magnetization process mainly occurs by motion of 180° domain walls, which are favored by the tensile stress [68]. After *unloading*, the volumes of the small dislocation density (major areas, where domain wall motion mostly takes place) undergo opposite *compressive* internal stress than the harder areas (dislocation tangles, which act as the strong pinning centers) – total residual stress should be equal to zero. Presence of the *residual compressive stresses*, directed along the previous tension, was confirmed by plastic fatigue experiments [72], by X-ray [73] and neutron [74] diffraction measurements. The effect is symmetrical with respect to the stress sign: after uniaxial plastic compression there are residual tensile stresses in the compression direction [73]. Little is known about residual stress distribution in the transversal direction to the previous plastic tension. Neutron diffraction measurements showed either negligible or small tensile residual stresses in that direction [74].

In case of the magnetization *along* the stress direction, *under tensile load* the permeability (see the gray curve in Fig. 2.5) and the BN envelope [48] exhibit a usual single peak profile, whereas *after unloading* the two-peak profiles were obtained (see Figs. 2.5-2.6 and 2.17-2.18). The same two-peak curves were observed *under compressive load*, and the single peak curves were observed *after unloading from compression* [48, 50, 51], which proves the stress-driven nature of the phenomenon. Moreover, for the nickel-based alloys the effect of residual/applied stress is known to be opposite to the presented here due to negative magnetostriction of nickel [7, 51].

The two-peak form of the permeability (leading to the hysteresis loop bulging) and of the BN envelope has been explained in literature [8, 48] to be due to division of the magnetization process into

two stages. Firstly, even at negative fields the 90° domain wall motion, favored by magneto-elastic coupling with the compressive residual stresses [7, 68], occurs. This determines the first permeability (BN envelope) peak. Then, around the coercive field value, the 180° domain wall motion takes place, which defines the primary second peak. Another interesting magnetic property is that the initial point of the 90° domain wall motion (starting point of the first peak) is shifted to higher negative magnetic fields with the strain (increase of the proposed $\Delta H(\mu = const)$ MAT parameter – see Fig. 2.13(b)). This is apparently caused by increase of compressive residual stresses with higher deformation level. Less pronounced two-peak behavior of the BN envelopes for the non-deformed samples of the window and the strip is, evidently, explained by smaller but existent contribution of the 90° domain wall motion due to small residual stresses in the rolling direction. This means that the BN envelope is more sensitive to distinguish these two magnetic phases than the magnetic permeability. The second primary peak decreases with the strain and moves to higher fields according the H_c dependence (see Figs. 2.7(a)).

In case of the ring samples, when the magnetization is applied in the *perpendicular* direction to the previous elongation, the magnetization process takes place standardly by motion of the 180° domain walls mainly. Therefore, the permeability and the BN envelope have only the second peak. From that it can be concluded about absence of any significant compressive stresses in the perpendicular directions. Thus the small monotonous increase of the BN RMS with the strain for the rings is evidently explained by slight predominance of the 180° domain wall motion over the domain wall pinning on the dislocations (see Fig. 2.16). This 180° domain wall motion is favored by the compressive stresses in the axial direction moving the magnetic easy axes away to the transversal direction [79] and probably by the magneto-elastic coupling with the tensile residual stresses in the transversal direction. However, it is worth to mention that recently Dhar et al [52] obtained a peak-like dependence of the BN RMS, similarly to our results for the windows and the strips,

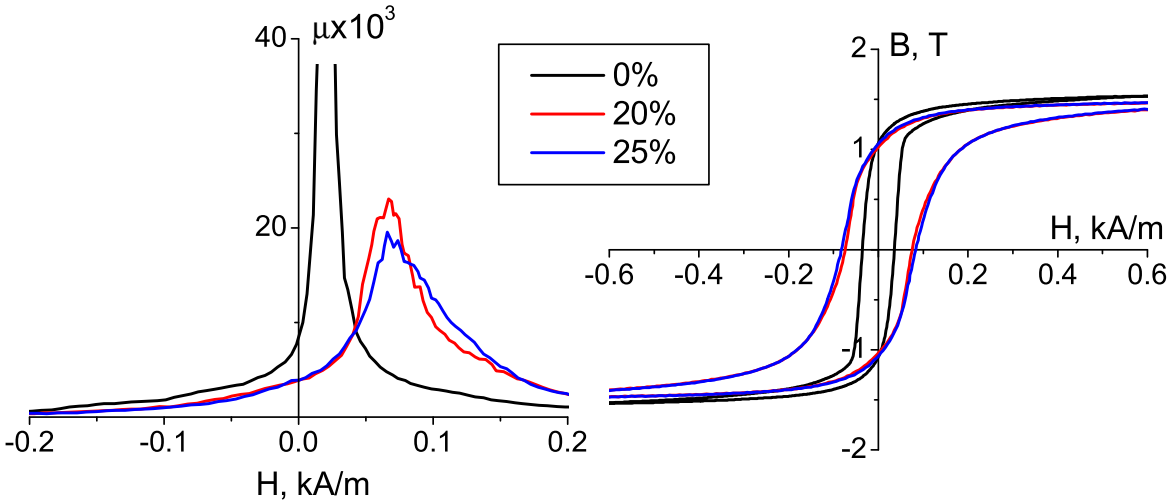

Figure 2.22: Permeability and hysteresis curves for closed rectangular-frame samples of iron single crystal (cut along the tension plane after unloading) [76]. The data are presented with kind approval of S. Takahashi.

for another mild steel in the *both* magnetization direction. But for the considered case of magnetization in the *transversal* direction, this peak behavior was much less pronounced than for the parallel magnetization direction. Different directional distribution of the residual stresses is probably also responsible for smaller sensitivity of the traditional magnetic parameters for magnetization in the transversal stress direction (see Figs. 2.7 and [75]).

The magnetic-stress behaviour is also substantially dependent on the steel composition. Analysis of the literature, our experimental data and the data, kindly provided by Prof. S. Takahashi's group [66, 76], give the following picture. Iron single crystals, magnetized *along* the direction of uniaxial tensile deformation after *unloading*, do not show the discussed two-peak shape of permeability. The hysteresis loops simply widen with the strain without bulging (see Fig. 2.22). Our recent measurements on nickel single crystal, uniaxially compressed and unloaded, show similar results in the stress direction (see Fig. 2.23). This behavior is evidently explained by different dislocation and/or residual stress pattern/s. Domain structure of these single crystals is known to be large-scale ribbon-

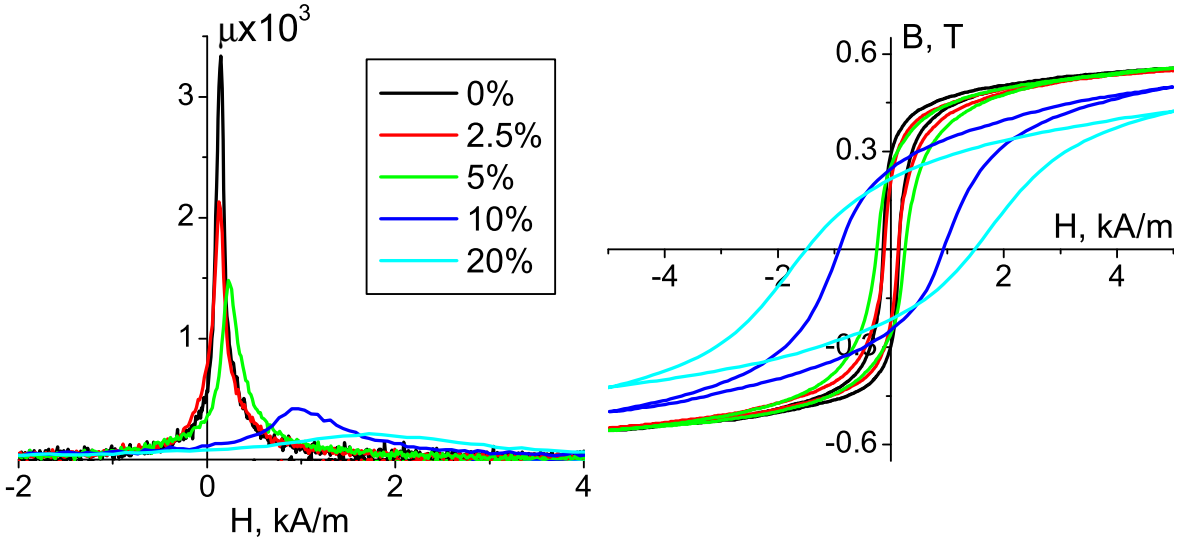

Figure 2.23: Permeability and hysteresis curves for closed rectangular-frame samples of nickel single crystal (cut along the compression plane after unloading). Unpublished data.

shaped, determined by the dislocation slip system [68]. This structure is mostly formed by spatially large 180° domains. However, pure polycrystalline iron does show the hysteresis bulging and the 90° domain wall magnetization at negative fields in the form of monotonously growing permeability, rather not distinct plateau-shaped peak (see Figs. 2.24). It is worth noting that the investigated steel is also a polycrystalline material with the grain size about 50 μm [64] and a very different domain structure from the single crystal cases. The principal crystal axes of different grains are distributed randomly. Each grain contains a number of 180° domain walls, aligned along easy magnetization direction and closed at their edges by 90° domain walls [7], which are responsible for the first permeability/BN envelope peak.

According to the literature review the discussed hysteresis bulging behavior as well as the two-peak shape of the permeability/BN envelope seem to be typical for the low-carbon steels only, approximately up to C $\simeq 0.15 - 0.2$ *wt.*% [8, 48, 51, 76]. For the harder steels the first peak of permeability (and consequently of the BN envelope) is known

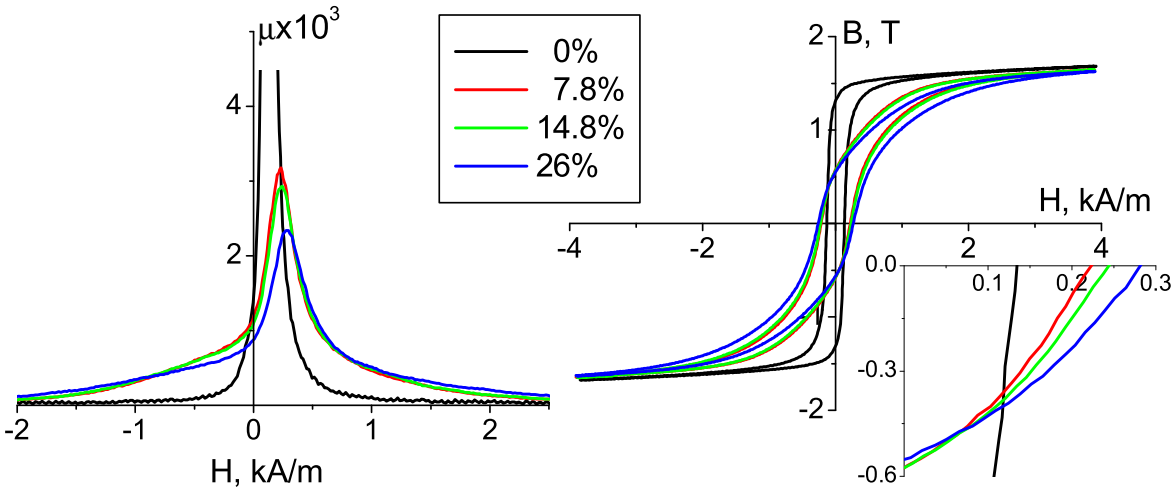

Figure 2.24: Permeability and hysteresis curves for the ring samples of pure polycrystalline iron (cut in the tension plane after unloading) [76]. The data are presented with kind approval of S. Takahashi.

to disappear [8, 49]. The reasons should be in different residual stress distribution in case of the medium/high carbon steels with initially more distorted lattice [74] and/or in different dislocation mobility due to increase of different type of inclusions in the ferritic matrix. In addition, increase of the carbon content is known to lead to worsening of sensitivity of the magnetic methods to the mechanical deformation [8, 77] and to monotonically decaying dependence of the BN RMS [47, 48].

Another interesting feature of the considered magnetic behaviour, which seems to always accompany the hysteresis bulging, is near-the-same intersection hysteresis points for the deformed specimens (see insets in Figs. 2.4-2.6 and 2.24). Similar pictures of the intercrossed loops in the second and the fourth hysteresis quadrants were already shown in the classical Bozorth textbook [7], in the 30-years old Abuku's article [50], and in a row of recent works [8, 47, 51]. According to our knowledge the effect was firstly mentioned by Bulte and Langman [51] three years ago. For a chosen mild steel the stable cross-points, called the "coincident" points, were obtained in wide range of *applied plastic deformation* (from tension to compression including non-stressed state). Our current

investigation, however, showed that for our low-carbon steel the stable "coincident" points of the *unloaded* samples do not coincide with the hysteresis loop of the non-stressed samples (see insets in Figs. 2.4-2.6). This is also valid for the presented measurements of pure polycrystalline iron (see inset in Figs. 2.24). The position of the coincident points is also dependent on the field amplitude [51] as is shown in Fig. 2.8. These experimental facts suggest that the coincident point behaviour is of stress-driven nature and it possibly relates to the two phase magnetization process. Another argument for existence of physical background of the coincident points phenomenon is that theoretical hysteresis modeling of the deformed soft Fe-Si alloy does show the hysteresis bulging and the coincident points effects [78]. However, the nature of such a behavior is not clear up to now and further investigations are planned to clarify it.

2.4.2 Applicability of magnetic testing

The main aim of this work was more technical than physical: the search of the most sensitive and reliable magnetic descriptors of uniaxial tensile deformation. Such descriptors showing near-linear dependencies in $5 - 20\%$ strain range were picked up from the detailed minor loop datasets (see Figs. 2.13-2.14). The chosen descriptors are defined by the above-mentioned features of the magnetic behavior, namely by the permeability two-peak broadening and by the hysteresis loops "rotation" around the intersection points (see Fig. 2.6).

The most promising parameter showing a good sensitivity-stability ratio even at non-saturated field amplitudes was found to be the $B(H, H_m)$-MAT descriptor (see Fig. 2.14(a)). The conjugate $H(B, H_m)$-MAT descriptor does also show good sensitivity but poor stability. Stability of the descriptors is understood as a low variability of their magnitudes when their coordinates $(H/B, H_m)$ are shifted around. Since the permeability as a differential characteristic is a less stable magnetic parameter than the hysteresis, it should be used in practice very carefully [37]. The permeability maximum region is the most unstable to variations of

the measurement conditions (of the contact quality between the yoke and the sample as well as of the magnetization speed – dynamical effects are proportional to $\partial B/\partial t$). Therefore, it is better to utilize the proposed $\Delta H(\mu = const)$ parameter rather than the permeability half-height width $\Delta H(\mu = \mu_{max}/2)$.

Thus, the best solution for magnetic NDT of the investigated degradation of low-carbon steels seems to be the following. First, a pair of symmetrical hysteresis points in the third quadrant for the considered upper loop half $(-H', -B')$ and in the first quadrant for the mirror-image lower half (H', B'') of a near-saturation hysteresis loop should be chosen with the best sensitivity-stability ratio of the $B(H', H_{sat})$-MAT parameter (e.g. with the $H' = -2.6$ kA/m working point as in the case of the tested strips – see Fig. 2.14(a)). Using the two symmetrical points for the MAT parameter evaluation increases the method stability (two point averaging). Additionally the quality (i.e. symmetry) of the measured hysteresis loop can be checked on the requirement of $B' = B''$. For a complementary control, it is useful to utilize the measured near-saturation loop for evaluation of another MAT parameters, such as the $H(B, H_{sat})$ and the permeability curve width $\Delta H(\mu = const)$ (see Figs. 2.13(b) and 2.14(b)).

When either the tested material can not be magnetized to saturation or the testing time should be decreased, there is a need to use a minor hysteresis loop for the magnetic testing. In this magnetization range, only the $B(H, H_m)$-MAT parameter shows good sensitivity and stability (e.g. the $B(H = 1.9, H_m = 2.6)$ kA/m MAT-parameter can be used in the case of the tested strips – see Fig. 2.14(a)). For a complementary control, the classical coercive field H_c of the tested minor loop can be utilized.

Further improvement of the method stability can be achieved by evaluation of the MAT parameter values from repeated measurements of the same hysteresis loop. However, this leads to increase of the testing time. Another way of increase of stability of the proposed MAT-parameters can be to use integral descriptors of the hysteresis loop "rotation" around

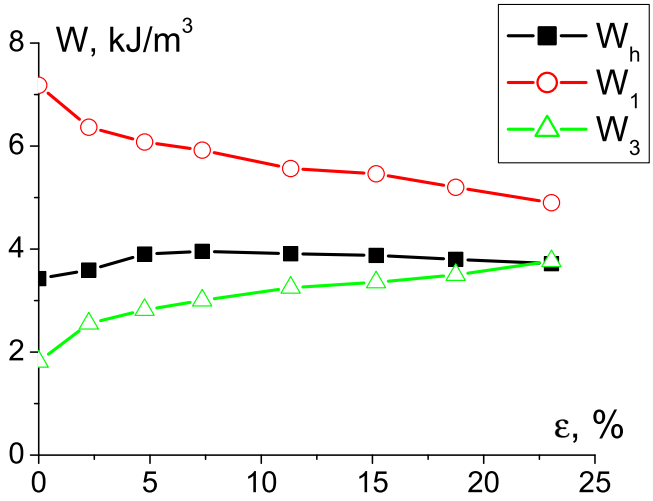

Figure 2.25: Integral descriptors of the hysteresis loop rotation W_1 and W_3 compared to the total hysteresis losses W_h for the strip series. Similar trends were found for the window-shaped series.

the coincident points. In Fig. 2.25 such integral parameters for the strips in the first $W_1 = \int_0^{H_{sat}} B\mathrm{d}H$ and the third $W_3 = \int_{-B_{sat}}^{0} H\mathrm{d}B$ hysteresis quadrants for the upper saturation hysteresis branch together with the classical total hysteresis losses $W_h = \oint_{-B_{sat}}^{B_{sat}} H\mathrm{d}B$ are shown.

Two parallel series of the samples, magnetized in the tension direction after unloading, were investigated in detail (minor loops) for comparison of the measurements of the magnetically closed samples (windows) with the single-yoke laboratory equipment (strips). The purpose was to test the simple method of measurement with the small single yoke for the whole set of magnetic parameters [28, 37]. It can be stated that these two types of measurement showed qualitatively similar results including the two-peak permeability profile, the hysteresis loop intersection points, and the behavior of the classical as well as the MAT magnetic parameters. However, there are some serious quantitative distinctions, namely the less pronounced first permeability peak for the window series and the considerable differences of the measured magnetic quantities on field/permeability scales for these two sample series (see for example Figs. 2.7 and 2.14(b)).

The first point to keep in mind is that even the window-shaped samples are not magnetically uniform circuits. The flux is closed through two magnetically different parts, because only the window legs are deformed, whereas the upper and the bottom parts of the "window" are in the initial non-deformed state (see Fig. 2.1). This leads to the less pronounced first permeability peak and also to some mistakes in the inside-sample field definition (because of non-homogeneous flux distribution and demagnetizing fields on the interfaces between the structurally different volumes). Another reason of the different field/permeability scales is the hysteresis broadening due to dynamical effects. The magnetization speed for the yoke measurements was chosen higher than that for the windows, which resulted in enlarging of the field scale and, additionally, in reducing of the permeability scale for the strip series. Quantitative distinctions of the sensitivity maps for the two series (Figs. 2.10-2.11) could be also caused by non-homogeneous strips magnetization at low field amplitudes.

However, the main reasons of the differences between measurements of the closed and the open sample series are the intrinsic imperfections of the yoke measurements, namely *(i)* mistakes of the sample field determination with the magnetizing current method, and *(ii)* uncontrolled influence of the contact quality between the yoke legs and the samples on the measurement results. The uncertainty of the sample-yoke contact, which was fixed as much as possible by the sample surface polishing and the yoke weighting, is probably the most problematic point for development of the single yoke measurement method from a laboratory equipment to a standard industrial NDT technique. This known topical problem stimulated us to a detailed analysis of the single-yoke setup with the aim of its optimization to a stable and easy measuring technique for the magnetically open samples. Results of this investigation are presented in the next Chapter 3.

This work showed significant anisotropy of magnetic behavior in different directions with respect to the uniaxial tensile deformation. Despite the similar dependence of the classical magnetic parameters in the

both directions, their sensitivity to the strain in transversal direction is smaller than along the stress (see Figs. 2.7 or [75]). Evidently, the magnetic techniques can be used for NDT of uniaxially deformed ferromagnetic materials, especially for the case of low-carbon steels, but the attention should be paid to determination of the stress direction. Magnetically and mechanically harder steels are supposed to be more difficult problem for magnetic NDT in comparison with the presented case of the low-carbon steel. For the harder steels the first permeability peak disappears [8], and the traditional magnetic parameters show worse sensitivity to the strain [8, 77]. Another limitation for the proposed MAT-solution is that, evidently, for the harder steels the hysteresis intersection points get smeared with suppression of the hysteresis "rotation" behavior [7, 8].

So the investigated case of material degradation should be generally tested by a rotational magnetic measurement technique to clarify the direction/s of uniaxial deformation [67, 79]. Different magnetization directions with respect to the stress require different magnetic parameters for an optimal NDT: in the axial direction the $B(H, H_m)$, the $H(B, H_m)$ and the $\Delta H(\mu = const)$ MAT parameters were proposed to be utilized for the low-carbon steels (see Figs. 2.13-2.14); in the transversal direction the $\mu(H, H_m)$ MAT parameter seems to be the most promising [45]. For additional control it would be useful to test the coercive field H_c, which shows moderate rise with the strain, but which is the parameter with minimal dependence on the quality of the yoke-sample contact [28, 37].

2.5 Conclusions

Inductive hysteresis and Barkhausen noise measurements were performed to investigate the influence of plastic tensile deformation of the low-carbon steel in the parallel as well as in the perpendicular directions to the stress. The behaviour of the classic hysteresis parameters and of the root mean square values of Barkhausen noise was explained by the change of the dislocation structure of the material with the deformation, which was confirmed by observation with transmission electron

microscope. Physically interesting feature of the two-peak form of the permeability and of the Barkhausen noise envelope was ascribed to the internal residual stresses. Poorly investigated topic of anisotropy of magnetization process with respect to the uniaxial stress direction was considered in detail. Another intriguing effect of the hysteresis coincident points was observed and pointed. Additionally, the general question of influence of the steel composition on the observed magnetic behavior was mentioned.

The minor loop measurements, done on the two series of magnetically closed and open samples, showed qualitatively the same results in all range of magnetization. On the basis of the characteristic magnetic features of the considered problem (the two-peak permeability and the hysteresis coincident points) the new magnetic parameters, namely the $B(H, H_m)$, the $H(B, H_m)$ and the $\Delta H(\mu = const)$ MAT parameters, with good sensitivity-stability ratio in wide range of the strain were proposed for utilization. Related problems of a general 2-D testing as well as of worsening of the magnetic parameters sensitivity in transversal directions and with the harder steels were discussed.

Chapter 3

Optimization of single-yoke testing

Our results of the single-yoke measurements with the method of the sample field determination from the magnetizing current and their comparison with measurements on the parallel series of magnetically closed samples, presented in Chapter 2, showed remarkable instability of the measurement technique. Moreover, the quantitative differences between results on the closed and on the open samples were significant (see Section 2.4.2). This stimulated us to instrument our measuring equipment for the magnetically open samples by a surface field measurement (see Section 1.1). However, the first attempts of such measurements with relatively small heads showed considerable dependence of the measured surface field on small deviations of the Hall sensor position. That forced us to make serious research of technical side of the problem with the aim to clarify applicability conditions and limitations of the technique. Firstly, detailed investigation of distributions of around-sample fields at constant values of the magnetizing current, i.e. Direct Current (DC) measurements, was done. This part of the work is presented in Section 3.1 and published in Ref. [80]. The obtained results showed how the single-yoke setup should be designed for further experiments. So, finally, AC surface field measurements were realized in order to prove our ideas about the ways of the setup optimization. These results are given in Section 3.2 and published in Ref. [81].

3.1 DC measurements

This section is devoted to the preliminary DC investigation of the surface field distributions around the sample surfaces. The work is done on basis of experimental data (measurements of the samples fields by a conventional Hall probe), accompanied by computational modeling by Finite Element Method (FEM). It is structured as follows: Section 3.1.1 describes and analyzes the head-sample contact problem; Section 3.1.2 is dedicated to the FEM computation of the problem and its comparison with fields, measured in the free space around the samples. Discussion, needed for the next AC experiment design, can be found in Section 3.1.3.

3.1.1 Analysis of the problem

Fig. 3.1 represents a sketch of the considered head-sample system with two widely-used configurations of the driving coil/s. In the first configuration two identical Driving Coils are wound symmetrically around the two Legs of the yoke (DCL configuration) [28, 35, 36]. In the other configuration a single Driving Coil is wound (also as symmetrical as possible) around the yoke Bow (DCB configuration) [32]. The inspection head with cross-section S_h, magnetic path l_h, made from a ferromagnetic material with permeability μ_h, is closely attached to a flat ferromagnetic sample with cross-section S_s, magnetic path l_s, and permeability μ_s. The magnetic contact is never ideal, characterized by an air gap with cross-section $S_a = S_h$, magnetic path l_a, and $\mu_a = 1$. Total number of the driving coil turns is N carrying the magnetizing current I. Main features of the magnetic circuit can be considered on the base of Ampere's law. With the assumption of zero magnetic flux leakage (i.e. $\Phi = \Phi_s = \Phi_h$) it states the total magnetomotive force equals the sum of its drops on constituents of the circuit (see e.g. [38]):

$$NI = \frac{\Phi}{\mu_0}\left(\frac{l_s}{\mu_s S_s} + \frac{l_h}{\mu_h S_h} + \frac{l_a}{S_a}\right) \tag{3.1}$$

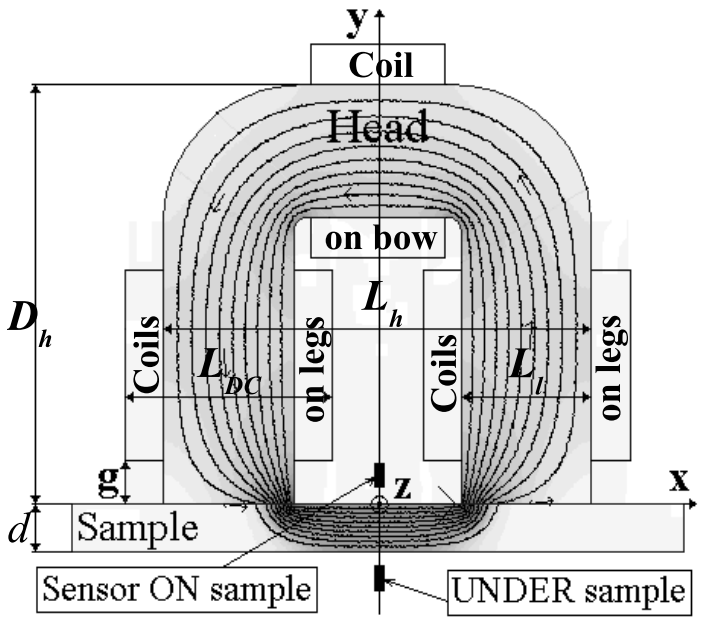

Figure 3.1: Sketch of the head-sample system.

We introduce an *effective* sample field $H_s^* = NI/l_s$, which is the field, calculated classically from the magnetizing/driving current (i.e. the field in the sample in the ideal case when reluctances of the head and the air gap are both zero) [38]. For the sake of simplicity, hereafter within this chapter, all magnetic parameters, marked by the upper star, mean the correspondent magnetic parameters, calculated with reference to the magnetizing current. Thus Eq. 3.1 can be rewritten as

$$H_s^* = H_s \left[1 + \frac{\mu_s S_s}{l_s S_h} \left(\frac{l_h}{\mu_h} + l_a \right) \right] \tag{3.2}$$

where $H_s = \Phi/\mu_0 \mu_s S_s$ is the *real* value of the inside-sample field. As the parenthesis in Eq. 3.2 is never negative, the real sample field is always smaller than the effective one $H_s < H_s^*$. With reference to the magnetizing current this discrepancy between the effective and the real fields should be minimized. For that it is recommended to approach the square bracket to one by use of a very soft magnetic yoke $\mu_h \gg \mu_s$ with a large cross-section of magnetic poles $S_h \gg S_s$. From Eq. 3.2 it

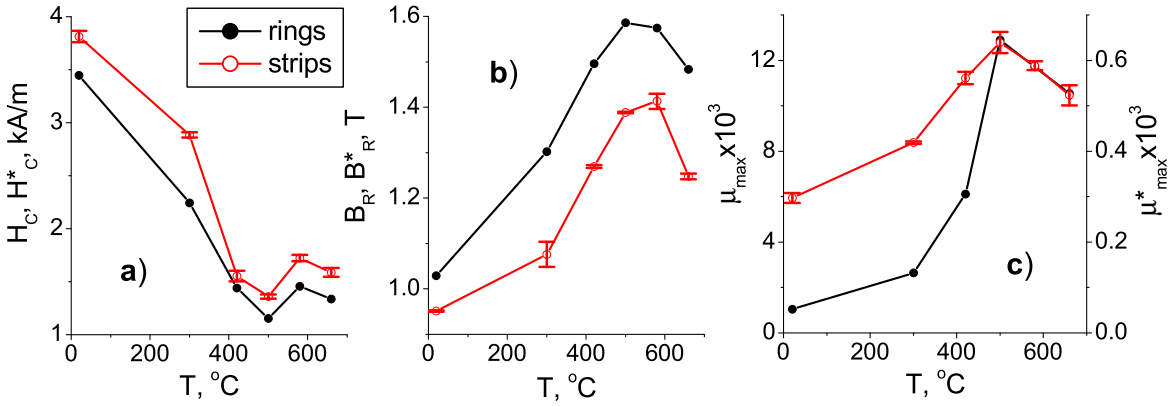

Figure 3.2: Coercive field H_c (a), remanent induction B_R (b), and maximum differential permeability μ_{max} (c), measured on rings, together with H_c^*, B_R^*, and μ_{max}^*, measured on strips by Head 1, versus tempering temperature T (T=20°C corresponds to the quenched sample).

is also evident that even a small air-gap l_a could lead to a substantial discrepancy between H_s^* and H_s, especially in the case of magnetically soft specimens $\mu_s \gg 1$ [12, 38].

Figs. 3.2 represent a typical example of the measurement results: the traditional saturated magnetic parameters, measured on closed rings (with constant magnetization speed $\mathrm{d}H_s/\mathrm{d}t = 1$ kA/m/s), which are compared with the corresponding *effective* parameters, referred to H_s^*, obtained by single inspection head measurements on flat strips (with the size 120 $mm \times 20\ mm \times 3\ mm$; measured with $\mathrm{d}H_s^*/\mathrm{d}t = 14$ kA/m/s). The measurements were performed on a model series of construction steel CSN 14260 (EN 54SiCr6), structurally varied by thermal processing (quenching from 840°C down to 20°C in oil, and following tempering for 30 minutes at temperatures from 300°C up to 660°C) [46]. Head 1 was used for these measurements (see geometrical parameters of Head 1 in Tab. 2.1 and its magnetic properties in Fig. 3.3). Each flat specimen was measured six times with differently positioned head for investigation of the data scatter. It can be seen from Fig. 3.2 that behavior of the effective parameters, measured on the open samples, and of the real parameters, measured on the rings, do again correspond to each other

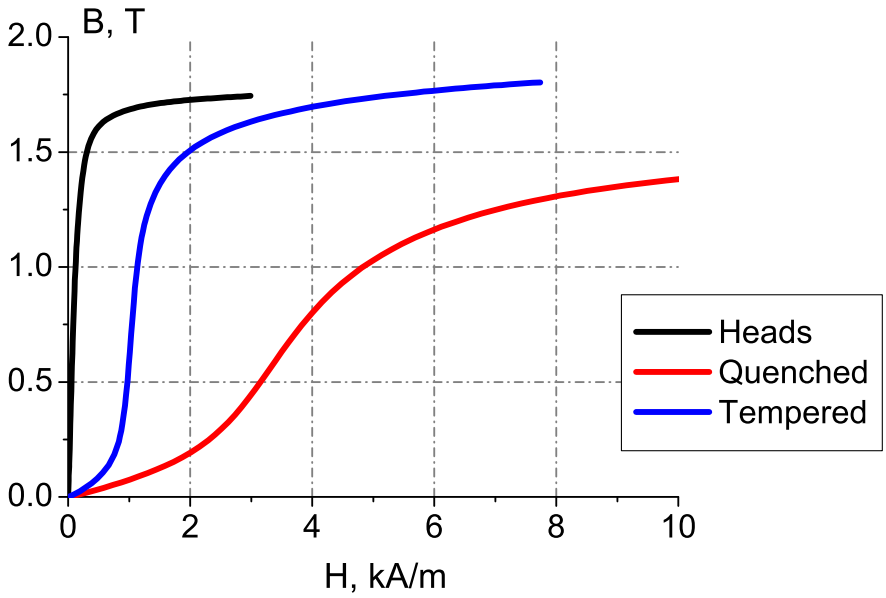

Figure 3.3: Virgin curves of the used materials: Heads, Quenched and Tempered samples.

qualitatively. As expected from Eq. 3.2, the real magnetic field in the samples is smaller than the effective one due to a non-zero reluctance of the head and of the air-gap (see Fig. 3.2(a) for H_c), and the real magnetic induction is higher than the effective one due to the non-zero flux leakage and the demagnetizing field in the non-uniform head-sample system (see Fig. 3.2(b) for B_R). The coercive field H_c proves to be again the most stable magnetic parameter with respect to imperfections of the head-sample contact [28, 37]. The other magnetic parameters show larger scatter and require more precise head-sample contact conditions.

The simple problem analysis, stated in this section, together with the typical measurement results (of Chapter 2 and in Figs. 3.2) prove that relative indication of the material structure variation by single-yoke testing should be more applicable under the condition of truly sample field measurement $H_s(t)$, determined simultaneously with the induced voltage $U_{ind}(t)$.

3.1.2 Investigation of surface sample fields

In order to explain the experimental results, to investigate possibility of measurement of the inside-sample magnetic field, and to predict the magnetic output with changing conditions of the measurement, the head-sample circuit was simulated by a 2-D FEM computation (using the FEMM program [82]). The task was solved as a steady-state problem for definite driving current values. The program found fields satisfying Maxwell equations via magnetic vector potential $\mathbf{A}$, which for 2-D problems has the z-component only [14]:

$$\nabla \times \left(\frac{1}{\mu(B)} \nabla \times \mathbf{A} \right) = \mu_0 \mathbf{I} \tag{3.3}$$

where flux density $\mathbf{B}$ is written in terms of the vector potential as $\mathbf{B} = \nabla \times \mathbf{A}$. The boundary conditions were also defined through the magnetic potential $\mathbf{A}$, which generally do not obey classical conditions of continuity of the normal component of magnetic induction and the tangential component of magnetic field. Dirichlet boundary condition, i.e. $A = 0$, was defined along the outer boundary in order to keep the magnetic flux inside the considered region. The simplest Neumann boundary condition, specifying the normal derivative of potential along the boundary to be zero, was used along all inner boundaries to force the flux to pass each boundary at exactly right-angle to it. This sort of boundary condition is consistent with an interface with a very highly permeable metal, what does not fully obey our case and may be a source of error. The finite element mesh was triangular with the size chosen to be $0.05 \div 0.7$ mm. Mesh of the whole problem usually contained about one-two hundred thousands of nodes.

In Fig. 3.3 the virgin curves of the used laminated Fe-Si yokes (see Tab. 2.1) and the two used specimens are presented. For investigation the magnetically hardest (quenched) and the softest (tempered at $T = 500°C$) specimens of the thermally treated series of the construction steel CSN 14260 (EN 54SiCr6) [46] were chosen (shown in Fig. 3.2). They will be referred to hereafter as the *Quenched* and the *Tempered*

samples, respectively. As a result of the calculations, 2-D maps of the magnetic field and of the flux density were obtained as functions of the magnetizing current for the anhysteretic magnetization process along the virgin curves. A sketch of the problem with the flux distribution map is shown in Fig. 3.1.

Results of the FEM calculations for four different qualities of the head-sample contact are presented in Fig. 3.4. The contact imperfections were modeled either by a surface defect (an ellipsoidal "crack" 6 mm long and 0.7 mm deep, positioned under one of the head legs), or by a 0.25 mm air-gap, or by the defect and the gap together. Head 1 with DCL and a 3 mm thick Tempered sample were used for these simulations. Computations with defects and air-gaps smaller or larger than the presented dimensions show qualitatively similar behavior. Tangential (horizontal x-components in Fig. 3.1) magnetic fields, computed in the middle of the sample (inside-sample field H_s), at 2 mm distance above the sample along the symmetry y-axis (on-sample field H_{on}) and below the sample (under-sample field H_{un}), are plotted versus the effective field H_s^* in Figs. 3.4(a-b). Fig. 3.4(c) gives calculated values of the magnetic flux in the sample Φ_s (along the y-axis) and in the head Φ_h (along the y-axis in the bow as well as in the head legs at 1.5 mm distance from the legs front) again in dependence on H_s^*. Fig. 3.4(d) presents the computed distributions of x-component of the magnetic fields along the y-axis for the considered contact conditions.

Measurements of the surface tangential magnetic fields above and under the samples were done with the F.W.Bell Gaussmeter, Model 7030, and the standard transverse Hall-probe STF71-0404-05-T with temperature compensation. The minimal distance of the Hall sensitive element to the sample surface was 2 mm; the declared accuracy was ± 65 A/m within the used measurement range of 24 kA/m. Inspection Head 2 with larger dimensions (in order to have enough free space between the head legs for the field measurements) and with DCL as well as DCB configurations (see Tab. 2.1 and Fig. 3.3) was applied to polished surfaces of the Quenched and the Tempered samples with dimensions $50 \times 60 \times 3$ mm^3.

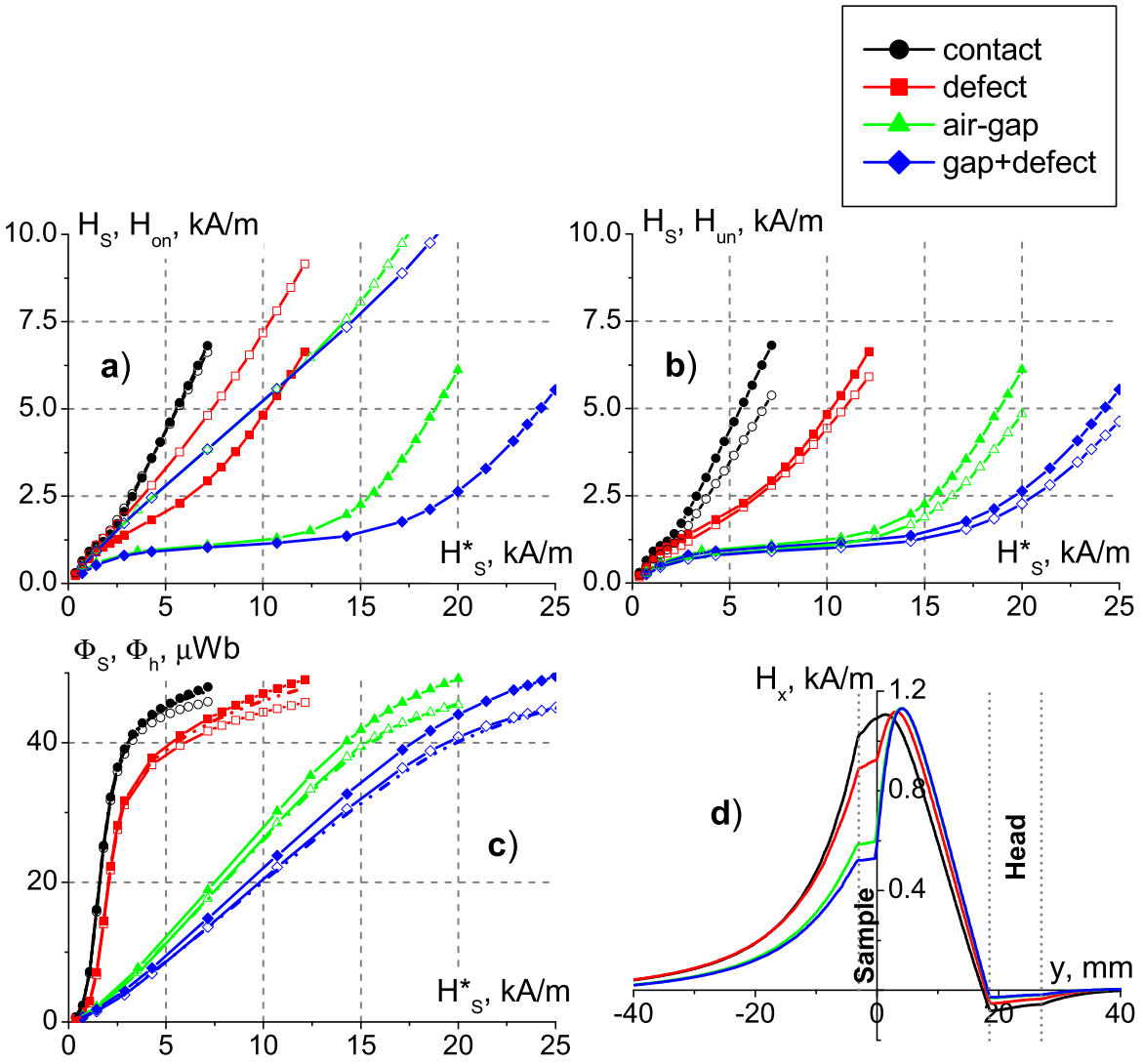

Figure 3.4: FEM simulation of influence of contact imperfections on the single-yoke measurements: (a) H_s and H_{on}; (b) H_s and H_{un}; (c) Φ_s and Φ_h, plotted versus H_s^*. The full symbols represent the points of H_s (a-b) and Φ_s (c) for the different contact conditions, marked by different symbols and colors (see inset). The corresponding open symbols, marked by the same color, represent the points of H_{on} (a), H_{un} (b) and Φ_h in the head bow (c) for the same contact conditions. The dash-dot lines in (c) presents Φ_h close to the head leg front. Computed points are connected by lines for eye guidance. Figure (d) represents computed x-component of the field gradients along the y-axis for the considered contact conditions, marked by the same colors.

The sample magnetic path for this yoke was defined as the mean distance between the head legs $l_s = 29$ mm, which gave good correlation with the experiment. The head was carefully positioned in the middle of the samples; the air-gaps were introduced by non-magnetic plates to modulate the contact imperfections. The tangential x-component of the magnetic field in the head-sample system was measured along the symmetry y-axis with a half-millimeter step at several constant values of the effective field $H_s^* = 1.7; 3.5; 5.2; 6.9$ kA/m by the Hall-probe, fixed in a specially designed movable control holder. All field measurements were accompanied by the FEM computations with the corresponding configurations.

Results of the investigation are presented in Figs. 3.5-3.6. Figs. 3.5 show the measured and the computed curves for the two considered samples and for two H_s^* values at condition of the *perfect* contact with the head for the DCL (Fig. 3.5(a)) and the DCB (Fig. 3.5(b)) configurations. Figs. 3.6 show comparison of the *different contact* conditions, namely the perfect contact and the 0.2 mm air-gap between the legs of the Head 2 and surface of the Tempered sample, again for the two types of the driving winding. For the sake of clarity the graphs contain minimum curves: dependencies for other effective field values are qualitatively the same; field values for the Quenched sample are very close to the presented curves for the Tempered sample. Increase/decrease of the air-gap causes deterioration/improvement of the sample magnetization with similar behavior of the around-sample fields. Extrapolation of the experimental on-sample H_{on} and under-sample H_{un} field distributions indicates the most probable values of the inside-sample field H_s. Small deviations of the extrapolated sample fields for the different magnetizing coil configurations are evidently caused by slightly different conditions of additional leakage flux losses through the head legs.

In order to show how the magnetization conditions are varied by modifications of the sample/head dimensions, FEM computations were applied for the system in the case of perfect magnetic contact. Modifications of width of Head 2 and of the driving coil dimensions are presented

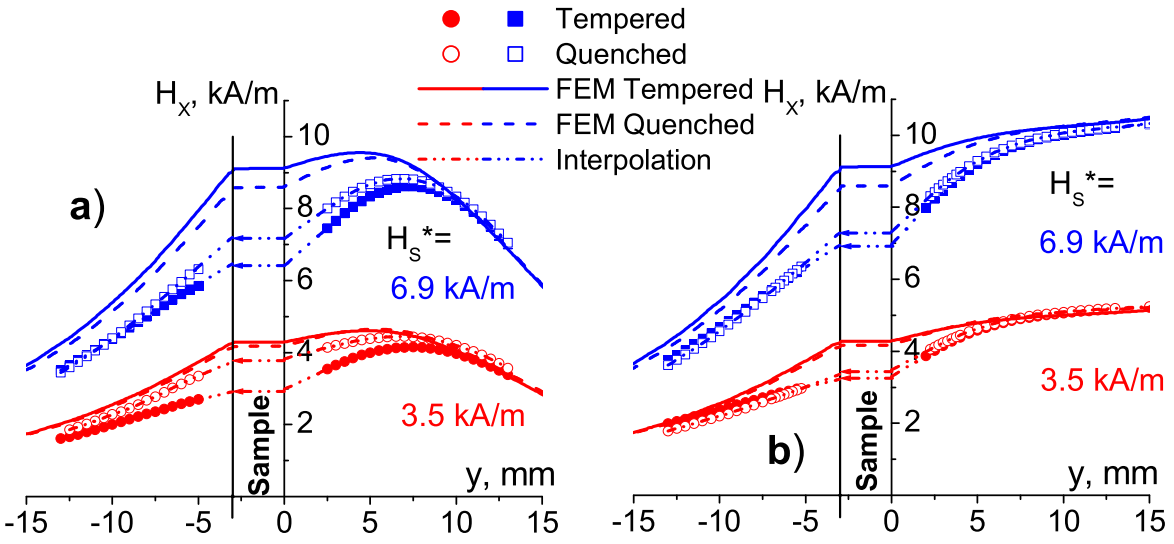

Figure 3.5: Experimental and FEM computed tangential fields along the y-axis for the *perfect* contact case for DCL (a) and DCB (b) configurations. Extrapolation of the experimental field curves above and under the sample (dash-dot lines) indicates the values of H_s. Values of the applied H_s^* are indicated in the figures. Similar trends were found for another H_s^* values.

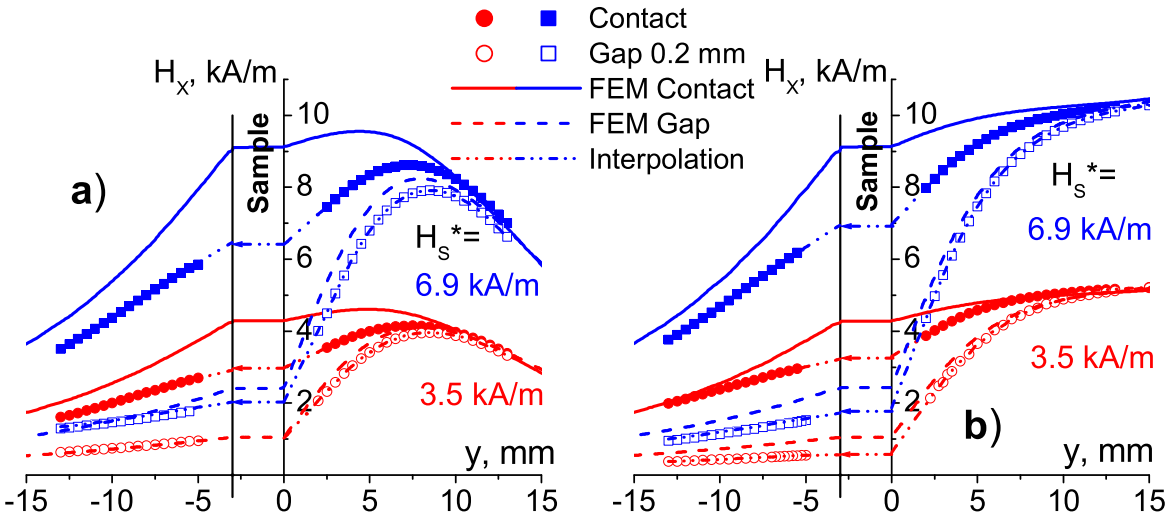

Figure 3.6: Experimental and FEM computed tangential fields along the y-axis for the *different contact* conditions: the perfect contact (full symbols) and the 0.2 mm air-gap (correspondent open symbols) between the sample and the head for DCL (a) and DCB (b) configurations. Dependencies are shown for the Tempered sample only. Similar trends were found for the Quenched sample and for another H_s^* values.

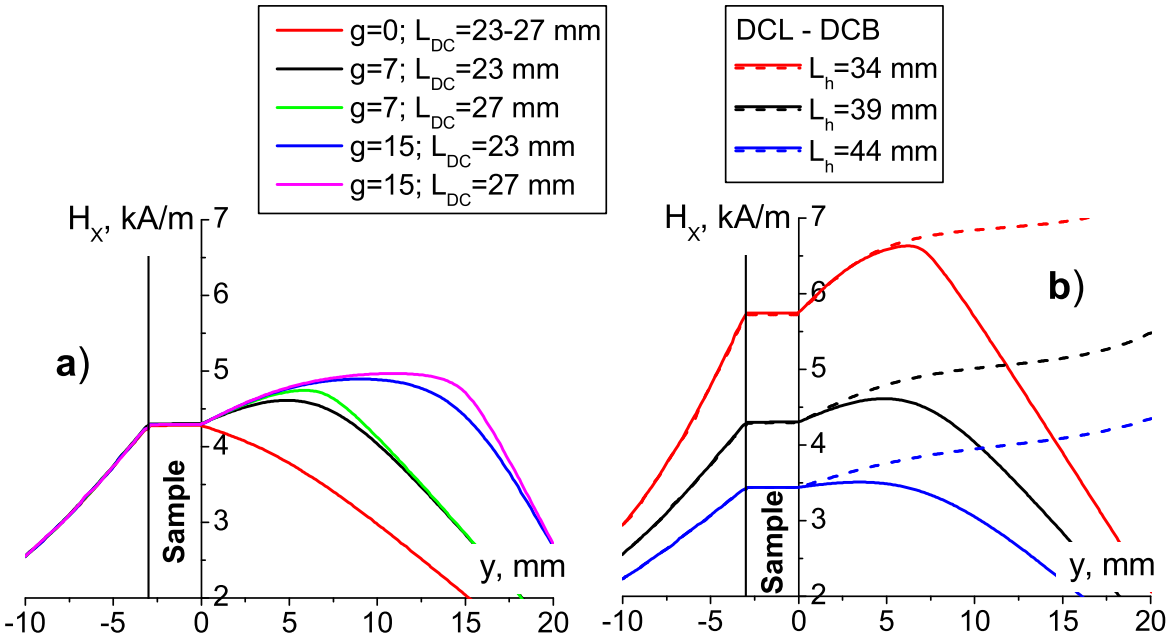

Figure 3.7: Tangential field distributions along the y-axis at $H_s^* = 3.5$ kA/m: (a) Constant Head 2 dimensions, varied DCL dimensions g and L_{DC} (Head 2 configuration $g = 7$ mm, $L_{DC} = 23$ mm is shown by black line); (b) Constant dimensions of DCL (solid lines) and DCB (dash lines), varied Head 2 width L_h (Head 2 configuration $L_h = 39$ is shown by black lines).

in Figs. 3.7 (3 mm thick Tempered sample is used). Fig. 3.7(a) shows the tangential field distributions along the y-axis for different DCL dimensions. Fig. 3.7(b) illustrates the influence of different head widths for the two types of the driving winding. Dependencies of the sample fields on the sample thickness d are presented in Figs. 3.8 (Head 1 and the Tempered sample are used). The figure indicates increase of non-uniformity of the magnetic field penetration inside the sample with increase of its thickness. Other modifications of the set-up dimensions do not give significant alterations of the magnetizing conditions.

3.1.3 Discussion

In this section the main source of problems of the single-yoke measurements is considered, namely dependence of the magnetic output of the

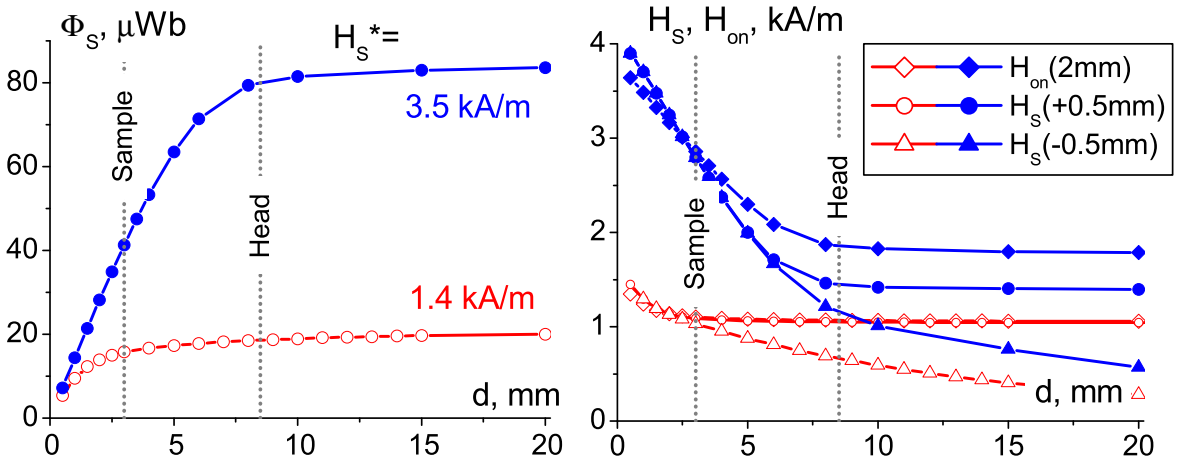

Figure 3.8: Dependencies of inside-sample flux (a) and inside-/on-sample fields (b) on the sample thickness d for two effective field values $H_s^* = 1.4$ and 3.5 kA/m. H_s at the 0.5 mm distance from the top surface (+0.5 mm) and at the 0.5 mm distance from the bottom surface (−0.5 mm) are shown. Thicknesses 3 mm of the sample and 8.5 mm of Head 1 legs are indicated.

setup on generally unknown and non-reproducible quality of contact between the sample and the head leading to appearance of parasitic air-gaps in the "quasi-closed" magnetic circuit. It is seen from Figs. 3.4 and 3.6 that with worsening of the contact it becomes more difficult to magnetize the sample: all dependencies of the sample fields and flux are stretched to higher values of the effective fields H_s^* with increase of the on-sample field gradient. This leads to significant rise of the difference between the on-sample H_{on} and the inside-sample H_s fields. The under-sample field H_{un} is always smaller than H_s with slowly decaying field distribution (see Figs. 3.4-3.6). The magnetic flux inside the sample Φ_s, as is shown in Fig. 3.4(c), is smaller than the flux inside the head Φ_h due to non-zero flux leakage between the yoke legs. This is the reason why the head flux values *near the sample* are closer to the inside-sample flux. Therefore it is recommended to place the induction coil on the *leg-ends* of the head [12, 32]. The computed flux behavior corresponds to the well known experimental observation that presence of the air-gaps shifts the induction signal maximum to higher H_s^*, decreases its value,

and eventually changes its shape completely from a peak-contour to a peak-less rectangular profile.

While curves in Figs. 3.4 were only numerically computed, Figs. 3.5-3.6 present comparison of the computation with the experiment. The FEM calculated curves in the case of *perfect contact* (see Figs. 3.5) correspond to the experimental ones only qualitatively. The comparison is in a substantially better agreement with the air-gap between the head and the sample (Figs. 3.6). The main reasons of the poorer agreement of the experiment and the calculations are assumed to be the following: *(i)* discrepancy between the real experimental 3-D situation and our 2-D FEM simulations (different z-dimensions of the head and the samples); *(ii)* calculation error due to the used Neumann boundary condition on the head-sample interfaces, which much better suits to interface between soft magnet and air [82]; *(iii)* in practice there are always some air-gaps between two adjacent surfaces.

The experimental and theoretical investigation of the on-sample field distribution of the single-yoke setup proves existence of substantial gradients of the x-component of the sample surface tangential field. Moreover, for the DCL case this distribution can have a non-monotonous parabolic-like profile. However, values of H_{on} and its gradient in vicinity of the sample surface are very similar both for DCL and DCB configurations (see Fig. 3.7(b)). This tangential on-sample field is technically measurable at a *non-zero distance* from the sample surface (without expensive and less-stable technical tricks these distances are of millimeter order). Therefore, significant error can be introduced by a "blind" measurement of the sample field with a probe positioned simply "as close as possible" to the sample surface [32, 37] with unknown and unrepeatable contact quality in particular. A promising way towards solution of the contact problem can lead via multi-point measurement of the sample-surface tangential magnetic fields and their extrapolation to the sample surface. This simple idea was already utilized in laboratories for DC SST-like measurements with lifting H-coil more than seventy years ago [7]. Twenty years ago it was revived by T. Nakata et al. [83] and

recommended for SST improvement by introducing of two H-coils in its design. Up to now the Nakata's proposition has not been realized in full extent and has not been included into the SST standard [18], however, it has a number of followers [84, 85].

In order to determine the on-sample field profile with the DCB configuration, minimum *two field sensors*, located in proper positions at the symmetry y-axis in the initial linear-like field gradient region, are needed. The DCL set-up version is more problematic for the suggested multi-point field extrapolation because of the non-monotonous on-sample field behavior. However, as it was shown by the simulations and the experiment, the position of the field distribution maximum is defined by combination of the leakage fields from the head legs and from the coils edges. With large enough coils width L_{DC} and gap g between the coils edges and the sample (see Fig. 3.7(a)) the peak position roughly corresponds to the gap distance g (as in the case of Head 2 with $g = 7$ mm in Figs. 3.5(a)-3.6(a)). Therefore, in case when DCB configuration can not be used, convenient design of the DCL set-up (carefully chosen head/coils dimensions) should be done to shift the peak maximum of the field distribution far enough from the sample surface for two-point extrapolation, otherwise a minimum three-sensor array should be applied to describe the parabolic-like field profile. The field gradient, measured by the sensors, can give additional information about the head-sample contact quality (see Figs. 3.6).

The excellent quantitative coincidence between values of the inside-sample field, obtained by extrapolation of the field distributions above and under the sample, proves correctness of the proposed extrapolation method for the sample field determination. Extrapolation of the tangential field profile under the sample can be very helpful for precise determination of the real H_s values. The field under the sample H_{un} is not influenced by the stray fields of the head, its distribution is smooth and simple, and two field sensors can be quite enough for good accuracy. Simultaneous extrapolation of H_{on} and H_{un} fields should be able to determine the H_s values precisely (see Figs. 3.5). In order to real-

ize this, however, the bottom side of the sample must be accessible and the sample must be thin enough to be magnetized homogeneously (see Figs. 3.8).

The optimum head dimensions depend on many factors: the investigated material, its shape, the surface quality and the sample dimensions (its cross-section S_s in particular), the desired gradients of the measured surface field distributions as well as the tested locality requirements. In order to magnetize an iron-based sample through, the cross-section of the iron-based head should be larger than that of the sample $S_h \geq S_s$. Increase of S_h, with the legs front best fitted to the sample surface, does also improve the result stability to the sample surface roughness [28]. On the other hand, in the case of very thin samples $S_s \ll S_h$ the influence of small thickness deviations to the measurement results can be considerable, as it can be seen from FEM calculations (see Figs. 3.8) and as it is known experimentally [30]. That is the reason of simultaneous on-line measurement of the sample thickness at magnetic NDT of thin steel sheets (see review [16]). Obviously, in real 3-D situation the way of the flux penetration into the sample is more complex than the theoretically investigated 2-D case. The flux penetrates not only into the sample depth but also into the sample breadth direction (z-direction in Fig. 3.1) gradually damping away from the head [86]. Therefore, measurement errors due to deviations of sizes and shapes of investigated samples should be counted with.

3.2 AC measurements

This section is devoted to the next step of the investigation of extrapolation method applicability, namely, to the AC measurements of hysteresis major loops together with the surface sample fields. The results of the preliminary DC measurements (see Section 3.1) were used for appropriate setup design. The section is structured as follows: in Section 3.2.1 the description of the experiment is given, the obtained results are presented in Section 3.2.2 and discussed in Section 3.2.3. Main conclusions

of Chapter 3 of this thesis are summarized in Section 3.3.

3.2.1 Experiment

Major hysteresis loops were measured on our home-made permeameter with triangular wave-form of the driving current (see Section 2.1.1). The Head 2 (see Tab. 2.1) in the DCB configuration together with the Quenched and the Tempered samples, used in our preliminary DC experiments (see Section 3.1), were used in the current work for the AC measurements. The sketch and the dimensions of the head-sample system are shown in Fig. 3.9. Major hysteresis loops of the yoke material and of the sample materials, measured on the ring-shaped specimens, are presented in Fig. 3.10 (the corresponding virgin curves are shown in Fig. 3.3). The soft magnetic material of the yoke with the leg cross-section larger that the sample cross-sections was chosen to magnetize the samples through. The DCB configuration was chosen in order to achieve monotonous field dependence above the sample. Two induction coils were wound around the head legs as close as possible to the sample in order to minimize the flux determination error (see Section 3.1.3).

Measurements of the surface tangential magnetic fields above and under the samples were done with the same F.W.Bell Gaussmeter and the same Hall-probe as for the preliminary DC experiment (Section 3.1). Air-gaps of 0.04 and 0.2 mm were introduced by non-magnetic plates to modulate the contact imperfections. All measurement conditions on the driving current were identically fixed for each sample. The harder Quenched sample was measured with the effective field amplitude $H_m^* \simeq 17$ kA/m and the constant effective speed $\mathrm{d}H_s^*/\mathrm{d}t \simeq 3.3$ kA/m/s. The softer Tempered sample was measured with the effective field amplitude $H_m^* \simeq 11$ kA/m and the minimal possible speed $\mathrm{d}H_s^*/\mathrm{d}t \simeq 1.3$ kA/m/s. Four identical separate measurements of the tangential x-component of the surface magnetic fields above and under the samples along the symmetry y-axis with a half-millimeter step (i.e. $\pm y = 2; 2.5; 3$ and 3.5 mm) were done. Digital averaging on-the-fly (from the measur-

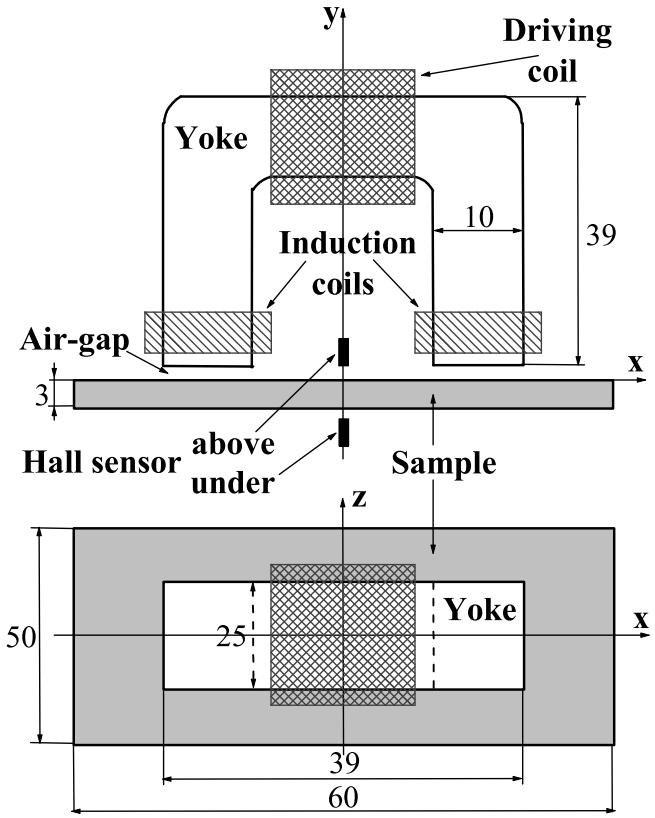

Figure 3.9: Sketch of the yoke-sample system.

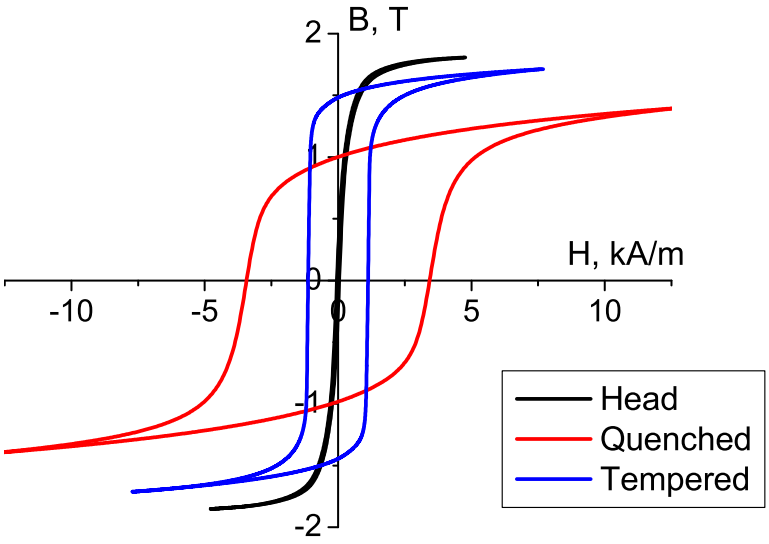

Figure 3.10: Major hysteresis loops of the head and the used samples.

ing 60 kHz sampling frequency to the resulting 50 Hz) was used for smoothing of the induction and the Hall signals [87].

These four identical measurements with differently positioned Hall sensor above and under the samples for each contact quality condition were used for extrapolation of the above/under sample field profiles down/up to the samples surfaces. The separate measurements were combined through the effective field H_s^*, and the resulting multi-point Hall measurements, obtained in such a way, were extrapolated linearly using the least-squares fitting. Eq. 2.2 was slightly rewritten in order to obtain relation between the material differential permeability μ_{dif}, as the material characteristic, the measurable induction signal U_{ind} (also referred to H_s^*) and the sample field derivative $\mathrm{d}H_s/\mathrm{d}t$:

$$U_{ind} = -n\frac{\mathrm{d}\Phi_h}{\mathrm{d}t} \simeq -nS_s\frac{\mathrm{d}B_s}{\mathrm{d}t} = -nS_s\frac{\mathrm{d}H_s}{\mathrm{d}t}\mu_0\mu_{dif} \tag{3.4}$$

For determination of the $\mathrm{d}H_s/\mathrm{d}t$ value, the derivatives of the effective field H_s^*, of the fields, measured by the Hall sensor H_{hall} at the minimal 2 mm distance, as well as of the extrapolated fields H_{ext} were calculated and substituted. Despite the digital averaging, the dependencies of the measured field derivatives $\mathrm{d}H_{hall}/\mathrm{d}t$ are noisy; the dependencies of $\mathrm{d}H_{ext}/\mathrm{d}t$ are even noisier. For the smoothing the local least-squares fitting by second-order polynomials with constant span was used.

3.2.2 Results

Results of the work for one half of the permeability/hysteresis loops, measured with the three different conditions of the head-sample contact, are presented in Figs. 3.11-3.21. Dependencies of the measured fields H_{hall} above (noted by "+" sign) and under ("-" sign) the two samples at the minimal and the maximal considered distances from the sample surfaces together with the sample field H_{ext}(+0 mm), extrapolated from the above-sample profile, are shown versus the effective field H_s^* in Figs. 3.11-3.12. The zoomed insets illustrate the low field region in detail. Figs. 3.13-3.14 present comparisons of the effective,

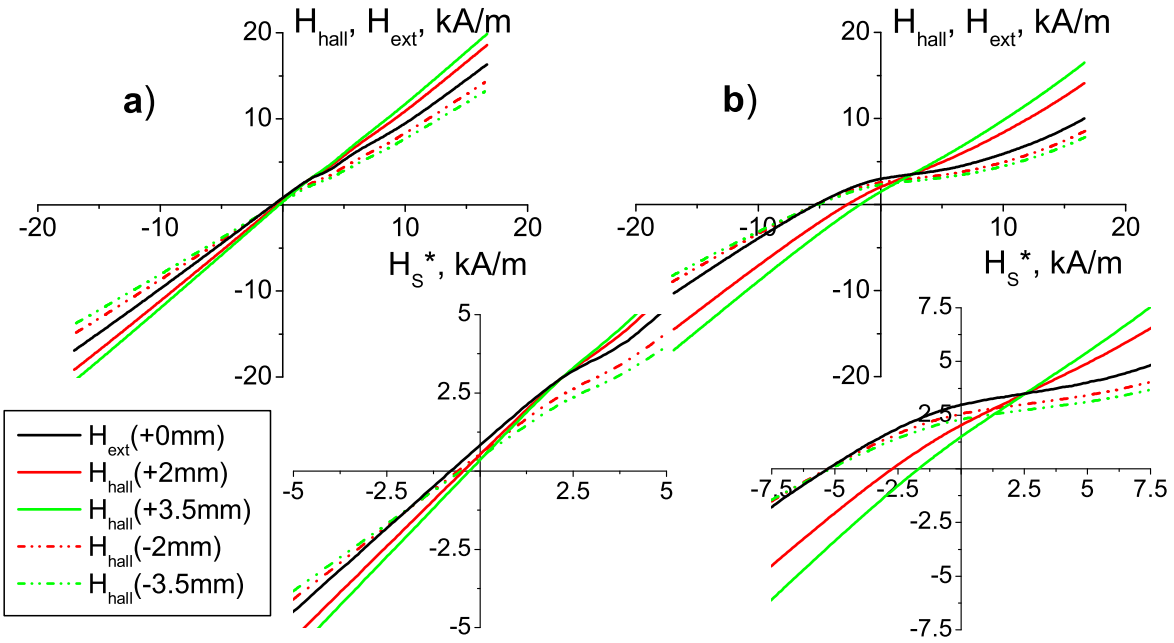

Figure 3.11: Dependencies of H_{hall} and H_{ext} on H_s^* for the perfect contact (a) and the 0.2 mm air-gap (b) between the Head 2 and the Quenched sample.

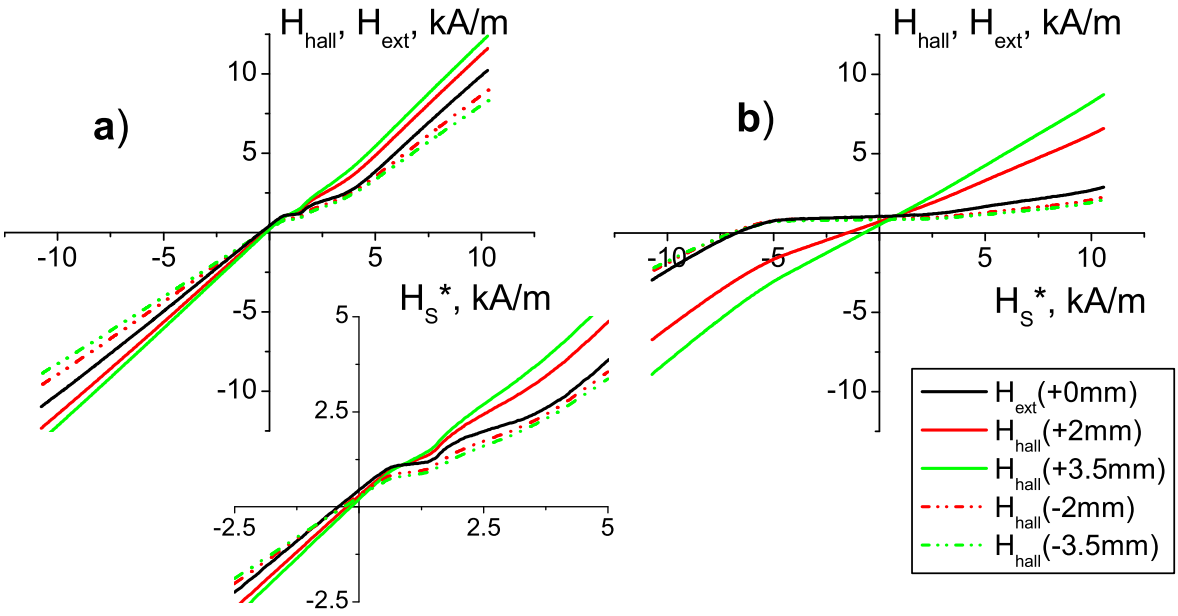

Figure 3.12: Dependencies of H_{hall} and H_{ext} on H_s^* for the perfect contact (a) and the 0.2 mm air-gap (b) between the Head 2 and the Tempered sample.

the measured and the extrapolated field derivatives as functions of the above-extrapolated fields, which are believed to correspond better to the "real" sample fields. In Figs. 3.13(a)-3.14(a) it can be seen that in reality even the effective field is not constant. Due to the self-induction signal in the driving coil it is deviated from the given constant rate in the maximum permeability/coercivity region. The softer the tested material is, the more significant this deviation is (for the investigated samples this effect is more visible in the case of the magnetically softer Tempered sample). Worsening of the contact quality reduces the self-induction and, therefore, reduces this effect of the effective field deviation too. In Figs. 3.15-3.16 the slope modules of the used linear extrapolation together with the extrapolation error (Pearson's correlation coefficient) are shown. The closer the Pearson's coefficient to one is, the better correspondence of the used linear interpolation with the experimental data is [88].

From Figs. 3.11-3.16 it can be seen that the measured as well as the extrapolated fields are substantially deviated from the triangular wave-form effective field. The main deviation is in the maximum permeability/coercivity region ($H_c = 3.4$ kA/m for the Quenched sample, and 1.1 kA/m for the Tempered sample). Moreover, the second distinguishable minimum of the field derivatives is observed. The measurable surface fields above and under the samples do not correspond to each other (see Figs. 3.13-3.14(b-c)), whereas the extrapolated fields from above and under the samples show good correlation (see Figs. 3.13-3.14(d)). Figs. 3.15-3.16 proves propriety of the used linear extrapolation except for the narrow region (1-3 experimental points) of the slopes sign change. These points (of intersection of the measured and the extrapolated fields in Figs. 3.11-3.12) do not change noticeably with different contact conditions and are positioned at small negative fields for the under-sample field extrapolation. For the above-sample extrapolation the points are very close to the coercive field values (3, 3.4 and 3.5 kA/m for the Quenched sample, and 1.1, 1.2 and 1.1 kA/m for the Tempered sample for the different contact conditions). From these intersection points

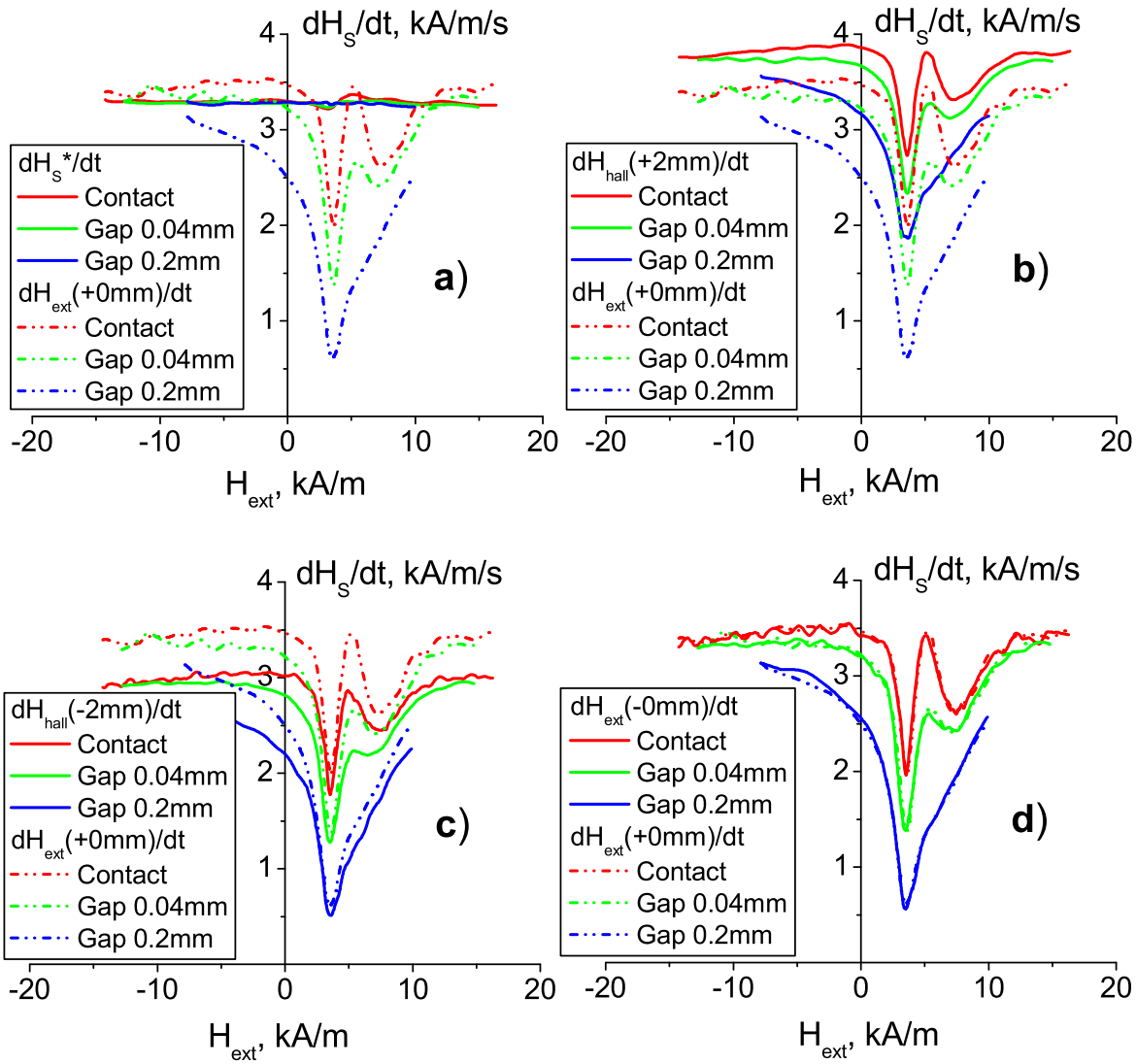

Figure 3.13: Comparison of $\mathrm{d}H_{ext}(+0\ \mathrm{mm})/\mathrm{d}t$ with $\mathrm{d}H_s^*/\mathrm{d}t$ (a), with $\mathrm{d}H_{hall}/\mathrm{d}t$ at 2 mm above (b) and under (c) the Quenched sample, as well as with $\mathrm{d}H_{ext}(-0\ \mathrm{mm})/\mathrm{d}t$ (d) as functions of $H_{ext}(+0\ \mathrm{mm})$.

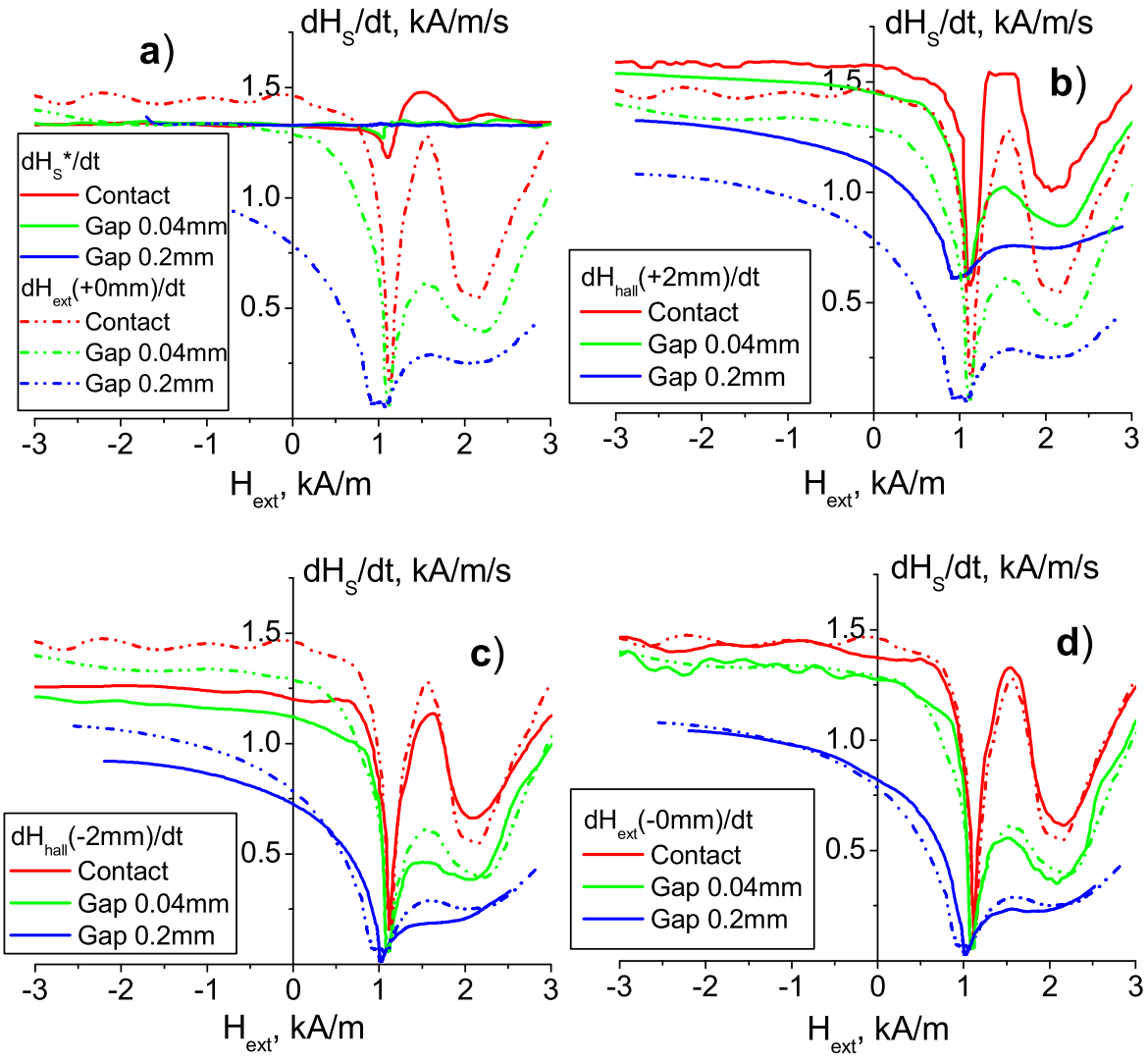

Figure 3.14: Comparison of $\mathrm{d}H_{ext}(+0\ \mathrm{mm})/\mathrm{d}t$ with $\mathrm{d}H_s^*/\mathrm{d}t$ (a), with $\mathrm{d}H_{hall}/\mathrm{d}t$ at 2 mm above (b) and under (c) the Tempered sample, as well as with $\mathrm{d}H_{ext}(-0\ \mathrm{mm})/\mathrm{d}t$ (d) as functions of $H_{ext}(+0\ \mathrm{mm})$.

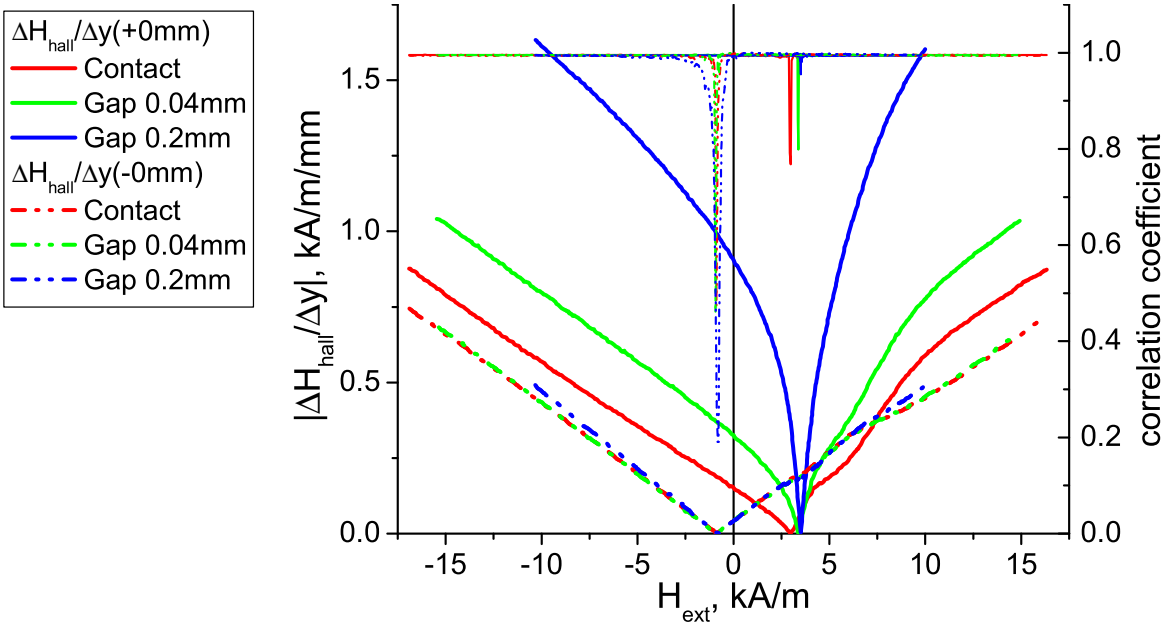

Figure 3.15: Module of the field gradient dependencies above and under the Quenched sample (left scale) and Pearson's correlation coefficient (right scale, thin upper lines) of the used linear extrapolation for the different contact conditions.

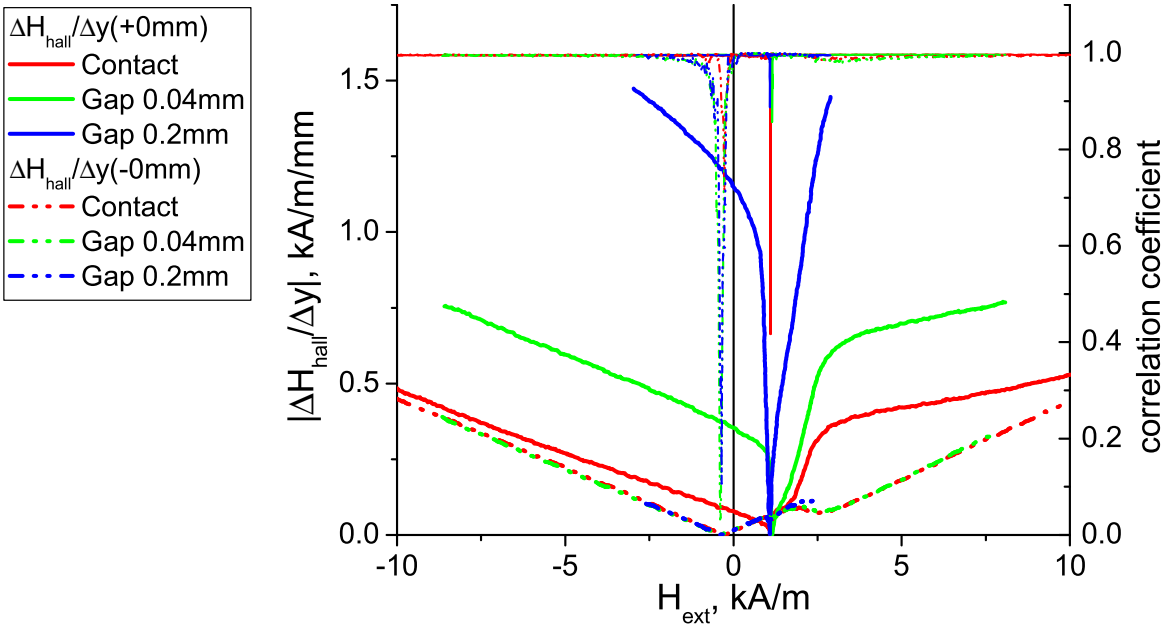

Figure 3.16: Module of the field gradient dependencies above and under the Tempered sample (left scale) and Pearson's correlation coefficient (right scale, thin upper lines) of the used linear extrapolation for the different contact conditions.

the field gradients increase with the field and reach considerable values, especially with worsening of the contact condition for the above-sample profile. In addition, the extrapolated fields change the sign before the effective field does, and worsening of the head-sample contact increases this difference (see Figs. 3.11-3.12). The field dependencies for the two tested samples are qualitatively similar.

The resulting magnetic permeability/hysteresis curves, obtained by different methods of the sample field determination, are presented in Figs. 3.17-3.21. In Figs. 3.17-3.18 the permeability curves of the Quenched and the Tempered samples, obtained by the proposed extrapolation method with different contact conditions, are shown in different scales. For comparison the corresponding permeability curves, obtained by the methods of the effective field H_s^* and of the measured surface field H_{hall}, are presented in Figs. 3.19-3.20. It can be seen that the permeability curves, obtained by the extrapolation method, are much more stable with respect to the imperfections of the head-sample contact than the widely used methods of the effective and the surface fields (see Section 1.1). They are also closer to the "true" permeability, measured on the closed ring-shaped specimens. However, the second minimum of the field derivatives leads to an unexpected hillock on the permeability profiles. For the Tempered sample the permeability curves (see Figs. 3.18) show qualitatively similar results but with much worse quantitative correlation. The second-peak form of the permeability curve is visible even with the effective field method (see Fig. 3.20(a)). The corresponding hysteresis half-loops for the two samples are presented in Figs. 3.21. They do prove better stability of the results, obtained by the extrapolation method, but also illustrate a visible difference between the extrapolated loops and the "true" ones.

3.2.3 Discussion

Magnetic measurements are based on determination of ferromagnetic *material response* to the *inside-sample magnetic field* acting on the ma-

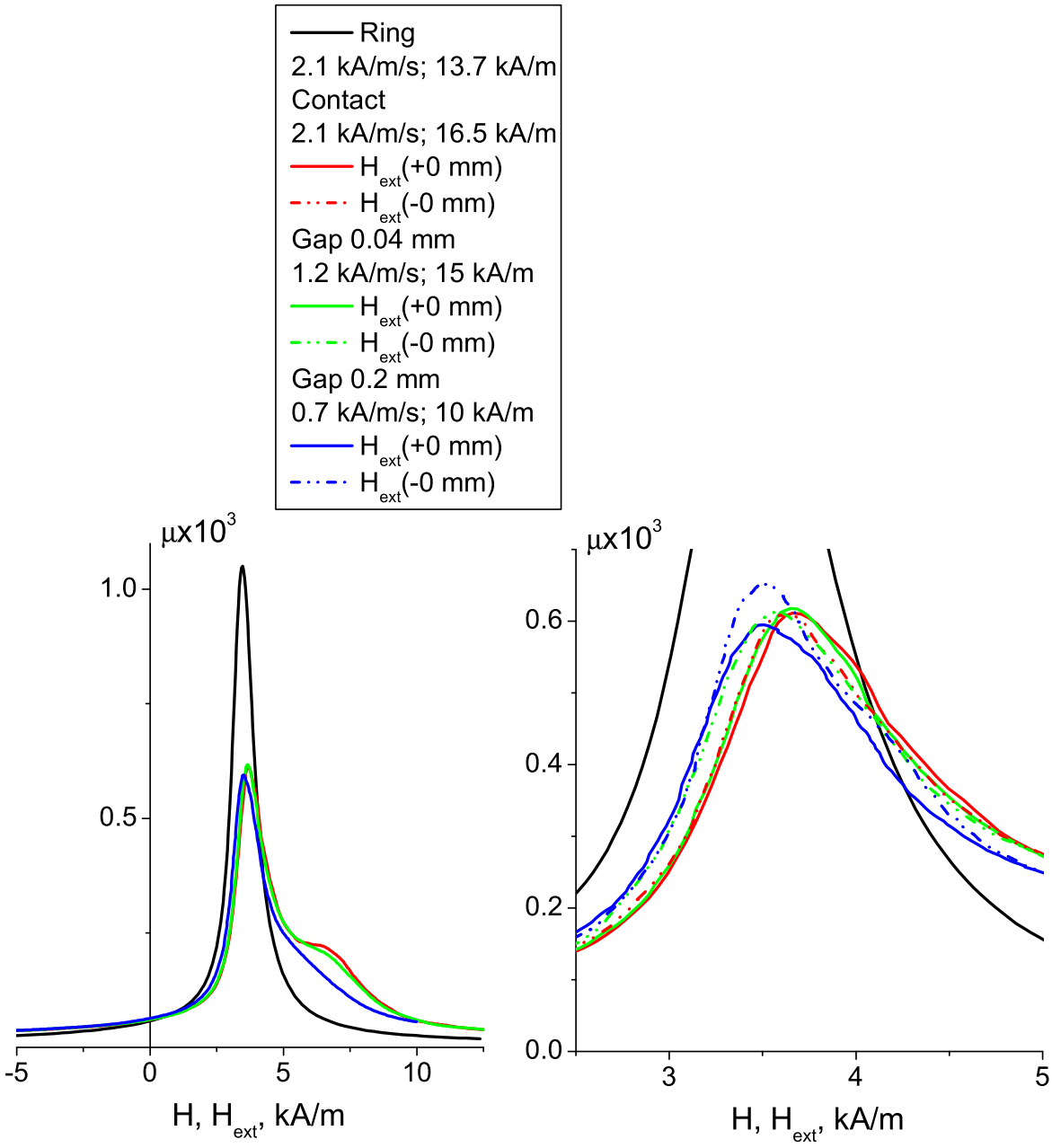

Figure 3.17: Permeability curves of the Quenched sample, obtained by the extrapolation method at different contact conditions. The measurement conditions for the each case (the minimal speed $\mathrm{d}H_{ext}/\mathrm{d}t$ and the field amplitude of H_{ext}) are pointed in text inset. The "true" permeability curve, obtained from the ring measurement, is shown for comparison.

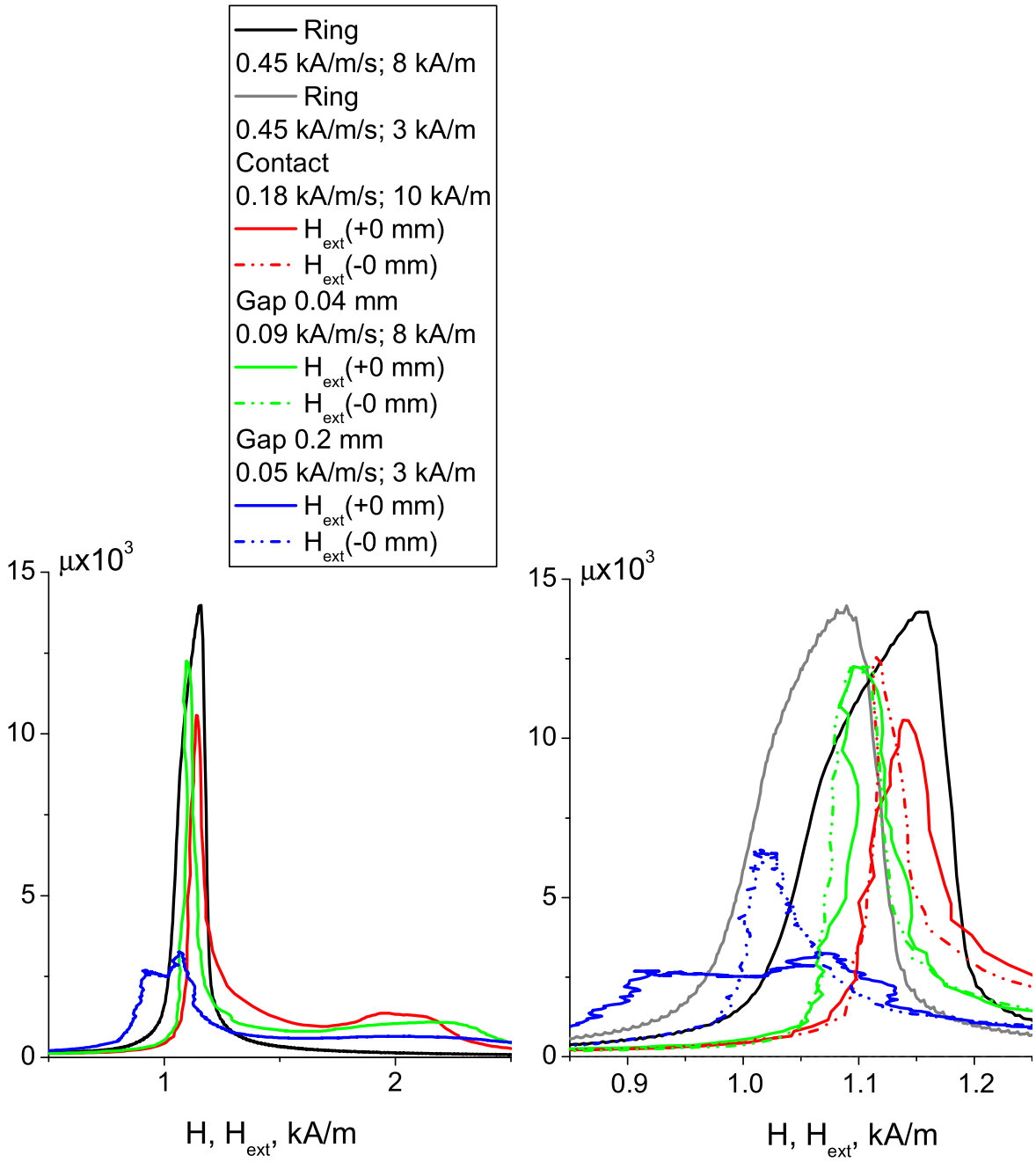

Figure 3.18: Permeability curves of the Tempered sample, obtained by the extrapolation method at different contact conditions. The measurement conditions for the each case (the minimal speed $\mathrm{d}H_{ext}/\mathrm{d}t$ and the field amplitude of H_{ext}) are pointed in text inset. The "true" permeability curves, obtained from the ring measurement, are shown for comparison.

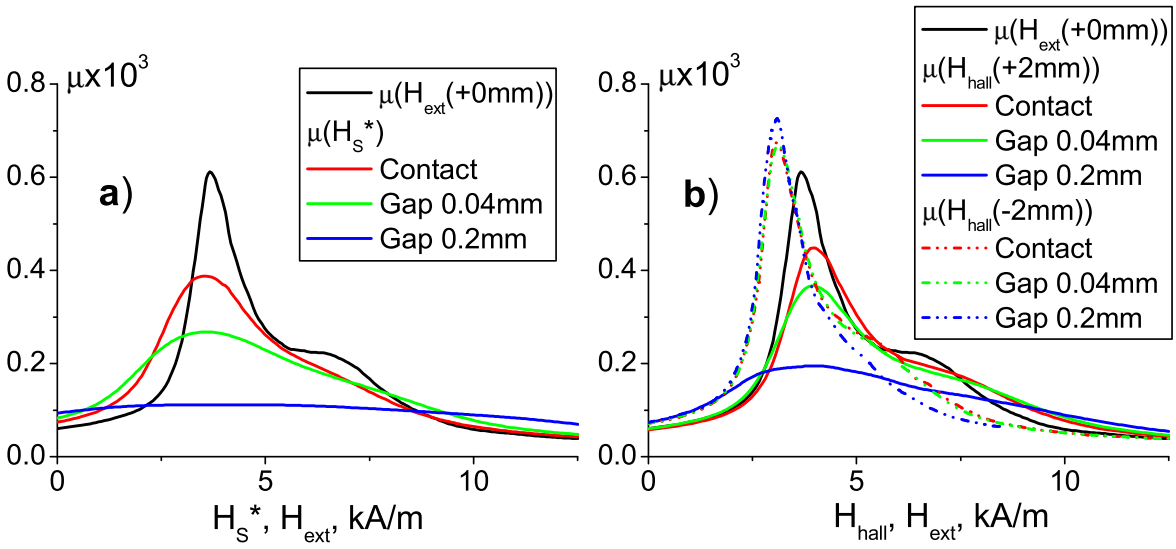

Figure 3.19: Permeability curves of the Quenched sample, obtained by use of H_s^* (a) and of H_{hall} at 2 mm distance above and under the sample (b) at different contact conditions. Permeability extrapolated curves for the perfect contact condition are shown for comparison.

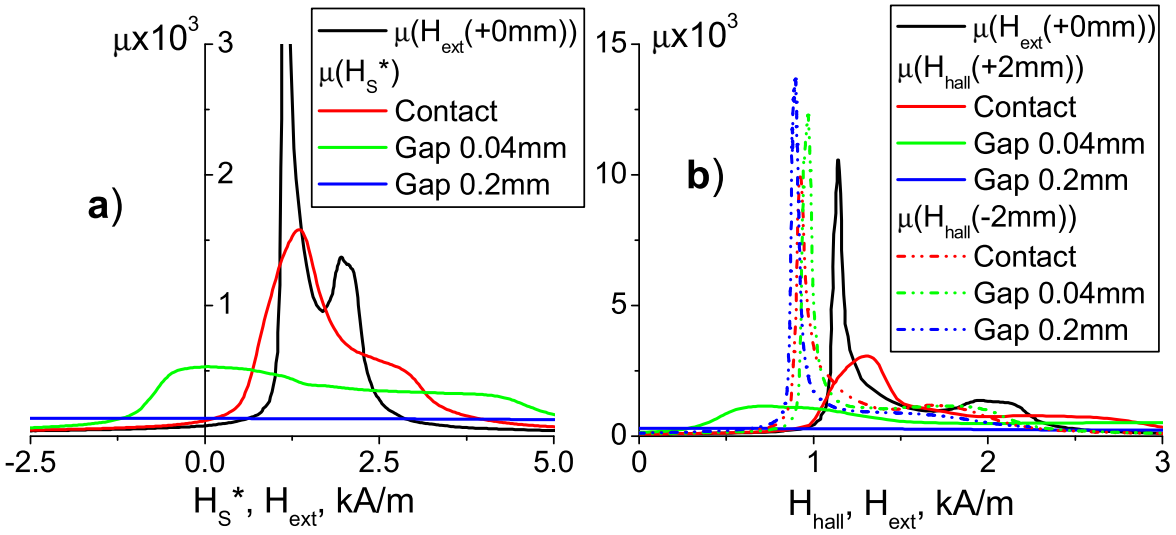

Figure 3.20: Permeability curves of the Tempered sample, obtained by use of H_s^* (a) and of H_{hall} at 2 mm distance above and under the sample (b) at different contact conditions. Permeability extrapolated curves for the perfect contact condition are shown for comparison.

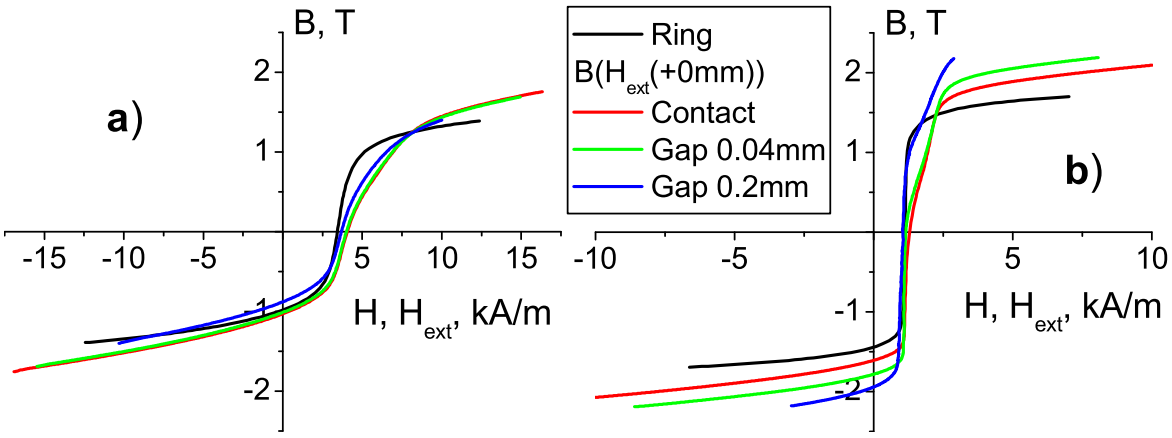

Figure 3.21: Hysteresis half-loops of the Quenched (a) and the Tempered (b) samples, obtained by the extrapolation method at different contact conditions. The "true" hysteresis half-loops, obtained from the measurement on rings, are shown for comparison.

terial. The technically easiest approach for the measurements of magnetically open samples is to apply a single ferromagnetic yoke with a magnetizing coil, which feeds the magnetic flux into the sample, and with an induction coil, which records the magnetic flux in the head-sample magnetic circuit. However, with such a setup the question of control of the sample magnetization process becomes very important. For that purpose, it would be physically accurate to measure the inside-sample magnetic field, however, this is quite a difficult task. That is the reason why the SST standard [18] prefers the method of the field determination from the magnetizing current (effective field) because of instabilities of the surface field measurements [19]. Another problem is that the induced voltage in the head induction coil does not simply record the inside-sample flux because of the non-zero flux leakage between the yoke legs (see Section 3.1.3). Therefore, the seemingly simple head-sample system is still worth of a thorough study. This work investigates applicability of the field extrapolation technique to this attractive measurement method. In comparison with the recent related works [87, 89] the single-yoke setup, used in the presented thesis, was complicated towards the case of industrial interest (smaller yoke with the induction coil on its own body and the sample overhang). Moreover,

the sample magnetization was considered in detail (extrapolation of the above- and the under-field profiles) for fundamental understanding of the underlying physical processes.

The results show substantial qualitative difference between the effective and the measured fields as well as substantial quantitative difference between the measured and the extrapolated fields (see Figs. 3.11-3.14). Moreover, there is a very good coincidence between the field extrapolation of the above- and the under-sample profiles. That proves the statement that the "true" local inside-sample field can be determined by the surface field extrapolation as it was proposed in Section 3.1.3. However, it is obvious that for the equality of the above- and the under-sample surface fields the tested sample should be thin, compared to the yoke leg cross-section, in order to achieve an entire and homogenous magnetization. The second argument for the extrapolation method is much better result stability with respect to the head-sample contact imperfections, introduced by air-gaps, and closer values of the obtained magnetic parameters to the "true" materials' values (see Figs. 3.17-3.21). But, as the arguments against, there are serious distinctions between the magnetic characteristics, obtained by the extrapolation method and by the ring measurement, which should be discussed in detail.

For the single-yokes with the driving coil/s, wound on their own body, the tested samples are magnetized by the yoke-generated flux. The measured surface as well as the extrapolated fields show two evident minimums of the fields derivatives (see Figs. 3.13-3.14), which means deceleration of the sample magnetization at the applied conditions of the constant derivative of the effective field (i.e. of the magnetizing current) $\mathrm{d}H_s^*/\mathrm{d}t \sim \mathrm{d}I/\mathrm{d}t = const.$ The first deeper minimum of the sample field derivatives corresponds to the sample maximum permeability/coercivity region, where the main part of the remagnetization process takes place. In this region the sample absorbs large amount of the yoke-generated flux at a narrow region of the magnetic field strength, which decreases the rate of the sample magnetization. Increase of the gap between the investigated sample and the yoke leads to worse conditions of the flux pen-

etration (worse sample magnetization – see Section 3.1.3) and, therefore, to smaller values of the fields derivatives (see Figs. 3.13-3.14). Another consequence of the sample-head contact imperfections is an additional flux leakage between the yoke legs, which results in overestimation of the sample flux, measured by the head induction coil/s (see Figs. 3.21).

The second shallower minimum of the field derivatives was not observed in the recent work [87], where similar experiment was done on the same sample materials but with the width of the yoke equal to that of the samples. Therefore, it can be concluded that the main reason of the obtained second minimum is the sample overhang (in this work the tested samples width is twice larger than that of the yoke – see Fig. 3.9). These second minimums of the measured/extrapolated field derivatives occur at approximately 1 T of magnetization for both samples, which would correspond to the case of near-saturated magnetization of the under-yoke region of the samples if only this region were magnetized. To all appearance, for the yoke-generated flux it is easier to penetrate into the depth of the tested samples (along x-y plane in Fig. 3.9) than into their breadth (along z-axis). To say it in another way, the magnetization of the under-yoke region of the samples surpasses the magnetization into the samples breadth. So it can be concluded that the samples magnetization proceeds via two fuzzy stages: firstly, the under-yoke part of the sample is magnetized to near-saturation, and only then the sample is completely magnetized into the breadth from the yoke too. Another possible reason of such an interesting behavior could be internal magnetization processes of the yoke itself.

The surface field distributions above and under the samples are different from each other due to the fact that the above-sample field profile is influenced by the leakage flux from the head legs and by the stray field from the driving coil. Moreover, the change of sign of the under-sample profile occurs at small negative sample fields, whereas, the change of sign of the above-sample profile occurs at the near-coercive region (see Figs. 3.11-3.12 and 3.15-3.16). In the first case, this is the point, where the under-sample field distribution is compensated by the opposite stray

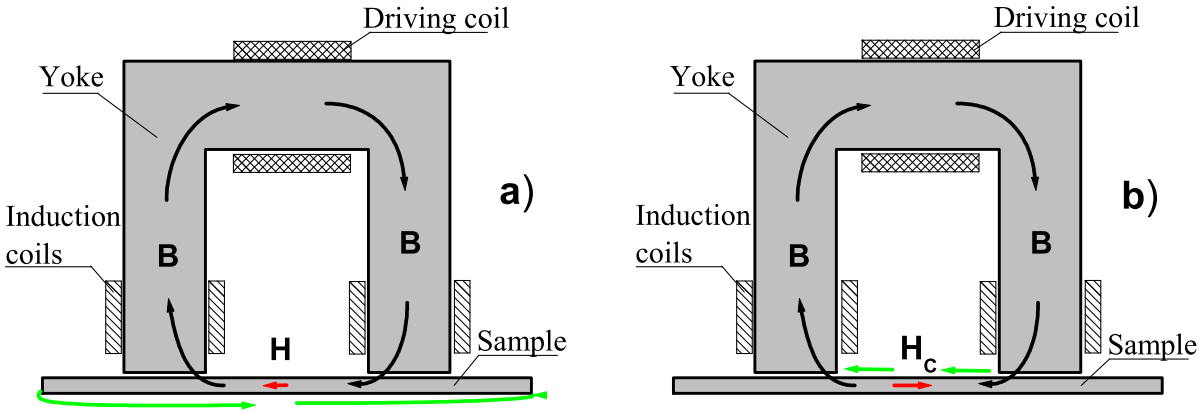

Figure 3.22: Scheme of the field-flux distributions in the single-yoke system near the points of the change of sign of the under-sample (a) and the above-sample (b) field profiles.

fields from the sample edges (see Fig. 3.22(a)). In the second case, it takes place under condition of the close-to-zero negative flux in the head-sample system, when the near-coercive surface field above the sample is compensated by the opposite leakage field from the head legs (see Fig. 3.22(b)).

Another interesting moment is the change of sign of the extrapolated fields before the corresponding sign change of the effective fields (see Figs. 3.11-3.12). This is caused by different magnetic properties of the yoke and the samples. The yoke is usually chosen to be much softer than the samples for their easy entire magnetization and the measurement result stability [38, 81]. On the other hand, such a setup configuration does often lead to the situation, when the sample has already absorbed enough amount of the yoke-generated flux to cross the remanence point, whereas, the yoke magnetization state is still before the remanence in the third hysteresis quadrant (at the negative effective fields). Of course, additionally to the differences of the yoke-sample magnetic properties, the behavior of the inside-sample field is dependent on ratio of the yoke-sample cross-sections ($\Phi_h = S_h B_h \simeq S_s B_s$). From Fig. 3.10 it can be seen that for the hysteresis loops (the case when $S_h = S_s$ and $B_h \simeq B_s$) the above-discussed condition is satisfied: remanent inductions of the

tested samples do still correspond to the inductions of the yoke in the third hysteresis quadrant.

Disparities in the magnetic field directions in the head and the sample also lead to conversion of magnetically induced attractive forces between the head and the sample to repulsive ones. The repulsive force causes the head "jumping" on the sample during the measurement in the second and the forth hysteresis quadrants. This results in distortion of the induction signal (it usually leaps a bit below the maximum permeability). The problem is generally solved by use of a pressure mechanism [32, 33] as it was also done in this work. Potential disadvantage of such a decision is the dependence of magnetic properties of the head/sample material/s on the induced mechanical stresses [25, 72].

Analysis of the around-sample field profiles proves the applicability of the used linear extrapolation in all range of magnetization except of the small regions of zero field gradients (see Figs. 3.15-3.16). These regions as well as the regions of high field gradients (at high fields or with a bad head-sample contact for the above-sample field profile) are the most problematic for the extrapolation method accuracy. Error of the extrapolation procedure, caused by mistakes of the surface field measurements (due to the sensor accuracy or small deviations of the sensor position), grows with the field gradient increase [87]. At low fields the above-sample field gradient is relatively small, which leads to comparatively reasonable results of the minor loop measurements (especially for the coercive field values) with the surface field method [37, 89]. The smaller under-sample field gradient is more appropriate for accurate extrapolation procedure. However, it can be used for the thin samples only and it complicates the device.

An attractive but technically more difficult solution can be the use of three/four Hall sensors array for the precise surface field extrapolation [81, 87]. It was confirmed by the current investigation, when the extrapolation over four points was chosen to be the best. Of course, the use of one movable sensor in this work instead of a Hall sensor array introduces an additional error due to mistakes of the sensor position de-

termination. Another serious problem of the extrapolation procedure is the noise of the Hall output signal. Therefore, the question of the best choice of the smoothing procedure is very important. Relatively small mistakes of the smoothing near the field derivative minimum could lead to substantial deviations of the maximal permeability region at the close-to-zero derivative minimum values $\mu_{dif} \sim \varepsilon_{ind}/(\mathrm{d}H_s/\mathrm{d}t)$ (large air-gapes or soft specimens as in the case of the investigated Tempered sample).

The main results of the work are presented in Figs. 3.17-3.21, where comparison of the permeability curves and the hysteresis loops, obtained by the different methods of sample field determination, for the different contact conditions together with the ring measurements is done. For the Quenched sample the comparison, presented in Figs. 3.17 and 3.21(a), is quite acceptable. There is a good correlation between the curves for the perfect contact and the smaller 0.04 mm air-gap, obtained by the above-sample field extrapolation. A little bit larger difference between the corresponding curves, obtained by the under-sample field extrapolation, is believed to be due to slightly non-homogenous magnetization into the depth of the sample (increasing with the gap) and position mistakes of the under-sample sensor installation. Deviation of the results is larger for the 0.2 mm air-gap. The reasons are the above-mentioned problems of the extrapolation accuracy and the field derivative smoothing. The small shift of the permeability maximum to lower fields is due to the field amplitude decrease below the saturation limit (checked on the ring).

However, the Tempered sample was found to be much more difficult for the measurement and for the field extrapolation procedure. A very narrow and high peak of the permeability (rectangular-like hysteresis – see Figs. 3.10 and 3.18) leads to similarly narrow and deep first peak of the field derivatives (see Figs. 3.14), which are difficult to smooth. This is the reason of larger result scatter and of worse quality of the permeability curves for the Tempered sample. Moreover, decrease of the field amplitudes of H_{ext} and the magnetization speeds $\mathrm{d}H_{ext}/\mathrm{d}t$ with the worsening of the contact conditions (see text inset in Fig. 3.18) does also result in shifting of the maximum permeability position to lower fields.

The effect of the field amplitude decrease, checked on the ring (see the zoomed Fig. 3.18), gives approximately a twice smaller shift than on the curves, obtained by the extrapolation method. Unfortunately, the ring measurement for evaluation of the dynamical effects (decrease of the magnetization speed) can not be realized on our equipment at such small magnetization speeds.

Finally, it can be declared that even for the case of the sample overhang the field extrapolation method provides the best result stability of the single-yoke measuring setup to the yoke-sample contact imperfections, compared to the effective/surface field methods. However, the deviations of the permeability/hysteresis curves, obtained by the extrapolation method, from the corresponding "true" ones, measured on the closed rings, is quite significant (see Figs. 3.17-3.20). Utilizing the same widths of the yokes and the samples gives better but also not exact correspondence of the ring and the yoke measurements [87]. In the present work the second hillock of the permeability curves, obtained by the extrapolation method due to non-homogeneous flux penetration into the sample bulk, leads to an additional detraction of the primary first permeability peak and to a corresponding deviation of the hysteresis loops to higher fields in the first quadrant (see Figs. 3.21).

The classical ring-shaped samples are uniform magnetic circuits of a single material. On the other hand, the used single-yoke measuring setup is a complex non-uniform magnetic circuit, consisted of the three magnetically different components: yoke-air-sample. These two magnetic circuits are principally different and can give the same results only in the ideal case of homogenous sample magnetization and zero magnetic reluctance of the yoke-air components of the circuit. Therefore, it is not generally correct to compare directly the results of the measurements on the classical rings and by the single-yoke setup. By the extrapolation method the measurement is stabilized by precise determination of the local surface-sample field, whereas, use of some average flux density of usually non-homogenous distribution as well as non-zero reluctances of the yoke and the air-gaps introduce measurement errors [87]. However,

due to the extrapolation method stability it can be used for the *relative* NDT measurements, based on evaluation of the *effective* magnetic parameters rather than their *absolute* analogues.

3.3 Conclusions

In the first part of this chapter (DC measurements), typical configurations of the single inspection head system with the magnetizing and the induction coils, wound on the yoke body, were designed. Magnetic field distributions in the sample and the free space around it were computed and measured as functions of the applied magnetomotive force. The set-up was tested for variations of the head-sample contact quality and the geometrical dimensions.

Recommendations for optimization of the single-yoke magnetic NDT setup were formulated. Particularly: *(i)* The single-head setup is applicable for reliable inspection of materials with *on-line determined field* $H_s(t)$ *inside the tested sample* as the reference independent variable (rather than the magnetizing current). *(ii)* The inspection head should be designed in such a way that within the expected range of the tested materials and the contact quality variations the inside-sample field $H_s(t)$ can be determined by extrapolation of $H_{on}(y,t)$ and/or $H_{un}(y,t)$. *(iii)* Minimum of *two magnetic field sensors*, integrated into the inspection head, can make the said extrapolation possible.

In the next AC measurements these recommendations were realized in practice. It was confirmed that the permeability curves and the hysteresis loops, obtained by the proposed extrapolation method, do really show a good result stability to small imperfections of the head-sample contact even for the considered case of the sample overhang. Moreover, the stability of the extrapolation method is much better than that of the widely used methods of the effective/surface fields. It gives hope that this approach can fix the well-known problem of substantial result deviations due to roughness/curvature of the tested sample surfaces for local magnetic NDT with relatively small single-yokes. However, important

drawbacks of the method were also pointed. The technical difficulties of the extrapolation procedure realization are the setup complication by a Hall sensor array and the precise smoothing of the measuring surface fields. Intrinsic imperfections of the method are considered to be the error of the magnetic flux determination and the considerable influence of the set-up configuration (sizes and shapes of the attached yoke and the tested samples) on the measurement results.

Summary

The first part of this thesis is devoted to the inductive measurements of the magnetic hysteresis and the Barkhausen noise, performed to investigate the influence of uniaxial plastic tensile deformation on magnetic behavior of the low-carbon steel in the parallel as well as in the perpendicular directions with respect to the stress. The so far scantily investigated structural-magnetic anisotropy, caused by the uniaxial tensile deformation, was considered in detail. For the first time it was shown that the profiles of differential permeability and the Barkhausen noise envelope display the usual one-peak form in the transversal direction to the previous elongation, whereas, in the axial direction they reveal an uncommon two-peak shape. This physically interesting feature was qualitatively explained by formation of the internal residual stresses and the dislocation tangles structure. On basis of this characteristic magnetic behavior of the considered problem, *new* magnetic parameters with good sensitivity-stability ratio in a wide strain range were proposed for utilization in magnetic non-destructive testing of similar low-carbon/mild steel materials.

In the second part of the thesis the technical question of applicability of the single-yoke measurement technique was investigated. The sample magnetization process with the magnetizing-and-sensing single-yoke was considered in detail on the basis of the surface field measurements and of the finite element method simulations. It was shown that the widely-used laboratory setups with the methods of the sample field determination from the magnetizing current as well as from the surface field measurements are quite unstable with respect to small frequently-occurring

deviations of the yoke-sample magnetic contact quality. Therefore, it was suggested to use the method of the surface field extrapolation for optimization of the single-yoke setup. It was firstly confirmed that the extrapolation method does really stabilize the single-yoke measurements even for the case of the sample overhang.

Bibliography

[1] D.C. Jiles, Review of Magnetic Methods for Nondestructive Evaluation, *NDT Int.* **21** (1988) 311–319.

[2] M.K. Devine, The Magnetic Detection of Material Propeties, *JOM* **44** (1992) 24–30.

[3] G.V. Bida, A.P. Nichipuruk and T.P. Tsar'kova, Magnetic Properties of Steels after Quenching and Tempering. I. General. Carbon Steels, *Russ. J. Nondestr. Test.* **37** (2001) 79–99.

[4] G.V. Bida, A.P. Nichipuruk and T.P. Tsar'kova, Magnetic Properties of Steels after Quenching and Tempering. II. Low-Alloyed Steels, *Russ. J. Nondestr. Test.* **37** (2001) 100–115.

[5] G.V. Bida, A.P. Nichipuruk and T.P. Tsar'kova, Magnetic Properties of Steels after Quenching and Tempering. III. High-Chromium Steels., *Russ. J. Nondestr. Test.* **37** (2001) 116–127.

[6] J.A. Ewing, *Magnetic Induction in Iron and Other Metals*, London: The Electrician, 1892.

[7] R.M. Bozorth, *Ferromagnetism*, Toronto: D. Van Nostrand, 1951.

[8] J.M. Makar and B.K. Tanner, The Effect of Plastic Deformation and Residual Stress on the Permeability and Magnetostriction of Steels, *J. Magn. Magn. Mater.* **222** (2000) 291–304.

[9] C.C.H. Lo, F. Tang, Y. Shi, D.C. Jiles and S.B. Biner, Monitoring Fatique Damage in Material Using Magnetic Measurement Techniques, *J. Appl. Phys.* **85** (1999) 4595–4597.

[10] C.C.H. Lo, F. Tang, S.B. Biner and D.C. Jiles, Effect of Fatique-Induced Changes in Microstructure and Stress on Domain Structure and Magnetic Properties of Fe-C Alloys, *J. Appl. Phys.* **87** (2000) 6520–6522.

[11] N. Ebine, M. Suzuki, K. Ara, H. Kikuchi, T. Abe, Y. Kamada, S. Takahashi and K. Fujiwara, Development of a Device for Measurement of Hysteresis Magnetization Curves of Charpy Impact Test Pieces, *Int. J. Appl. Electromagn. Mech.* **19** (2004) 243-248.

[12] M. Dufek, J. Hrabák and Z. Trnka, *Magnetic Measurement* (Praha: Státní Nakladatelství Technické Literatůry, 1964) (in Czech).

[13] V.G. Antonov, L.M. Petrov and A.P. Shelkin, *Measurement Techniques for Magnetic Material Parameters* (Leningrad: Energoatomizdat, 1986) (in Russian).

[14] J.D. Jackson, *Classical Electrodynamics* (New York: John Wiley & Sons Inc., 1999).

[15] International Electrotechnical Commission, *Magnetic Materials–Part 2: Method of Measurement of the Magnetic Properties of Electrical Steel Sheet and Strip by Means of an Epstein Frame* 1996 **IEC 404-2**.

[16] G.S. Korzunin, V.K. Chistyakov, F.F. Rimshev and V.M. Shevnin, Developing Techniques for Testing Magnetic Properties of Electrical Steel. III. Apparatus for Sheet Steel, *Russ. J. Nondestr. Test.* **37** (2001) 397–421.

[17] V.F. Matyuk, S.A. Goncharenko, H. Hartmann and H. Reichelt, Modern State of Nondestructive Testing of Mechanical Properties and Stampling Ability of Steel Sheets in a Manufacturing Technological Flow, *Russ. J. Nondestr. Test.* **39** (2003) 347–380.

[18] International Electrotechnical Commission, *Magnetic Materials–Part 3: Method of Measurement of the Magnetic Properties of Electrical Sheet and Strip by Means of a Single Sheet Tester* 1992 **IEC 404-3**.

[19] H. Pzützner and P. Schönhuber, On the Problem of the Field Detection for Single Sheet Tester, *IEEE Trans. Magn.* **27** (1991) 778–785.

[20] P. Beckley, C.H. Porter and D. Snell, On-line Single Sheet and Epstein Power Loss Testing, *J. Magn. Magn. Mater.* **26** (1982) 168–175.

[21] H. Ahlers and J.D. Sievert, Comparison of a Single Strip Tester and Epstein Frame Measurements, *J. Magn. Magn. Mater.* **26** (1982) 176–178.

[22] J. Sievert, The Measurement of Magnetic Properties of Electrical Sheet Steel – Survey on Methods and Situation of Standards, *J. Magn. Magn. Mater.* **215–216** (2000) 647–651.

[23] J. Sievert, Recent Advantages in the One- and Two-Dimentional Magnetic Measurement Technique for Electrical Steel Sheet, *IEEE Trans. Magn.* **26** (1990) 2553–2558.

[24] M. Wulf, D. Makaveev, Y. Houbaert and J. Melkebeek, Design and Calibration Aspect of Small Size Single Sheet Testers, *J. Magn. Magn. Mater.* **254–255** (2003) 70–72.

[25] V.E. Iordache, E. Hug and N. Buiron, Magnetic Behaviour versus Tensile Deformation Mechanisms in a Non-oriented Fe-(3wt.%)Si Steel, *Mat. Sci. Eng.* A-*Struct.* **A359** (2003) 62–74.

[26] J. Sievert, H. Ahlers, M. Birkfeld, B. Cornut, F. Fiorillo, K.A. Hempel, T. Kochmann, A. Kedous-Lebouc, T. Meydan, A. Moses and A.M. Rietto, European Intercomparison of Measurements of Rotational Power Loss in Electrical Sheet Steel, *J. Magn. Magn. Mater.* **160** (1996) 115–118.

[27] T. Nakata, Y. Ishihara, Y. Kamijyo, T. Nagai, F. Kogiku, Y. Tani and K. Yago, Intercomparison of a Single Sheet Tester for Amorphous Alloys by Round Robin Measurments in Japan, *J. Magn. Magn. Mater.* **160** (1996) 119–122.

[28] G.V. Bida and A.P. Nichipuruk, Coercive Force Measurements in Nondestructive Testing, *Russ. J. Nondestr. Test.* **36** (2000) 707–727.

[29] E.S. Gorkunov, Magnetic Devices for Testing of Structure and Mechanical Properties of Steel and Cast Iron Articles, *Defektoskopiya* **10** (1992) 3–36 (in Russian).

[30] I.A. Kuznetsov, M.N. Mikheev and T.P. Tsar'kova, Effect of the Parameters of Tested Articles on the Indications of a Coercimeter Having an Attached Electromagnet, *Sov. J. Nondestr. Test.* **9** (1973) 223–226.

[31] V.P. Tabachnik, Influence of Gaps on Coercimeter Reading with U-shaped Attached Electromagnet, *Defektoskopiya* **2** (1990) 45–52 (in Russian).

[32] C.C.H. Lo, J.A. Paulsen and D.C. Jiles, A Magnetic Imaging System for Evaluation of Material Conditions Using Magnetoresistive Devices, *IEEE Trans. Magn.* **39** (2003) 3453–3455.

[33] M.J. Sablik, L.A. Riley, G.L. Burkhardt, H. Kwun, P.Y. Cannell, K.T. Watt and R.A. Langman, Micromagnetic Model for Biaxial Stress Effects on Magnetic Properties, *J. Magn. Magn. Mater.* **132** (1994) 131–148.

[34] A. Parakka and D.C. Jiles, Magneprobe: A Portable System for Non-destructive Testing of Ferromagnetic Materials, *J. Magn. Magn. Mat.* **140-144** (1995) 1841–1842.

[35] G. Vértesy, I. Mészáros and I. Tomáš, Nondestructive Indication of Plastic Deformation of Cold-rolled Stainless Steel by Magnetic Minor Hysteresis Loops Measurement, *J. Magn. Magn. Mater.* **285** (2005) 335–342.

[36] R.A. Langman and P.J. Mutton, Estimation of Residual Stresses in Railway Wheel by means of Stress-induced Magnetic Anisotropy, *NDT&E Int.* **26** (1993) 195–205.

[37] K.J. Stevens, Stress Dependence of Ferromagnetic Hysteresis Loops for Two Grades of Steel, *NDT&E Int.* **33** (2000) 111–121.

[38] J. Brož, *Principles of Magnetic Mesurements*, Prague: Press of Czechoslovak Academy of Sciences, 1953 (in Czech).

[39] D. Jiles, *Introduction to Magnetism and Magnetic Materials*, London: Chapman & Hall, 1998.

[40] S. Takahashi, L. Zhang and T. Ueda, Magnetic Hysteresis Minor Loops in Fe Single Crystal, *J. Phys.: Condens. Matter* **15** (2003) 7997–8002.

[41] I. Tomáš, Non-destructive Magnetic Adaptive Testing of Ferromagnetic Materials, *J. Magn. Magn. Mater.* **268** (2004) 178–185.

[42] G. Bertotti, *Hysteresis in Magnetism*, San Diego: Academic Press, 1998.

[43] A. Iványi, *Hysteresis Models in Electromagnetic Computation*, Budapest: Akadémiai Kiadó, 1997.

[44] I. Tomáš, O. Stupakov, J. Kadlecová, O.Perevertov, Magnetic Adaptive Testing – Low Magnetization, High Sensitivity Assessment of Material Modifications, *J. Magn. Magn. Mater.* **304** (2006) 168–171.

[45] O. Stupakov, I. Tomáš, J. Pal'a, J. Bydžovský, J. Bošanský and T. Šmida, Traditional Barkhausen and MAT Magnetic Response to Plastic Deformation of Low-carbon Steel, *Czech. J. Phys.* **54** (2004) D47–50.

[46] O. Stupakov, B. Skrbek and I. Tomáš, Magnetic Adaptive Testing of Thermally Treated Construction Steel, *Electromagnetic Nondestructive Evaluation* (VIII) ed. T. Sollier et al. (Amsterdam: IOS Press, 2004) pp 175–182.

[47] D.G. Hwang and H.C. Kim, The Influence of Plastic Deformation on Barkhausen Effects and Magnetic Properties in Mild Steel, *J. Phys. D: Appl. Phys.* **21** (1988) 1807–1813.

[48] C. Gatelier-Rothea, J. Chicois, R. Fougeres and P. Fleischmann, Characterization of Pure Iron and (130 ppm) Carbon-Iron Binary Alloy by Barkhausen Noise Measurements: Study of the Influence of Stress and Microstructure, *Acta Mater.* **46** (1998) 4873–4882.

[49] S.M. Thompson and B.K. Tanner, The Magnetic Properties of Specially Prepared Pearlitic Steels of Varying Carbon Content as a Function of Plastic Deformation, *J. Magn. Magn. Mater.* **132** (1994) 71–88.

[50] S. Abuku, Magnetic Studies of Residual Stress in Iron and Steel Induced by Uniaxial Deformation, *Jpn. J. Appl. Phys.* **16** (1977) 1161–1170.

[51] D.P. Bulte and R.A. Langman, Origin of the Magnetomechanical Effect, *J. Magn. Magn. Mater.* **251** (2002) 229–243.

[52] A. Dhar, L. Clapham and D.L. Atherton, Influence of Uniaxial Plastic Deformation on Magnetic Barkhausen Noise in Steel, *NDT&E Int.* **34** (2001) 507–514.

[53] A.J. Birkett, W.D. Corner, B.K. Tanner and S.M. Thompson, Influence of Plastic Deformation on Barkhausen Power Spectra in Steels, *J. Phys. D: Appl. Phys.* **22** (1989) 1240–1242.

[54] O. Stupakov, J. Pal'a, I. Tomáš, J. Bydžovský and V. Novák, Investigation of Magnetic Response to Plastic Deformation of Low-Carbon Steel, to appear in *Mater. Sci. Eng.* A-*Struct.*

[55] J. Pal'a, O. Stupakov, I. Tomáš, J. Bydžovský and V. Novák, Magnetic Behaviour of Low-carbon Steel in Parallel and Perpendicular Directions to Tensile Deformation, submitted to *J. Magn. Magn. Mater.*

[56] O. Stupakov, I. Tomáš, Hysteresis Minor Loop Analysis of Plastically Deformed Low-carbon Steel, *NDT&E Int.* doi:10.1016/j.ndteint.2006.04.001.

[57] G. Vértesy, T. Uchimoto, T. Takagi, I. Tomáš, O. Stupakov, I. Meszaros, J.Pavo, Minor Hysteresis Loops Measurements for Characterization of Cast Iron, *Physica* B **372** (2006) 156–159.

[58] O.V. Perevertov, Application of the Preisach Model to the Magnetization Process in Steels, *J. Phys. D: Appl. Phys.* **35** (2002) 2467-2471.

[59] V. Moorthy, B.A. Shaw and S. Day, Evaluation of Applied and Residual Stresses in Case-carburised En36 Steel Subjected to Bending Using the Magnetic Barkhausen Emission Technique, *Acta Mater.* **52** (2004) 1927–1936.

[60] X. Kleber and A. Vincent, On the Role of Residual Internal Stresses and Dislocation on Barkhausen Noise in Plastically Deformed Steel, *NDT&E Int.* **37** (2004) 439–445.

[61] J. Pal'a, J. Bydžovský and P. Švec, Influence of Magnetizing Frequency and Construction of Pick-up Coil on Barkhausen Noise, *Journal of Electrical Engineering* **55** (2004) 38–40.

[62] D.C. Jiles, Dynamics of Domain Magnetization and the Barkhausen Effect, *Czech. J. Phys.* **50** (2000) 893–924.

[63] M. Blaow, J.T. Evans and B.A. Shaw, Magnetic Barkhausen Noise: the Influence of Microstructure and Deformation in Bending, *Acta Mater.* **53** (2005) 279–287.

[64] J. Bošanský, The effect of Deformation Temperature on Changes of the Mechanical Properties of α-Fe and/or of Low Carbon Steels, *Kov. Mater.-Met. Mater.* **10** (1972) 325–336.

[65] A.P. Nichipuruk, N.I. Noskova, E.S. Gorkunov and E.G. Ponomareva, Influence of Dislocation Structure, Caused by Plastic Deformation, on Magnetic and Magnetoelastic Properties of Iron and Low Carbon Steel, *Defektoskopiya* **12** (1992) 81–86 (in Russian).

[66] S. Takahashi, L. Zhang, S. Kobayashi, Y. Kamada, H. Kikuchi and K. Ara, Analysis of Minor Hysteresis Loops in Plastically Deformed Low Carbon Steel, *J. Appl. Phys.* **98** (2005) doi:10.1063/1.1999853.

[67] A. Dhar, L. Clapham and D.L. Atherton, Influence of Lüders Bands on Magnetic Barkhausen Noise and Magnetic Flux Leakage Signals, *J. Mater. Sci.* **37** (2002) 2441–2446.

[68] H. Kronmüller and M. Fähnle, *Micromagnetism and the Microstructure of Ferromagnetic Solids*, Cambridge: Cambridge University Press, 2003.

[69] M.J. Sablik, Modeling the Effect of Grain Size and Dislocation Density on Hysteretic Magnetic Properties in Steels, *J. Appl. Phys.* **89** (2001) 5610–5613.

[70] F. Vicena, On the Influence of Dislocations on the Coercive Force of Ferromagnetics, *Czech. J. Phys.* **5** (1955) 480–501.

[71] J. Šternberk, E. Kratochvílová, J. Hřebík and A. Gemperle, Coercivity and Microstructure of Low-alloy Cr-Mo Steel, *Phys. Stat. Sol.* A **79** (1983) 523–529.

[72] E. Hug, O. Hubert and M. Clavel, Influence of the Plastic Anisotropy on the Magnetic Properties of a Nonoriented 3% Silicon Iron, *J. Appl. Phys.* **79** (1996) 4571–4573.

[73] B.D. Cullity, Source of Error in X-ray Measurements of Residual Stress, *J. Appl. Phys.* **35** (1964) 1915–1917.

[74] E.C. Oliver, M.R. Daymond and P.J. Withers, Interphase and Intergranular Stress Generation in Carbon Steels, *Acta Mater.* **52** (2004) 1937–1951.

[75] S.M. Thompson and B.K. Tanner, The Magnetic Properties of Plastically Deformed Steels, *J. Magn. Magn. Mater.* **83** (1990) 221–222.

[76] S. Takahashi, J. Echigoya and Z. Motoki, Magnetization Curves of Plastically Deformed Fe Metals and Alloys, *J. Appl. Phys.* **87** (2000) 805–813.

[77] D.C. Jiles, The Effect of Compressive Plastic Deformation on the Magnetic Properties of AISI 4130 Steels with Various Microstructures, *J. Phys. D: Appl. Phys.* **21** (1988) 1196–1204.

[78] M.J. Sablik, S. Rios, F.J.G. Landgraf, T. Yonamine and M.F. de Campos, Modeling of Sharp Change in Magnetic Hysteresis Behavior of Electrical Steel at Small Plastic Deformation, *J. Appl. Phys.* **97** (2005) doi:10.1063/1.1856191.

[79] T.W. Krause, L. Clapham, A. Pattantyus and D.L. Atherton, Investigation of the Stress-dependent Magnetic Easy Axis in Steel Using Magnetic Barkhausen Noise, *J. Appl. Phys.* **79** (1996) 4242–4252.

[80] O. Stupakov, I. Tomáš and J. Kadlecová, Optimization of Single-yoke Magnetic Testing by Surface Fields Measurement, *J. Phys. D: Appl. Phys.* **39** (2006) 248–254.

[81] O. Stupakov, Investigation of Applicability of Extrapolation Method for Sample Field Determination in Single-yoke Measuring Setup, *J. Magn. Magn. Mater.* doi:10.1016/j.jmmm.2006.04.015.

[82] Meeker D 2004 *Finite Element Method Magnetics: Users Manual*, http://femm.foster-miller.net.

[83] T. Nakata, Y. Kawase and M. Nakano, Improvement of Measuring Accuracy of Magnetic Field Strength in Single Sheet Testers by Using Two H Coils, *IEEE Trans. Magn.* **5** (1987) 2596–2598.

[84] M. Delage, Cl. Ramiarinjaona, J.B. Desmoulins and J.F. Rialland, Measurement of Magnetic Characteristics of Ferromagnetic Materials along Arbitrary Directions under Mechanical Stress, *IEEE Trans. Magn.* **33** (1997) 4038–4040.

[85] S. Tumanski, A Multi-coil Sensor for Tangential Magnetic Field Investigations, *J. Magn. Magn. Mater.* **242-245** (2002) 1153–1156.

[86] S. Tumanski and T. Bakon, Measuring System for Two-dimensional Testing of Electrical Steel, *J. Magn. Magn. Mater.* **223** (2001) 315–325.

[87] O. Perevertov, Measurement of the Surface Field on Open Magnetic Samples by Extrapolation Method, *Rev. Sci. Instrum.* **76** (2005) doi:10.1063/1.2084367.

[88] E. Madelung, *Mathematical Apparatus of Physics*, Berlin: Springer-Verlag, 1957 (in German); Moscow: State Press of Physical-Mathematical Literature, 1961 (in Russian).

[89] T. Liu, S. Takahashi, H. Kikuchi, K. Ara and Y. Kamada, Stray Flux Effect on the Magnetic Hysteresis Parameters in NDE of Low Carbon Steel, *NDT&E Int.* **39** (2006) 277–281.